Department of Signal Processing and Acoustics

Sparse sensor arrays for active sensing

Array configurations and signal processing

Robin Rajamäki

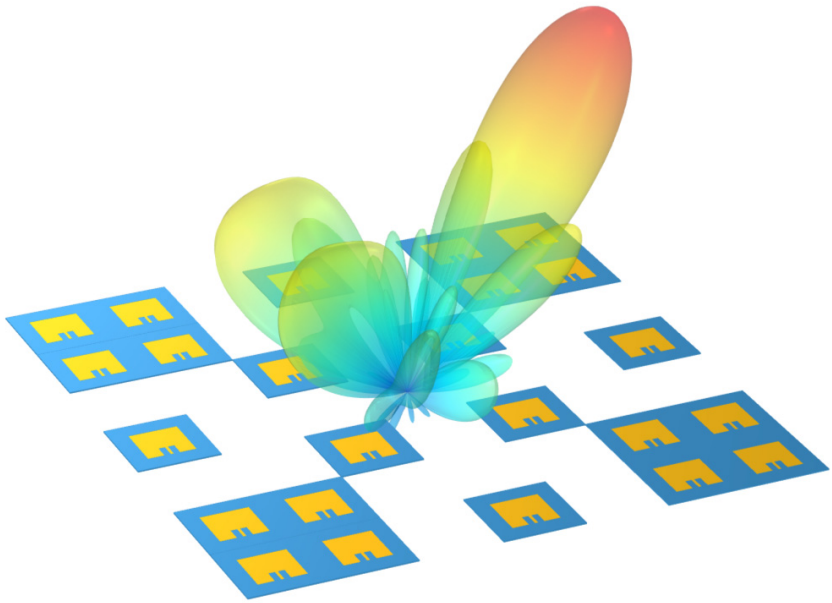

Aalto University

DOCTORAL DISSERTATIONS

Aalto University publication series
DOCTORAL DISSERTATIONS 108/2021

Sparse sensor arrays for active sensing

Array configurations and signal processing

Robin Rajamäki

A doctoral dissertation completed for the degree of Doctor of Science (Technology) to be defended, with the permission of the Aalto University School of Electrical Engineering, at a public examination held via remote connection on 10 September 2021 at 12:00.

Aalto University
School of Electrical Engineering
Department of Signal Processing and Acoustics

Supervising professor
Prof. Visa Koivunen, Aalto University, Espoo, Finland

Preliminary examiners
Prof. Fauzia Ahmad, Temple University, Philadelphia, PA, USA
Prof. Chun-Lin Liu, National Taiwan University (NTU), Taipei, Taiwan

Opponent
Prof. Geert Leus, Delft University of Technology (TU Delft), Delft, Netherlands

Aalto University publication series
DOCTORAL DISSERTATIONS 108/2021

ISBN 978-952-64-0473-8 (printed)
ISBN 978-952-64-0474-5 (pdf)
ISSN 1799-4934 (printed)
ISSN 1799-4942 (pdf)
http://urn.fi/URN:ISBN:978-952-64-0474-5

Images: Cover image: COMSOL Multiphysics® v. 5.6

Unigrafia Oy
Helsinki 2021

Finland

NORDIC SWAN ECOLABEL
Printed matter
4041-0619

Aalto University

Abstract

Aalto University, P.O. Box 11000, FI-00076 Aalto www.aalto.fi

Author
Robin Rajamäki

Name of the doctoral dissertation
Sparse sensor arrays for active sensing

Publisher School of Electrical Engineering

Unit Department of Signal Processing and Acoustics

Series Aalto University publication series DOCTORAL DISSERTATIONS 108/2021

Field of research Signal Processing

Manuscript submitted 11 May 2021 **Date of the defence** 10 September 2021

Permission for public defence granted (date) 30 June 2021 **Language** English

☐ **Monograph** ☒ **Article dissertation** ☐ **Essay dissertation**

Abstract

Multisensor systems are a key enabling technology in, e.g., radar, sonar, medical ultrasound, and wireless communications. Using multiple sensors provides spatial selectivity, improves the signal-to-noise ratio, and enables rejecting unwanted interference.

Conventional multisensor systems employ a simple array of uniformly spaced sensors with a linear or rectangular geometry. However, a uniform array spanning a large electrical aperture may become prohibitively expensive, as many sensors and costly RF-IF front ends are needed. In contrast, sparse sensor arrays require drastically fewer resources to achieve comparable performance in terms of spatial resolution and the number of identifiable scatterers or sources. This is facilitated by the co-array: a virtual array structure consisting of the pairwise differences or sums of physical sensor positions.

Most recent works on co-array-based sparse array design focus exclusively on passive sensing. Active sensing, where sensors transmit signals and observe their backscattered component, have been investigated less, despite their importance in ubiquitous applications such as radar and ultrasound imaging. The sum co-array naturally arises from the active sensing signal model, whereas the difference co-array is often more relevant in passive sensing.

This dissertation proposes novel sparse array designs and signal processing methods for active sensing and imaging. We introduce linear and planar sparse array configurations that achieve a large contiguous sum co-array for diverse aspect ratios using significantly fewer sensors than conventional arrays. These low-cost arrays resolve vastly more scatterers than sensors in both azimuth and elevation, and synthesize beampatterns that are normally achieved by uniform arrays only. Several of the proposed configurations are symmetric, which implies that their sum and difference co-arrays are equivalent, and that they are suitable for both active and passive sensing.

We also develop methods for coherent linear imaging, where image quality is improved by summing multiple component images, possibly corresponding to separate transmissions and receptions. We formulate a new optimization problem for achieving any feasible transmit-receive beampattern to a desired accuracy using as few component images as possible. We derive algorithms and closed-form expressions approximately solving this problem, and establish bounds on the number of component images of the optimal solution. We consider fully digital, hybrid, and fully analog beamforming architectures, as well as various waveform diversity cases, including phased array and orthogonal MIMO. Hybrid and analog beamforming further reduce the number of RF-IF front ends and related hardware costs, whereas waveform diversity governs the number of component images acquired per transmission. Numerical experiments verify the analytical results and characterize the trade-offs between the various system parameters. The contributions are of practical value in the design of sensor arrays for active sensing.

Keywords Sparse sensor arrays, active sensing, sum co-array

ISBN (printed) 978-952-64-0473-8 **ISBN (pdf)** 978-952-64-0474-5

ISSN (printed) 1799-4934 **ISSN (pdf)** 1799-4942

Location of publisher Helsinki **Location of printing** Helsinki **Year** 2021

Pages 252 **urn** http://urn.fi/URN:ISBN:978-952-64-0474-5

A! Aalto-yliopisto

Tiivistelmä

Aalto-yliopisto, PL 11000, 00076 Aalto www.aalto.fi

Tekijä
Robin Rajamäki

Väitöskirjan nimi
Harvat anturiryhmät aktiivisessa aistimisessa - Anturigeometrioita ja signaalinkäsittelyä

Julkaisija Sähkötekniikan korkeakoulu

Yksikkö Signaalinkäsittelyn ja akustiikan laitos

Sarja Aalto University publication series DOCTORAL DISSERTATIONS 108/2021

Tutkimusala Signaalinkäsittely

Käsikirjoituksen pvm 11.05.2021 **Väitöspäivä** 10.09.2021

Väittelyluvan myöntämispäivä 30.06.2021 **Kieli** Englanti

☐ **Monografia** ☒ **Artikkeliväitöskirja** ☐ **Esseeväitöskirja**

Tiivistelmä

Monianturijärjestelmät ovat avainasemassa monessa sovelluksessa, kuten tutkassa, kaikuluotauksessa, lääketieteellisessä ultraäänessä ja langattomassa viestinnässä. Usean anturin käyttäminen tarjoaa erinäisiä hyötyjä, kuten suunnatun lähetyksen ja vastaanoton, paremman signaali-kohinasuhteen ja mahdollisuuden torjua häiriöitä.

Perinteisissä monianturijärjestelmissä anturit on sijoitettu tasavälein janalle tai suorakulmion muotoon. Tällainen anturiryhmä voi kuitenkin tulla kalliiksi, kun sen koko ja antureiden lukumäärä kasvaa suureksi. Sitä vastoin harvat anturiryhmät, joiden anturit on sijoitettu epäjaksollisesti, vaativat huomattavasti vähemmän resursseja vertailukelpoisen suorituskyvyn saavuttamiseksi esimerkiksi sirottajien tai signaalilähteiden paikantamisessa. Tämän mahdollistaa virtuaalinen anturiryhmä, joka tyypillisesti koostuu fyysisten antureiden sijaintien parittaisista erotuksista tai summista, eli niin sanotusta erotus- tai summajoukosta.

Virtuaaliseen anturiryhmään perustuvassa harvojen anturiryhmien suunnittelussa on ennen keskitytty lähes yksinomaan passiiviseen aistimiseen. Aktiivista aistimista, jossa anturit sekä lähettävät että vastaanottavat, on tutkittu huomattavasti vähemmän. Aktiivisella aistimisella on kuitenkin tärkeitä ja laajalle levinneitä sovelluksia esimerkiksi tutka- ja ultraäänikuvantamisessa. Summajoukko ilmenee luonnollisesti aktiivisen aistimisen signaalimallissa, kun taas erotusjokko on tärkeämmässä asemassa passiivisessa aistimisessa.

Tässä väitöskirjassa ehdotetaan uusia harvoja anturigeometrioita ja signaalinkäsittelymenetelmiä aktiiviseen aistimiseen ja kuvantamiseen. Työssä kehitetään sekä lineaarisia että tasomaisia geometrioita, jotka saavuttavat suuren yhtenäisen summajoukon edullisesti käyttämällä merkittävästi vähemmän antureita kuin perinteiset geometriat. Nämä harvat anturigeometriat pystyvät sekä havaitsemaan huomattavasti antureiden lukumäärää enemmän siroittajia, että tuottamaan säteilykuvioita, jotka ovat perinteisesti vain tasavälisen geometrian saavutettavissa. Useat ehdotetuista anturigeometrioista ovat symmetrisiä, mistä seuraa, että niiden summa- ja erotusjoukot ovat samat ja että ne soveltuvat sekä aktiiviseen että passiiviseen aistimiseen.

Väitöskirjassa kehitetään myös menetelmiä lineaariseen kuvantamiseen, jossa kuvanlaatua parannetaan yhdistämällä useita komponenttikuvia, jotka mahdollisesti vastaavat erillisiä lähetyksiä ja vastaanottoja. Työssä muotoillaan myös optimointitehtävä, jonka ratkaisulla saavutetaan haluttu säteilykuvio ennalta määrättyyn tarkkuuteen käyttämällä mahdollisimman vähän komponenttikuvia. Ongelman ratkaisemiseksi johdetaan algoritmeja ja määritellään rajoja optimaaliselle komponenttikuvien määrälle tyypillisimmät monianturijärjestelmäarkkitehtuurit huomioon ottaen. Numeeriset simulaatiot vahvistavat johdetut teoreettiset tulokset ja havainnollistavat kompromisseja eri järjestelmäparametrien välillä. Kontribuutioilla on käytännön arvoa anturiryhmien suunnittelussa aktiivista aistimista varten.

Avainsanat Harvat anturiryhmät, aktiivinen aistiminen, virtuaaliryhmä, summajoukko

ISBN (painettu) 978-952-64-0473-8 **ISBN (pdf)** 978-952-64-0474-5

ISSN (painettu) 1799-4934 **ISSN (pdf)** 1799-4942

Julkaisupaikka Helsinki **Painopaikka** Helsinki **Vuosi** 2021

Sivumäärä 252 **urn** http://urn.fi/URN:ISBN:978-952-64-0474-5

Författare
Robin Rajamäki

Doktorsavhandlingens titel
Glesa sensoruppställningar för aktiv avkänning - Sensorgeometrier och signalbehandling

Utgivare Högskolan för elektroteknik

Enhet Institutionen för signalbehandling och akustik

Seriens namn Aalto University publication series DOCTORAL DISSERTATIONS 108/2021

Forskningsområde Signalbehandling

Inlämningsdatum för manuskript 11.05.2021 **Datum för disputation** 10.09.2021

Beviljande av disputationstillstånd (datum) 30.06.2021 **Språk** Engelska

☐ **Monografi** ☒ **Artikelavhandling** ☐ **Essäavhandling**

Sammandrag

Flersensorsystem är väsentliga inom t.ex. radar, ekolod, medicinsk ultraljud och trådlös kommunikation. Användning av flera sensorer medför diverse fördelar, som riktad sändning och mottagning, förbättrat signal-brusförhållande och möjligheten att dämpa oönskade störningar.

Konventionella flersensorsystem består typiskt av likformigt placerade sensorer i en linjär eller rektangulär geometri. En sådan sensoruppsättning kan dock bli dyr då dess dimensioner och sensorantal ökar. Däremot kräver glesa sensoruppsättningar drastiskt färre resurser för att uppnå jämförbar prestation, exempelvis gällande rumslig upplösningsförmåga, eller antalet identifierbara spridare eller signalkällor. Detta möjliggörs av en virtuell sensoruppsättning som består av de parvisa skillnaderna eller summorna av de fysiska sensorpositionerna, d.v.s. skillnad- eller summamängden.

Den senaste forskningen i glesa sensorgeometrier och den virtuella sensoruppsättningen fokuserar exklusivt på passiv avkänning. Aktiv avkänning, där sensorer både sänder och observerar signaler, har undersökts mindre trots dess betydelse i vidspridda applikationer som radar och ultraljudsavbildning. Summamängden uppstår naturligt i signalmodellen för aktiv avkänning, medan skillnadsmängden är mer relevant i passiv avkänning.

Denna avhandling föreslår nya glesa sensorgeometrier och signalbehandlingsmetoder för aktiv avkänning och avbildning. Vi introducerar både linjära och plana geometrier som uppnår en stor sammanhängande summamängd kostnadseffektivt genom att använda betydligt färre sensorer än konventionella geometrier. Dessa glesa sensorgeometrier upplöser märkbart fler spridare än sensorer, och syntetiserar strålningsfördelningar som traditionellt uppnås endast av likformiga geometrier. Flera av de föreslagna sensorkonfigurationerna är symmetriska, vilket innebär att deras summa- och differensmängder är ekvivalenta, och att de är lämpliga för både aktiv och passiv avkänning.

Vi utvecklar också metoder för linjär avbildning, där bildkvaliteten förbättras genom att summera flera komponentbilder, som möjligen motsvarar separata sändningar och mottagningar. Vi formulerar ett nytt optimeringsproblem, vars lösning ger en önskad strålningsfördelning med en godtycklig noggrannhet med så få komponentbilder som möjligt. Vi härleder algoritmer som approximativt löser detta problem, samt ställer gränser för antalet komponentbilder som den optimala lösningen kräver i fallet av de vanligaste flersensorsystemarkitekturerna. Numeriska experiment verifierar de analytiska resultaten och karakteriserar kompromisser mellan olika systemparametrar. Bidragen är av praktiskt värde för design av sensoruppsättningar för aktiv avkänning.

Nyckelord Glesa sensoruppställningar, aktiv avkänning, virtuell uppställning, summamängd

ISBN (tryckt) 978-952-64-0473-8 **ISBN (pdf)** 978-952-64-0474-5

ISSN (tryckt) 1799-4934 **ISSN (pdf)** 1799-4942

Utgivningsort Helsingfors **Tryckort** Helsingfors **År** 2021

Sidantal 252 **urn** http://urn.fi/URN:ISBN:978-952-64-0474-5

Preface

This research was carried out under the supervision of Prof. Visa Koivunen at the Department of Signal Processing and Acoustics, School of Electrical Engineering, Aalto University, Finland. Firstly, I would like to express my deepest gratitude to Prof. Koivunen for his guidance, mentorship, encouragement and trust, as well as for providing countless opportunities for international collaboration, networking and professional development during these past years.

Secondly, I would like to sincerely thank my pre-examiners Prof. Fauzia Ahmad and Prof. Chun-Lin Liu, as well as my opponent Prof. Geert Leus, for taking the time to carefully read my thesis and provide constructive feedback.

Thirdly, I am indebted to the many outstanding scholars who I have been fortunate to learn from and work with. Thanks to Prof. Sergiy Vorbyov and Prof. Esa Ollila for their teaching and expertise. Many thanks to co-authors Dr. Jukka Kohonen and Prof. Sundeep Chepuri for fruitful research collaborations. Thanks also to collaborators Mikko Laakso, Prof. Risto Wichman and Ossi Lehtonen. Furthermore, I am exceedingly grateful to Prof. Saleem Kassam, Prof. Yonina Eldar and Prof. Piya Pal for kindly hosting me during research visits to their world-class research groups. Thanks to Prof. Kassam, Prof. Ahmad and Prof. Yimin Zhang helping me get started with this research back in 2016. Prof. Kassam and his many excellent graduate students over the years deserve a special acknowledgment for laying the foundation for much of the work that this thesis builds upon.

This dissertation would not have been possible without the generous financial support of entities that either directly or indirectly deemed this research worthy of their resources. In truth, I never had to worry about funding thanks to the tireless efforts of Prof. Koivunen. I would nevertheless like to thank the Aalto ELEC Doctoral School, the Foundation for Aalto University Science and Technology, Nokia Bell Labs (especially Dr. Veli-Matti Kolmonen), the Nokia Foundation, the Walter Alhström Foundation, the HPY Research Foundation, the Finnish Foundation for Technology Promotion, the Finnish Defense Research Agency, and the Academy of Finland.

I would also like to thank the many colleagues whom I have had the pleasure of knowing during these past years. Thanks to Dr. Shahab Basiri, Dr. Marian Bică,

Dr. Karthik Upadhya, Henri Hentilä, Emadaldin Mozafari, and Markus Yli-Niemi for the pleasant travel company on various trips to conference and courses around the world. Thanks to past and present co-workers including Dr. Tuomas Aittomäki, Dr. Adriana Chis, Dr. Mário Costa, Dr. Gyuyeol Kong, Dr. Yongzhe Li, Dr. Maarit Melvasalo, Dr. Jari Miettinen, Dr. Hassan Naseri, Dr. Eyal Nitzan, Dr. Jan Oksanen, Dr. Nora Ouzir, Dr. Keijo Pölönen, Dr. Muhammad Tabassum, Endrit Dosti, Majdoddin Esfandiari, Farshad Ghorbani, Martin Gölz, Atchutaram Kocharlakota, Petteri Pulkkinen, Elias Raninen, Vesa Saarinen and Salil Sharma. It has also been a great pleasure to meet several exceptional people abroad, including Prof. Nir Shlezinger, Dr. Tanya Chernyakova, Dr. Regev Cohen, Dr. Satish Mulleti, Dr. Oren Solomon, Or Dicker, Shahar Stein Ioushua and Shahar Tsiper in Haifa, as well as Dr. Ali Koochakzadeh, Dr. Heng Qiao, Jiawen Chen, Mehmet Can Hücümenoğlu, Pulak Sarangi and Sina Shahsavari in San Diego. Thank you for your kind hospitality.

Last but not least, I would like to thank my friends and family for providing refreshing (and likely much-needed) distractions from academic life. Many thanks to my parents for always supporting and encouraging me. Thanks to my grandparents, to whom I am indebted for the privilege of pursuing higher education wholeheartedly and carefreely.

Helsinki, August 20, 2021,

Robin Rajamäki

Contents

List of Publications

This thesis consists of an overview and of the following publications which are referred to in the text by their Roman numerals.

I Robin Rajamäki and Visa Koivunen. Sparse linear nested array for active sensing. In *proceedings of the 25th European Signal Processing Conference (EUSIPCO)*, pp. 1976–1980, Kos, Greece, 28 August–2 September 2017.

II Robin Rajamäki and Visa Koivunen. Sparse array imaging using low-rank matrix recovery. In *proceedings of the IEEE 7th International Workshop on Computational Advances in Multi-Sensor Adaptive Processing (CAMSAP)*, pp. 1–5, Curaçao, 10–13 December 2017.

III Robin Rajamäki and Visa Koivunen. Symmetric Sparse Linear Array for Active Imaging. In *proceedings of the IEEE 10th Sensor Array and Multichannel Signal Processing Workshop (SAM)*, pp. 46–50, Sheffield, UK, 8–11 July 2018.

IV Robin Rajamäki and Visa Koivunen. Sparse Active Rectangular Array With Few Closely Spaced Elements. *IEEE Signal Processing Letters*, Volume 25, issue 12, pp. 1820–1824, December 2018.

V Jukka Kohonen, Visa Koivunen, and Robin Rajamäki. Planar Additive Bases for Rectangles. *Journal of Integer Sequences*, Volume 21, Article 18.9.8, pp. 1–25, December 2018.

VI Robin Rajamäki, Sundeep Prabhakar Chepuri, and Visa Koivunen. Analog Beamforming for Active Imaging Using Sparse Arrays. In *proceedings of the 53nd Asilomar Conference on Signals, Systems, and Computers*, pp. 1202–1206. Pacific Grove, CA, USA, 3–6 November 2019.

VII Robin Rajamäki and Visa Koivunen. Sparse Low-Redundancy Linear Array with Uniform Sum Co-array. In *proceedings of the IEEE International Conference on Acoustics, Speech and Signal Processing (ICASSP)*, pp. 4592–4596, Barcelona, Spain, 4–8 May 2020.

VIII Robin Rajamäki, Sundeep Prabhakar Chepuri, and Visa Koivunen. Hybrid Beamforming for Active Sensing using Sparse Arrays. *IEEE Transactions*

on Signal Processing, Volume 68, pp. 6402–6417, October 2020.

IX Robin Rajamäki and Visa Koivunen. Sparse Symmetric Linear Arrays with Low Redundancy and a Contiguous Sum Co-Array. *IEEE Transactions on Signal Processing*, Volume 69, pp. 1697–1712, February 2021.

Author's Contribution

Publication I: "Sparse linear nested array for active sensing"

The author proposed the idea, and performed the analysis and simulations with input from the co-authors.

Publication II: "Sparse array imaging using low-rank matrix recovery"

The author proposed the idea, and performed the analysis and simulations with input from the co-authors.

Publication III: "Symmetric Sparse Linear Array for Active Imaging"

The author proposed the idea, and performed the analysis and simulations with input from the co-authors.

Publication IV: "Sparse Active Rectangular Array With Few Closely Spaced Elements"

The author proposed the idea, and performed the analysis and simulations with input from the co-authors.

Publication V: "Planar Additive Bases for Rectangles"

The author proposed searching for extremal restricted additive planar bases, and was responsible for the two-dimensional meet-in-the-middle algorithm in

Section 4 and the numerical results related to restricted bases in Section 5. The first author was responsible for the branch and bound algorithm in Section 3, the related numerical results in Section 5, and the upper/lower bounds in Section 6.

Publication VI: "Analog Beamforming for Active Imaging Using Sparse Arrays"

The author proposed applying image addition to the analog beamforming problem, and performed the analysis as well as the simulations with input from the co-authors.

Publication VII: "Sparse Low-Redundancy Linear Array with Uniform Sum Co-array"

The author proposed the idea, and performed the analysis and simulations with input from the co-authors.

Publication VIII: "Hybrid Beamforming for Active Sensing using Sparse Arrays"

The author proposed applying image addition to the hybrid beamforming problem, and performed the analysis as well as the simulations with input from the co-authors.

Publication IX: "Sparse Symmetric Linear Arrays with Low Redundancy and a Contiguous Sum Co-Array"

The author proposed the idea, and performed the analysis and simulations with input from the co-authors.

Abbreviations

5G	Fifth generation (wireless communications standard)
6G	Sixth generation (wireless communications standard)
ADC	Analog-to-digital converter
BA	Boundary array
CNA	Concatenated nested array
CPA	Co-prime array
CRA	Concentric rectangular array
CRLB	Cramér-Rao lower bound
DAC	Digital-to-analog converter
DoA	Direction-of-arrival
DoF	Degree of freedom
EVD	Eigenvalue decomposition
ESPRIT	Estimation of signal parameters via rotational invariance techniques
i.i.d.	Identically and independently distributed
IWA	Interleaved Wichmann array
KA	Kløve Array
KMA	Kløve-Mossige Array
LS	Least squares
mmWave	millimeter wave
MIMO	Multiple-input multiple-output
MRA	Minimum-redundancy array
MSE	Mean squared error
MUSIC	Multiple signal classification
NA	Nested array
PSF	Point spread function

R-SBA	Restricted short bars array
RF-IF	Radio frequency and intermediate frequency
Rx	Receiver
S-$\mathscr{G}$	Symmetric array with generator $\mathscr{G}$
SAR	Synthetic aperture radar
SBA	Short bars array
SNR	Signal-to-noise ratio
SINR	Signal-to-interference-plus-noise ratio
SoI	Signal of interest
SVD	Singular value decomposition
Tx	Transmitter
ULA	Uniform linear array
URA	Uniform rectangular array
w.l.o.g.	Without loss of generality
WA	Wichmann array

Symbols

$\boldsymbol{A}_\xi \in \mathbb{C}^{N_\xi \times K}$	Steering matrix of Tx or Rx array
$\boldsymbol{A}_\Sigma \in \mathbb{C}^{N_\Sigma \times K}$	Steering matrix of sum co-array
$\boldsymbol{a}_\xi \in \mathbb{C}^{N_\xi}$	Steering vector of Tx or Rx array
$B \in \mathbb{N}$	# of phase shift bits
$\mathbb{C}$	Set of complex numbers
$\boldsymbol{C}_\xi \in \mathbb{C}^{M_\xi \times Q}$	Digital beamforming weight matrix of Tx or Rx array
$\boldsymbol{C}_s \in \mathbb{C}^{M_\mathrm{t} \times N_s}$	Digital Tx waveform mixing matrix
$\boldsymbol{c}_\xi \in \mathbb{C}^{M_\xi}$	Digital beamforming weight vector of Tx or Rx array
$\mathscr{D}_\xi \subseteq \mathbb{Z}^2$	Set of (normalized) Tx or Rx sensor positions
$\mathscr{D}_\Sigma \subseteq \mathbb{Z}^2$	Set of (normalized) sum co-array element positions
$\boldsymbol{d}_\xi \in \mathscr{D}_\xi$	Position of Tx or Rx sensor (in units of δ_x and δ_y)
$\boldsymbol{d}_\Sigma \in \mathscr{D}_\Sigma$	Position of sum co-array element (in units of δ_x and δ_y)
$\mathrm{diag}(\cdot)$	Diagonalization (vector to diagonal matrix)
$\mathbb{E}(\cdot)$	Expected value
$\boldsymbol{e}_i \in \{0,1\}^n$	Standard unit vector of dimension n with unit entry at index i
$\exp(\cdot)$	Natural exponential function
$\boldsymbol{F}_\xi \in \mathscr{F}_\xi(B)$	Analog phase shift matrix of Tx or Rx array
$\mathscr{F}_\xi(B)$	Set of Tx or Rx phase shift matrices quantized by B bits
$\boldsymbol{f}_\xi \in \mathscr{F}_\xi(B)$	Analog phase shift vector of Tx or Rx array
$\mathbb{H}$	Set of Hermitian matrices
$H_\Sigma \in \mathbb{N}$	# of contiguous DoFs (product of h_x and h_y)
$h \in \mathbb{N}$	Dimension of largest contiguous subarray of sum co-array
$\boldsymbol{I}$	Idenitity matrix
$\mathscr{I}_p \subseteq \{1,2,\ldots,Q\}$	Index set of component images corresponding to pth pulse
j	Imaginary number $\sqrt{-1}$
$K \in \mathbb{N}$	Number of scatterers
$L \in \mathbb{N}$	Aperture (in units of δ)

$M_\xi \in \mathbb{N}$	# of Tx or Rx front ends
$\max(\cdot)$	Maximum (coordinate-wise)
$\min(\cdot)$	Minimum (coordinate-wise)
$\mathbb{N}$	Set of natural numbers $0, 1, 2, 3\ldots$
$\boldsymbol{N} \in \mathbb{C}^{N_\mathrm{r} \times T}$	Matrix of circularly symmetric complex Gaussian noise
$N_\xi \in \mathbb{N}$	# of Tx or Rx sensors (cardinality of $\mathscr{D}_\xi$)
$N_s \in \mathbb{N}$	# of linearly independent Tx waveforms
$N_\Sigma \in \mathbb{N}$	# of sum co-array elements (cardinality of $\mathscr{D}_\Sigma$)
$\boldsymbol{n} \in \mathbb{C}^m$	Vector of circularly symmetric complex Gaussian noise
$\mathscr{O}(\cdot)$	Big O notation (order of function)
$P \in \mathbb{N}_+$	# of transmission-receptions (pulses)
$\boldsymbol{p} \in \mathbb{R}^K_{++}$	Source/scatterer power vector
$Q \in \mathbb{N}_+$	# of component images or snapshots
$\mathbb{R}$	Set of real numbers
$R \in [1, \infty)$	Redundancy
$R_\infty \in [1, \infty)$	Asymptotic redundancy
$\boldsymbol{R}_\gamma \in \mathbb{H}^K_+$	Source/scatterer covariance matrix (positive semidefinite)
$\boldsymbol{R}_s \in \mathbb{H}^{N_s}_{++}$	Waveform cross-correlation matrix (positive definite)
$\boldsymbol{R}_x \in \mathbb{H}^{M_\mathrm{r} N_s}_+$	Measurement covariance matrix (positive semidefinite)
$\boldsymbol{S} \in \mathbb{C}^{N_s \times T}$	Tx waveform matrix
$S(d) \in \mathbb{N}$	d-spacing multiplicity (# of sensor pairs displaced by d)
$\boldsymbol{W}_\xi \in \mathbb{C}^{N_\xi \times Q}$	Beamforming weight matrix of Tx or Rx array
$\boldsymbol{W} \in \mathbb{C}^{N_\mathrm{r} \times N_\mathrm{t}}$	Co-array weight matrix
$\boldsymbol{w}_\Sigma \in \mathbb{C}^{N_\Sigma}$	Beamforming weight vector of sum co-array
$\boldsymbol{w}_\xi \in \mathbb{C}^{N_\xi}$	Beamforming weight vector of Tx or Rx array
$T \in \mathbb{N}$	# of temporal snapshots
$\boldsymbol{u} \in \mathbb{R}^2$	Focusing direction (projected to sensor plane)
$\boldsymbol{v} \in \mathbb{R}^2$	Scatterer direction (projected to sensor plane)
$\mathrm{vec}(\cdot)$	Vectorization (matrix to vector)
$y \in \mathbb{C}$	Beamformer output
$\boldsymbol{x} \in \mathbb{C}^{M_\mathrm{r} N_s}$	Received signal (measurement) vector
$\mathbb{Z}$	Set of integers

$\boldsymbol{\Gamma} \in \mathbb{C}^{K \times K}$	Scattering coefficient matrix (diagonal)
$\boldsymbol{\gamma} \in \mathbb{C}^{K}$	Scattering coefficient vector
$\delta \in \mathbb{R}_{++}$	Unit inter-sensor spacing (typically $\lambda/2$)
$\varepsilon \in \mathbb{R}_{+}$	ℓ_2 approximation error
$\eta \in [0,1]$	Ratio of transceivers to all transmitters and/or receivers
$\theta \in [0,\pi]$	Elevation angle
$\lambda \in \mathbb{R}_{+}$	Wavelength
ξ	Shorthand for either Tx ($\xi = \mathrm{t}$) or Rx ($\xi = \mathrm{r}$)
$\rho \in (0,1]$	Aspect ratio of sum co-array, i.e., h_y/h_x
$\sigma^2 \in \mathbb{R}_{+}$	Noise variance
$\varsigma \in \mathbb{R}_{+}$	Weighted sum of d-spacing multiplicities
$\boldsymbol{\Upsilon} \in \{0,1\}^{N_\Sigma \times N_\mathrm{t} N_\mathrm{r}}$	Sum co-array element selection matrix
$\upsilon_\Sigma \in \mathbb{N}$	Multiplicity function of sum co-array
$\Phi(B)$	Set of phase shifts uniformly quantized by B bits
$\varphi \in [-\pi/2, \pi/2]$	Azimuth angle
$\psi \in \mathbb{C}$	Point spread function

$\varnothing$	Empty set
$\mathbf{0}$	Vector of zeros
$\mathbf{1}$	Vector of ones
$\mathbb{1}(\cdot)$	Indicator function (1 if argument is true, 0 otherwise)
$\otimes$	Kronecker product
$\odot$	Khatri-Rao product (columnwise Kronecker product)
$\circ$	Hadamard product (elementwise product)
$\times$	Cartesian product (set of all element pairs of two sets)
$*$	Convolution
$\propto$	Proportional to
$(\cdot)_{+}$	Non-negative subset
$(\cdot)_{++}$	Positive subset
$(\cdot)^{*}$	Complex conjugate
$(\cdot)^{\dagger}$	Moore-Penrose pseudoinverse
$(\cdot)^{\mathrm{H}}$	Hermitian (complex conjugate) transpose
$(\cdot)^{\mathrm{T}}$	Transpose
$(\cdot)^{1/2}$	Matrix square-root
$\lvert\cdot\rvert$	Absolute value (scalar) or cardinality (set)
$\lVert\cdot\rVert_p$	ℓ_p norm of matrix or vector
$\forall$	For all

1. Introduction

Array signal processing extracts information from measurements acquired by multiple sensors in distinct locations [207, 123, 278]. Antennas, piezoelectric transducers, and microphones are typical examples of sensors. Key benefits of multisensor systems include spatial selectivity, the capability to resolve multiple targets or signal sources occupying the same spectrum, improved signal quality, noise and interference suppression, as well as increased data rate and reliability of communication links. The physical phenomenon underlying many of these properties is wave interference, i.e., the enhancement (when signals add constructively) or cancellation (when signals add destructively) of superimposed waves resulting from appropriately delaying, or phase shifting, the sensor outputs/inputs. Sensor arrays leveraging wave interference are therefore also commonly known as *phased arrays*.

Arrays are regularly used in, for instance, communications, radar, sonar, medical ultrasound, and radio astronomy [278, pp. 6–11], where they have played an increasingly important role since the early 1900s. In particular, pioneering work at Bell Labs in the 1930s paved the way for the use of arrays in communications [84] and radio astronomy [119]. Later, the Second World War accelerated the development of radar, sonar, and medical ultrasound—culminating in the emergence of precursors to modern electronically steered phased arrays in the 1950s [248, pp. 278–279], [298], [261, pp. 3–4 and 14]. Sensor arrays have ever since been a fundamental technology of modern society, enabling applications ranging from 5G and beyond wireless communications and autonomous vehicles, to hearing aids and ultrasonography for fetal monitoring.

The properties of sensor arrays, such as spatial resolution, typically improve with increasing array *aperture*. Especially important is the physical dimensions of the array with respect to the wavelength of radiation in the surrounding propagation medium. For example, the direct observation of the black hole M87 by the Event Horizon Telescope in 2019 required an effectively earth-sized aperture spanned by multiple observatories functioning in unison around the globe [15, 16]. While area for placing telescopes is often readily available, platforms such as aircrafts, cellular basestations, and mobile devices impose more stringent constraints on the physical size of the array. For instance, in wireless

communications, spectrum congestion and the increasing need for higher data rates has led to the utilization of millimeter wave (mmWave) frequencies and the exploration of unused spectrum in the multi-hundred GHz to THz regimes [227]. The higher frequencies offer unprecedented bandwidths, which are necessary for connecting devices on a massive scale, streaming high-resolution multimedia content, or mapping the environment accurately, as envisioned in the Internet of Things [23] and joint communications/sensing systems for 6G [296]. Increasingly shorter wavelengths enable packing hundreds to thousands of sensors in a small physical area. This improves spatial selectivity and array gain, which offset the increased attenuation and signal blocking at higher frequencies. However, a high sensor count also entails increased hardware and computational costs.

The demand for cost-efficiency, low power consumption, and miniaturization has simultaneously been driven by the diffusion of radar technologies to consumer applications. Notable examples include automotive radar [204] and radars for mobile devices or wearable electronics such as Google Soli [159], which uses gesture detection based on radar measurements. In ultrasonography, a data processing bottleneck has to be overcome in order to achieve practical high-resolution volumetric imaging and portable scanners—a problem exacerbated by the real-time requirements of medical ultrasound systems, and the large sensor count of the necessary arrays [71].

Sparse sensor arrays provide a promising solution to many of the aforementioned issues. In contrast to conventional array geometries with uniformly spaced elements, the number of sensors in a sparse array only weakly depends on the array aperture. Specifically, compared to a uniform array with N sensors, a sparse array of equivalent aperture may require only $\mathcal{O}\left(\sqrt{N}\right)$ sensors. Hence, sparse arrays can attain the advantages of an electrically large aperture, such as improved resolution and the capability to identify many targets, at a low cost. This implies significant monetary and computational savings, reduced power consumption, as well as potential robustness to non-idealities, such as mutual coupling.

1.1 Scope

This thesis focuses on sparse array signal *processing* and array configuration *design*. Array processing is rooted in multichannel statistical signal processing, whose typical tasks include detection, estimation, and time-series analysis [238, 127]. This work is concerned with spatial domain signal processing using sparse arrays. In particular, we consider *active sensing* tasks such as *beamforming* and *imaging*, where a spatial distribution of scatterers is illuminated by a sparse transmitting array, and the backscattered radiation is measured by a sparse receiving array. The spatial distribution and reflectivity of the scatterers is inferred from an image, which is formed by linearly combining these measurements. Any degradation in the image quality caused by the non-uniform (sparse)

spatial sampling or other hardware constraints is compensated for by summing together several component images corresponding to different transmit and receive sensor weightings. The adopted linear processing has the advantage of requiring minimal signal model assumptions and being computationally inexpensive. A virtual array model called the *sum co-array* ensures that judiciously designed sparse array configurations are, in a sense, equivalent to uniform arrays in such active sensing tasks.

Array geometry design, i.e., appropriately placing the transmitting and receiving sensors, is a necessary prerequisite for effective array processing. In this thesis, we consider environment-independent, or nonadaptive, array design based on the concept of the co-array. As our focus is on active sensing, we limit our study to the sum co-array, which is a virtual array arising from additive structure in the signal model. The co-array quantifies the inherent *redundancy* of the array measurements. This facilitates the design of non-uniform sensor configurations with low redundancy. We specifically study the *restricted* Minimum-Redundancy Array (MRA) and related sparse array configurations that have a contiguous sum co-array. Such arrays achieve the maximum number of co-array elements for a given physical aperture, while employing as few physical sensors as possible. The uniform structure of the co-array shares many of the advantages of a uniform physical array, such as amenability to theoretical analysis, convenient matrix structures in the signal model, and simplified algorithm design. The large number of virtual co-array elements of a sparse array allows resolving significantly more scatterers or emitters compared to a uniform array with the same number of physical sensors. In particular, a sparse array with N physical sensors can identify up to $\mathcal{O}\left(N^2\right)$ sources, whereas for a uniform array the limit is $N-1$, due to the smaller array aperture. Alternatively, for the same aperture, sparse arrays require only $\mathcal{O}\left(\sqrt{N}\right)$ physical sensors to distinguish an equal number of sources, which reduces hardware and computational costs at the expense of array gain. Savings can also be achieved by employing low-complexity beamforming architectures, where part of the *digital* processing load is outsourced to an *analog* pre-processing network consisting of inexpensive phase shifters. This is of particular interest in mmWave sensing and communications, where front end electronics are expensive and consume a lot of power. We investigate using such *hybrid* architectures in conjunction with sparse arrays in active sensing tasks.

The scope of this thesis is in active sensing. Hence, array configurations for purely passive sensing and related signal processing algorithms are only briefly reviewed. In passive sensing, the transmitter is absent, and the receiver observes a superposition of source signals originating from a collection of emitters, which are typically assumed uncorrelated. Our recent works on sparse passive arrays [222, 224, 146] are excluded from the thesis for brevity. We note that most of the array configurations developed in this work are nevertheless suitable for passive sensing, since they have a uniform difference co-array.

We also omit our preliminary work on near field imaging using sparse arrays

[223] from the thesis and limit ourselves to a far field point scatterer model—although, for completeness, Appendix A.2 outlines some relevant extensions to this model. Despite assuming discrete scatterers, we do not restrict their number, nor do we require that the unknown model parameters are identifiable. This effectively enables modeling continuous scatterers, which are typically encountered in, e.g., ultrasonography.

Moreover, it is beyond the scope of this work to examine the statistical performance and identifiability conditions of the considered algorithms and signal model in detail, because our focus is on beamforming and imaging in active sensing rather than parameter estimation. Due to the linearity of the studied imaging method, performance is characterized by the achievable point spread function, which defines the response of a linear imaging system to a point source.

A detailed study of the *general* MRA is left for future work. The general MRA maximizes the largest contiguous subarray contained in the sum co-array for a given number of physical sensors, but may require an exceedingly large physical aperture. In contrast, the aperture of the considered restricted MRA, or any sparse array configurations with a contiguous sum co-array, is directly determined by the number of co-array elements and aspect ratio.

1.2 Research objectives and problems

This work aims to advance the understanding and state-of-the-art of active sensing using sparse arrays. Specifically, the research objectives are

- Characterizing the active sum co-array-based MRA
- Designing scalable low-redundancy sparse array configurations
- Developing linear imaging and beamforming for active sensing using sparse arrays and hybrid architectures.

We now briefly motivate the relevance of each of these objectives, and give examples of related research problems addressed in the thesis.

The sum co-array based active MRA has received surprisingly limited attention in the past. Apart from work by Hoctor and Kassam in the 1990s [113], even active array redundancy seems to be lacking a precise definition that both holds for different degrees of overlap between the transmitting and receiving arrays, and is consistent with Moffet's original definition of passive array redundancy [187]. Solutions to the MRA problem are also largely unknown, especially in the two-dimensional (planar array) case. Moreover, the MRA is not unique in general. Consequently, solutions may be ranked based on additional design criteria. For example, minimizing the number of closely spaced sensors can reduce mutual coupling, as sensors placed further apart interact more weakly with each other.

Similar to the active MRA, there is little work on low-redundancy sparse array configurations with closed-form sensor positions and a contiguous sum co-array. Developing such scalable array geometries is important, since the MRA requires solving a combinatorial optimization problem, which is impractical when the desired aperture or number of sensors is large. For instance, linear MRAs with shared transmitters and receivers are unknown for more than 48 sensors. Furthermore, generating sparse array configurations for any array aspect ratio is crucial, as certain applications, such as radar, may require different resolution in azimuth and elevation. The symmetry of the physical array configuration is also known to play a role in active array design. However, the utility of symmetry and how it can be leveraged needs clarification.

A final research topic is understanding the effect of various system parameters on the performance of linear imaging. Principle examples of such parameters are the beamforming architecture, waveform diversity, and sparsity of the array configuration. Previous works have established that any sum co-array equivalent array configurations can achieve comparable image quality by summing multiple component images corresponding to different transmit and receive beamforming weight pairs [111]. However, several transmissions or linearly independent transmit waveforms may be required to achieve a desired image quality, which inevitably leads to a trade-off between reconstruction fidelity and acquisition time or hardware complexity. A quantitative understanding of this trade-off is crucial for optimizing the imaging system.

1.3 Contributions

This thesis presents novel contributions in sparse array design and processing for active sensing. The key results have been published in Publications I–IX. Table 1.1 shows a thematic overview of the articles. The thesis also contains some unpublished supplementary results, which are listed in Table 1.2. In summary, the main contributions of this work are:

1) Novel linear and planar sparse array configurations for active sensing

    a) Defined a general expression for the redundancy of active arrays that takes into account the desired overlap between the transmit and receive arrays (included in the thesis only).

    b) Formulated the active MRA problem using the proposed definition of redundancy for both a fixed number of physical sensors and a fixed sum co-array size (Publication V, IX, and new results in the thesis).

    c) Computed new planar MRAs using a novel two-dimensional extension of a state-of-the-art global search algorithm (Publication V)

    d) Proposed novel sparse planar array configuration with closed-form sensor positions. These arrays are minimally redundant in some

Table 1.1. Overview of publications. The two major themes of the thesis are sparse array design and signal processing for active sensing. We consider both linear and planar sparse array configurations, as well as imaging using sparse arrays with fully digital, hybrid, or fully analog beamforming architectures.

	Sparse array design		Active linear imaging			
Publication	Linear	Planar	Digital	Hybrid	Analog	Section
I	✓					4.3.3
II			✓			5.3.1
III	✓					4.3.3
IV		✓				4.3.1
V		✓				4.2.4
VI					✓	5.3.3
VII	✓					4.3.3
VIII			✓	✓	✓	5.3
IX	✓					4.3.3

Table 1.2. Unpublished results included in the thesis only. These auxiliary results bridge the gaps between Publications I–IX and cohere the dissertation.

#	Description	Result	Section
i	Extension of Publications II, VI and VIII to the general MIMO signal model	Eqs. (3.5), (5.5) and (5.6)	3.2
ii	Definition of redundancy for diverse overlap between Tx and Rx arrays	Eq. (4.2)	4.1.2
iii	MRA with non-overlapping Tx and Rx sensors (or single overlapping sensor)	Proposition 4.1	4.2.2
iv	Aspect ratio independent array with a contiguous sum co-array	Eq. (4.8)	4.3.2
v	Analysis of noise and interference suppression capability of image addition	Eqs. (5.14) to (5.17)	5.2
vi	Improved upper bounds on # of component images in case of fully digital beamforming	Eq. (5.21)	5.3.1
vii	Improved upper bound on # of component images in case of hybrid beamforming	Proposition 5.1	5.3.2

cases, and achieve a low redundancy for any aspect ratio (Publication IV, V, and new results included in the thesis).

e) Presented a unifying framework for symmetric sparse linear arrays. This allows constructing configurations with a contiguous sum and difference co-array. Such arrays are suitable for both active and passive sensing (Publication I, III, VII, and IX).

2) Active linear imaging using sparse arrays and hybrid beamforming

a) Analyzed the noise and interference suppression capability of active linear imaging using multiple transmissions and receptions (included in the thesis only).

b) Formulated an optimization problem for synthesizing any point spread function supported on the co-array using a minimum number of component images (Publication II, VI, and VIII).

c) Derived lower and upper bounds on the number of transmission-receptions required by a fully digital, hybrid, or fully analog beamforming architecture to achieve a desired point spread function (Publication VIII and new results included in the thesis).

d) Proposed algorithms for numerically finding the beamforming weights in the case of the fully digital, hybrid, or fully analog beamforming architectures (Publication VI and VIII)

A list of publications and the author's contributions can be found starting on page 10. The author is the primary author of all publications except Publication V, where the author was mainly responsible for computing restricted additive bases (corresponding to restricted MRAs). Otherwise, the author proposed the main technical ideas, and performed the analyses and simulations with input from the co-authors. The co-authors have contributed by steering and planning the research, as well as writing and revising the publications.

1.4 Organization

The thesis is organized as follows. Chapter 2 briefly reviews the sparse array literature, including sparse array design and processing. For simplicity, we start with the canonical passive linear array, which is the most widely considered model in the literature. Chapter 3 introduces the active planar array model, which is the main focus of this work. Chapter 4 formulates the sum co-array based sparse array design problem, and presents novel linear and planar array configurations. Chapter 5 proposes an active imaging framework that facilitates the use of both sparse arrays and hybrid beamforming architectures. Chapter 6 concludes the thesis by summarizing the main results and open problems.

1.5 Notation and basic identities

The most frequently used symbols and notation of this thesis are listed in a symbol table starting from page 13. We generally denote matrices by boldface uppercase, e.g, $\boldsymbol{A}$, vectors by boldface lowercase, $\boldsymbol{a}$, and scalars by unbolded letters, A, a. The (n,m)th element of matrix $\boldsymbol{A}$ is denoted as A_{nm}. If the matrix is distinguished by a subscript, say $\boldsymbol{A}_i$, the (n,m)th element is denoted $[\boldsymbol{A}_i]_{nm}$.

Calligraphic letters, e.g., $\mathscr{A}$, denote nonstandard sets, i.e., sets other than $\mathbb{R}, \mathbb{C}, \mathbb{N}$ etc. The two exceptions to this rule are $\mathcal{O}(\cdot)$ and $\mathbb{E}(\cdot)$, which denote the order of a function and the expectation operator, respectively. The set of integers from a to c in steps of b is denoted by $\{a : b : c\}$, where shorthand $\{a : c\}$ is used when $b = 1$. The Cartesian product between two sets $\mathscr{A}$ and $\mathscr{B}$ is denoted by $\mathscr{A} \times \mathscr{B} \triangleq \{(a,b) \mid a \in \mathscr{A}; b \in \mathscr{B}\}$. We interpret the elements of the product set as two-dimensional vectors when $\mathscr{A}$ and $\mathscr{B}$ are scalar sets. The coordinate-wise minimum of a real-valued set is defined as a vector whose entries are the minima of the respective coordinate of any vector in the set, that is,

$$\min \mathscr{A} \triangleq \{\boldsymbol{b} \mid b_i = \min \boldsymbol{e}_i^{\mathrm{T}} \boldsymbol{a};\ \boldsymbol{a} \in \mathscr{A}\}.$$

Here $\boldsymbol{e}_i$ is the standard unit vector of appropriate dimensions consisting of zeros except for the ith entry, which is unity. Note that $\min \mathscr{A}$ is not necessarily a member of $\mathscr{A}$ in the non-scalar case. The coordinate-wise maximum is defined in a similar manner as

$$\max \mathscr{A} \triangleq \{\boldsymbol{b} \mid b_i = \max \boldsymbol{e}_i^{\mathrm{T}} \boldsymbol{a};\ \boldsymbol{a} \in \mathscr{A}\}.$$

In the case $\mathscr{A}$ is a scalar set, the coordinate-wise minimum (maximum) reduces to the conventional minimum (maximum).

For matrices $\boldsymbol{A}, \boldsymbol{B}$, and $\boldsymbol{C}$ of appropriate dimensions, the following identity relates the vectorization operation and the Kronecker product:

$$\mathrm{vec}(\boldsymbol{ABC}) = (\boldsymbol{C}^{\mathrm{T}} \otimes \boldsymbol{A})\,\mathrm{vec}(\boldsymbol{B}).$$

If $\boldsymbol{B}$ is diagonal, i.e., $\boldsymbol{B} = \mathrm{diag}(\boldsymbol{b})$, then this simplifies to the Khatri-Rao (column-wise Kronecker) identity

$$\mathrm{vec}(\boldsymbol{ABC}) = (\boldsymbol{C}^{\mathrm{T}} \odot \boldsymbol{A})\boldsymbol{b}.$$

2. Review of sparse arrays

This chapter reviews key concepts in sparse array design and processing. We consider a passive linear array model, which serves as a simple starting point to describing basic sparse array configurations and methods. The main body of literature on sparse arrays studies passive sensing. Chapter 3 focuses on the more general planar array model for active sensing. The scope and contributions of this work are in active sensing using sparse arrays.

The chapter is organized as follows. Section 2.1 introduces the canonical passive array model. Section 2.2 shortly discusses common approaches to sparse array design. Section 2.3 presents established methods for leveraging the degrees of freedom provided by sparse arrays in the classical array processing application of direction-of-arrival estimation. Section 2.4 concludes the chapter by briefly reviewing prior work on sparse arrays in active sensing and imaging.

2.1 Canonical passive linear array model

The ubiquitous passive array model is featured in most of the literature on array processing due to its simplicity and wide applicability [143, 207, 123, 278]. Passive sensing is regularly employed in, for example, wireless localization [78], radar [145], sonar [131], radio astronomy [65], seismic monitoring [234], as well as optical fluorescence microscopy [108]. As illustrated in Fig. 2.1, a passive array consists of a collection of spatially distributed receivers that observe a superposition of waves emitted by a number of *emitters* or signal *sources*. Typically, the sources are assumed uncorrelated. Partially correlated and coherent signal models are also regularly considered, since, e.g., multipath propagation can give rise to correlation between the perceived sources [143, 285].

2.1.1 Received signal and covariance

Consider an array of N sensors observing a superposition of signals from K far field narrowband point sources. The received signal of this passive array at time

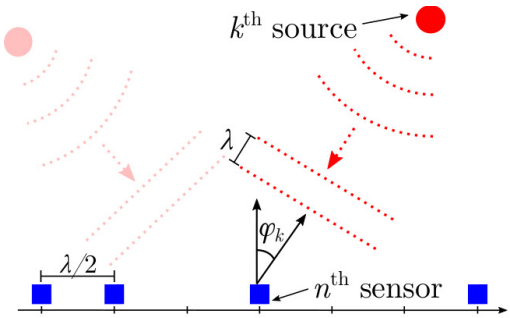

Figure 2.1. Passive linear array. Each sensor receives a superposition of narrowband source waveforms from a set of far field point emitters.

t is described by the continuous time model [143]

$$\boldsymbol{x}(t) = \boldsymbol{A}\boldsymbol{\gamma}(t) + \boldsymbol{n}(t), \tag{2.1}$$

where $\boldsymbol{A} \in \mathbb{C}^{N\times K}$ is the array steering matrix, $\boldsymbol{\gamma}(t) \in \mathbb{C}^K$ is the source signal vector, and $\boldsymbol{n}(t) \in \mathbb{C}^N$ is a receiver noise vector. The kth column of the steering matrix—or the *steering vector* $\boldsymbol{a}(\varphi_k) \in \mathbb{C}^N$—characterizes the response of the array to a the kth source at angle $\varphi_k \in [-\pi/2, \pi/2]$. The source signals are commonly assumed to be uncorrelated and follow a complex circularly symmetric normal distribution. Similarly, the noise is assumed Gaussian, uncorrelated with the signals, and spatio-temporally white. The received signal covariance matrix therefore becomes

$$\boldsymbol{R}_x \triangleq \mathbb{E}(\boldsymbol{x}\boldsymbol{x}^{\mathrm{H}}) = \boldsymbol{A}\boldsymbol{R}_\gamma\boldsymbol{A}^{\mathrm{H}} + \sigma^2\boldsymbol{I}, \tag{2.2}$$

where $\boldsymbol{R}_\gamma \triangleq \mathbb{E}(\boldsymbol{\gamma}\boldsymbol{\gamma}^{\mathrm{H}}) = \operatorname{diag}(\boldsymbol{p})$ is a diagonal matrix containing the source signal powers $\boldsymbol{p} \in \mathbb{R}^K_{++}$, and $\sigma^2 \in \mathbb{R}_+$ is the noise variance. In practice, (2.2) may have to be estimated from a finite sample using, e.g., the sample covariance matrix

$$\hat{\boldsymbol{R}}_x \triangleq \frac{1}{T}\sum_{i=1}^{T} \boldsymbol{x}(t_i)\boldsymbol{x}^{\mathrm{H}}(t_i). \tag{2.3}$$

Here t_i corresponds to the ith discrete time sample, and $T \in \mathbb{N}_+$ denotes the number of *snapshots*, where $T \geq N$ is necessary for $\hat{\boldsymbol{R}}_x$ to have full rank.

Note that since $\boldsymbol{R}_\gamma$ is diagonal, the vectorized covariance becomes

$$\boldsymbol{r}_x \triangleq \operatorname{vec}(\boldsymbol{R}_x) = (\boldsymbol{A}^* \odot \boldsymbol{A})\boldsymbol{p} + \sigma^2 \operatorname{vec}(\boldsymbol{I}). \tag{2.4}$$

Eq. (2.4) resembles the received signal model in (2.1). However, there are three important differences. Firstly, the K-dimensional signal vector $\boldsymbol{p}$ now consists of the (positive) source powers, rather than the complex-valued source waveform vector $\boldsymbol{\gamma}$. Secondly, the perturbation vector $\sigma^2\operatorname{vec}(\boldsymbol{I})$ is deterministic—assuming the noise variance σ^2 is constant—contrary to the stochastic noise vector $\boldsymbol{n}$ in (2.1). Thirdly, and most importantly, the effective steering matrix $\boldsymbol{A}^* \odot \boldsymbol{A}$ in (2.4)

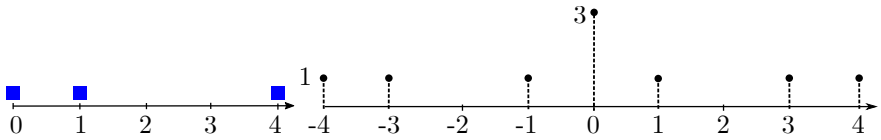

(a) Physical array **(b)** Difference co-array

Figure 2.2. Example of physical array and difference co-array.

can have substantially more unique rows than the physical steering matrix $\boldsymbol{A}$ in (2.1). This implies that significantly more sources than sensors can be identified, if the source directions or powers are of primary interest, rather than recovering the source signals themselves.

2.1.2 Difference co-array

To gain insight into (2.4), assume that the array consists of ideal omnidirectional sensors that are perfectly isolated from each other. Additionally, assume that the sensors are located on the real line at integer multiples of half a wavelength to avoid spatial aliasing. The entries of the steering matrix may then be written as $A_{n,k} = \exp(j\pi d_n \sin\varphi_k)$, which implies that the entries of the effective steering matrix in (2.4) are

$$\left[\boldsymbol{A}^* \odot \boldsymbol{A}\right]_{(m-1)N+n,k} = \exp\left(j\pi(d_n - d_m)\sin\varphi_k\right).$$

Here $d_n \in \mathbb{Z}$ is the normalized position of the nth sensor in units of half a wavelength. The sensor locations may thus be conveniently expressed as integers, bearing in mind that the true positions are integer multiples of the underlying inter-sensor displacement, which is typically half a wavelength as assumed here.

In any case, the number of unique equations in (2.4) is determined by the number of unique pairwise sensor position differences. The virtual array consisting of these differences, i.e., the *difference co-array*, is defined as

$$\mathscr{D}_\Delta \triangleq \mathscr{D} - \mathscr{D} = \{d_n - d_m \mid d_n, d_m \in \mathscr{D}\},$$

where $\mathscr{D} = \{d_n\}_{n=1}^N \subseteq \mathbb{Z}$ is the set of normalized sensor positions. A simple counting argument shows that the number of elements in the difference co-array satisfies $|\mathscr{D}_\Delta| \leq N(N-1)+1$, which implies that a sparse array may identify up to $\mathscr{O}(N^2)$ sources from (2.4). This is substantially more than the conventionally considered upper bound $N-1$ [256], which is also the number of sources identifiable by a uniform array with N sensors.

2.2 Sparse array design

Realizing the full potential of the co-array requires that the physical array configuration is sparse. That is, the array should have nonuniformly spaced

sensors in order to generate as many unique pairwise sensor position differences as possible. This is trivial to achieve if sensors can be placed arbitrarily, but less so if they are constrained to a uniform grid. In this work, we define a *sparse array* as a set of nonuniform sensor positions on a uniform lattice (cf. Fig. 2.2). This definition of a sparse array naturally suggests the concept of a uniform co-array, which can greatly simplify both array processing algorithms and the underlying theory. An especially useful property of a uniform array, be it physical or virtual, is the Vandermonde structure of the resulting array steering matrix [255, p. 161], [200]. Constraining the sensors to lie on a regular lattice is also a practical way to guarantee a sufficient spacing between sensors. Prominent examples of sparse array configurations falling into this category are the Minimum-Redundancy Array [187], Wichmann Array [294], Nested Array [200], and Co-Prime Array [276]. Section 2.2.2 discusses this approach to sparse array design in more detail. For completeness, however, we first briefly review other common definitions of sparse arrays.

2.2.1 Nonuniform arrays

The vast literature on sparse array design dates back to at least the work of Schelkunoff in the 1940s [239]. Early works on *nonuniform* or *aperiodic* arrays mainly considered *spatial density tapering*, where a desired beampattern is synthesized by continuously varying the positions of the sensors. In contrast, the discrete *sensor selection* problem has been more actively studied in recent times.

Spatial tapering
In spatial tapering, the desired beamforming weight function or taper, is interpreted as a density of sensors or a probability density. Deterministic designs approximate the desired taper by appropriately modulating the inter-sensor spacing [273, 128, 237, 101, 116, 274, 297, 265, 93, 64, 151, 281, 42], whereas stochastic designs generate sensor positions randomly from the spatial probability density defined by the taper [172, 173, 7, 251]. Typically, the beamforming weights of an array are assumed to be of constant magnitude (phase-only or isophoric weights). This reduces the possible loss in array gain compared to a uniform array with the desired amplitude tapering. The sensors of a spatially tapered array are usually placed continuously within the given domain of interest, i.e., a segment of the real line or an area in the real plane. A drawback of continuous spatial tapering is that changing the beampattern may require moving the sensors and recalibrating the array. Array calibration is a time-consuming operation requiring calibration measurements. Hence, this is impractical if the array should adapt rapidly to a dynamical propagation environment.

Sensor selection

When the sensors are constrained to a lattice, sparse array design becomes a *sensor selection* or *array thinning* problem. Here, the task is to select the best subset of sensors, based on a optimization criterion of choice. Common optimization goals are, for example, matching a desired beampattern [249, 66, 120, 148, 176, 24, 85, 125, 105], a high signal-to-interference-plus-noise ratio (SINR) [290, 291, 99], or a low mean squared error (MSE) in parameter estimation [50, 90, 267].

Depending on the optimization goal, the array configuration may be static or adaptive [98]. Dynamically changing array configurations typically use programmable switches to select a subset of sensors from the complete set of sensors. Regardless of the objective function, the resulting optimization problem is combinatorial, which implies that no polynomial-time algorithm is known for finding the global optimum. Even if solutions to moderately sized instances can be found using, e.g., branch and bound methods with judicious pruning [66], the problem becomes exceedingly (in fact, exponentially) more difficult to solve as the problem size grows. Consequently, a variety of approaches have been proposed to approximately solve the sensor selection problem, including convex relaxation techniques [125, 52, 53, 290, 267], greedy methods [290, 267], and heuristics inspired by biology or physics, such as genetic algorithms [104, 90] or simulated annealing [271]. Approaches combining aspects of discrete and continuous sensor spacing also exist [53]. For a detailed review of sensor selection in array processing see [182, Ch. 19], [231, 21] and references therein.

2.2.2 Co-array-based design

This work views sparse array design as a sensor selection problem with co-array-based optimization criteria and constraints. Specifically, Chapter 4 considers optimization problems where the goal is to maximize the size of the contiguous sum co-array, subject to constraints on the number of physical sensors or aperture. A large contiguous co-array increases the number of unambiguously resolvable sources for a given physical aperture.

Minimum-Redundancy Array

The optimal array configuration avoiding unnecessary multiplicity of the co-array elements is known as the *Minimum-Redundancy Array* (MRA) [187, 115, 31, 113, 183, 242]. In particular, the *general* MRA solves [187]

$$\underset{\mathscr{D}\subseteq\mathbb{N};\ h\in\mathbb{N}_+}{\text{maximize}}\ h \quad \text{subject to} \quad |\mathscr{D}| = N \quad \text{and} \quad \mathscr{D}-\mathscr{D} \supseteq \{0:h-1\}.$$

The *restricted* MRA instead constrains the aperture of the physical array to $L = h-1$ by requiring that $\mathscr{D}-\mathscr{D} = \{-L:L\}$. The origins of the MRA and other co-array-based array designs can be traced back to mid 20th century works in number theory [40, 68, 228, 150] and radio astronomy [185, 39, 22, 103, 38], which considered difference bases and difference co-arrays, respectively. The

MRA and other optimal configurations, such as the Minimum-Hole (Golomb) Array [33, 280, 183], suffer from the prohibitive complexity of the combinatorial array design problem. For example, restricted (difference co-array-based) MRAs are currently only known for $N \leq 26$ [242].

Scalable sparse array configurations

Due to the difficulty of finding optimal arrays for a large number of sensors, several scalable linear [206, 200, 276, 163], planar [94, 43, 166], as well as volumetric [212] array designs have been proposed in the past. Some of these configurations extend known instances of the MRA or other sparse arrays to larger apertures, such as recursive or fractal arrays [115, 59] and reduced redundancy arrays [115, 113]. Other configurations have parametric closed-form sensor positions, which enable optimizing the array geometry at a low computational cost. Two popular examples that have received a great deal of attention due to their simplicity are the previously mentioned Co-prime Array (CPA) [276] and Nested Array (NA) [200].

The CPA is parameterized by two co-prime numbers $N_1, N_2 \in \mathbb{N}$, which define the inter-sensor spacings of two subsampled *Uniform Linear Arrays* (ULAs). In particular, the set of sensor positions of the CPA is given by

$$\mathscr{D}_{\text{CPA}} \triangleq \{0 : N_1 : N_1(N_2-1)\} \cup \{0 : N_1 : N_1(N_2-1)\}.$$

The number of physical sensors of the CPA is $N_1 + N_2$, whereas the difference co-array has $\mathscr{O}(N_1 N_2)$ virtual elements [276]. Consequently, the CPA can resolve vastly more sources than sensors. The main drawback of the CPA is that its difference co-array contains holes. This limits the range of algorithms that can be applied without additional pre-processing, such as interpolation or matrix completion [4, 272, 170, 216].

In contrast to the CPA, the NA achieves a contiguous difference co-array. The set of sensor positions of the NA is defined as

$$\mathscr{D}_{\text{NA}} \triangleq \{0 : N_1 - 1\} \cup \{N_1 : N_1 + 1 : N_2(N_1+1) - 1\}.$$

Similarly to the CPA, the NA consists of two ULAs parameterized by non-negative integers $N_1, N_2 \in \mathbb{N}$, which yield a difference co-array of size $\mathscr{O}(N_1 N_2)$ using $N_1 + N_2 - 1$ physical sensors [200]. Note that N_1, N_2 need not be co-prime in case of the NA. The contiguous co-array of the NA considerably simplifies array processing and allows algorithms, such as co-array MUSIC [200, 162], to be directly applied to the whole co-array.

One disadvantage of the NA is that it contains several closely spaced sensors. This can lead to undesired mutual coupling effects, as sensors in close proximity to each other typically interact more strongly than sensors placed farther apart [163]. Consequently, several array configurations have been developed reduce the number of small sensor displacements. Notable examples include the Super Nested Array [163, 164] and MISC Array [307]. Other parametric configurations achieve a larger contiguous difference co-array than the NA. The foremost of

these is the Wichmann Array (WA) [294, 206, 160]. The WA has a contiguous difference co-array and approximately $1 - \sqrt{3}/2 \approx 13\%$ fewer sensors than the NA of equivalent (maximal) aperture [222]. In fact, for $N \geq 14$, this minimum-redundancy WA coincides the MRA, which is currently known for $N \leq 26$ [242].

Fig. 2.3 shows the ULA, (restricted) MRA, WA, NA and CPA with maximum aperture for $N = 6$ sensors. The difference co-array is uniform for all configurations except the CPA, which nevertheless has more co-array elements than the ULA. For further comparisons of these and other sparse array configurations, see, e.g., [3, 287, 135, 165, 222].

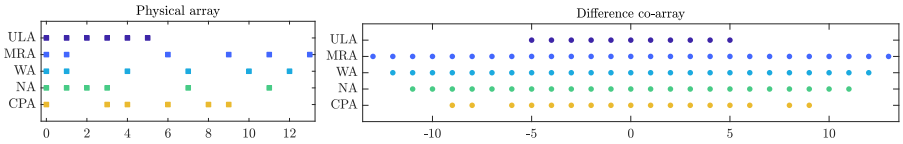

Figure 2.3. Examples of linear array configurations and the respective difference co-arrays. The sparse arrays considered in this work are thinned uniform arrays, i.e., their sensors lie on a regular grid. The normalized sensor positions can thus be conveniently represented by integers.

Alternative co-array-based design criteria

Redundancy is only one possible array design criterion, and many alternatives exist. For example, maximizing the number of total (rather than contiguous) co-array elements can provide more virtual sensors per physical sensor than an array with a contiguous co-array. However, gaps in the co-array can lead to unwanted grating lobes in the beampattern and ambiguities in the virtual array manifold (due to loss of the Vandermonde structure), which can affect imaging and parameter estimation performance. Furthermore, the virtues of uniform spatial sampling, such as simplified algorithm design, efficient processing, and predictable theoretical performance, are either irrecoverably lost or require interpolation or matrix completion techniques to be recovered [4, 272, 216].

Altogether different criteria may also be employed, such as the robustness of the array to sensor failures. For example, the k-fragility [168, 169] quantifies the probability of a change in the co-array if k physical sensors are removed uniformly at random. The MRA is maximally fragile, since all of it sensors are essential, i.e., the co-array changes if any sensor is removed. In contrast, the ULA is minimally fragile, as only its first and last sensor are essential. Hence, fragility may be decreased at the expense of an increase in redundancy. This suggests novel sparse array designs robust to sensor failures, such as the MRA with constrained fragility [167].

2.3 Direction-of-arrival estimation using the co-array

In the past decades, direction-of-arrival (DoA) estimation using sparse arrays has attracted substantial attention, due to the possibility of resolving more

sources than sensors. For example, several works have studied fundamental performance bounds, such as the Cramér-Rao Lower Bound (CRLB) in the underdetermined regime, where $K \geq N$ [2, 135, 165, 287]. The CRLB provides a lower bound for the variance of any unbiased estimator [127, Ch. 3]. The main difference between the underdetermined regime, $K \geq N$, and the conventional regime, $K < N$, is that in the former, the CRLB of the DoAs experiences an error floor. Specifically, the CRLB saturates for a fixed number of snapshots regardless of the signal-to-noise ratio (SNR) [165, Theorem 4]. This finite sample effect does not occur in the conventional regime, where the CRLB converges to zero as the SNR increases without bound for any number of snapshots [165, Theorem 3].

Optimal DoA estimation methods attaining the CRLB, such as deterministic and stochastic maximum-likelihood, usually require a multidimensional search over different combinations of potential DoA, which is computationally impractical for more than a few sources [41, 259, 215]. Consequently, computationally cheaper, but suboptimal algorithms are often employed instead. The classical Fourier approach to spatial spectrum estimation, also known as beamforming, makes minimal assumptions about the emitters, and is therefore straightforward and computationally inexpensive to employ. However, improved resolution and statistical performance may be achieved by leveraging *a priori* information about the signal sources and array geometry [256]. For example, subspace techniques such as MUSIC [240] and ESPRIT [236] decompose the measurement vector space into a signal and noise subspace similarly to maximum-likelihood methods. Both MUSIC and ESPRIT avoid the expensive multidimensional search of maximum-likelihood methods by decoupling the individual DoA estimation problems from each other.

This section reviews three widely used approaches to leveraging the difference co-array in DoA estimation. Section 2.3.1 discusses beamforming, which is the focus of this work. Sections 2.3.2 and 2.3.3 consider two alternative approaches based on compressive sensing and subspace decomposition, respectively.

2.3.1 Beamforming

Beamforming is a non-parametric form of spatial filtering, where the sensor signals are linearly combined to improve SNR. Specifically, signals impinging on the array from desired directions add constructively, creating a spatial interference pattern called a *beam* [279]. The advantages of beamforming include a low computational cost and a minimal requirement for assumptions.

In the case of the passive array model in (2.1), the output of the beamformer with beamforming weight vector $\boldsymbol{w} \in \mathbb{C}^N$ is defined as

$$y \triangleq \boldsymbol{w}^{\mathrm{H}}\boldsymbol{x} = \boldsymbol{w}^{\mathrm{H}}(\boldsymbol{A}\boldsymbol{\gamma} + \boldsymbol{n}).$$

Vector $\boldsymbol{w}$ is typically a function of the array steering vector $\boldsymbol{a}(\phi)$ in a direction of interest ϕ, as in case of the spatial matched filter $\boldsymbol{w} = \boldsymbol{a}/\|\boldsymbol{a}\|_2^2$, or the minimum variance distortionless response (MVDR) $\boldsymbol{w} = \boldsymbol{R}_x^{-1}\boldsymbol{a}/\|\boldsymbol{R}_x^{-1/2}\boldsymbol{a}\|_2^2$ [47, 143].

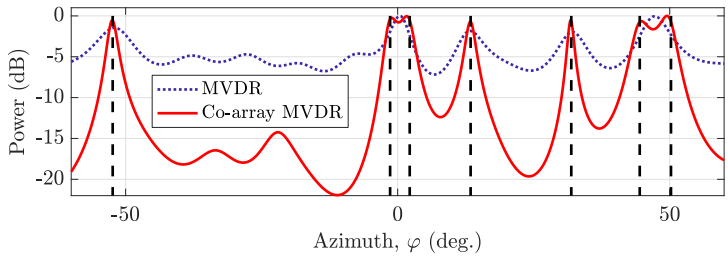

Figure 2.4. Beamformed spatial power spectrum. Co-array-based beamforming resolves all sources successfully. Simulation parameters: $N = 6$ sensor MRA and $K = 7$ uncorrelated equal power sources with DoAs $\{-52.4°, -1.4°, 2.1°, 13.4°, 31.9°, 44.5°, 50.2°\}$. The noise variance is $\sigma^2 = 7 \cdot 10^{-3}$ and the number of snapshots is $T = 2000$.

The data-dependent MVDR improves SINR compared to the data-independent matched filter, but requires inversion of the covariance matrix $\boldsymbol{R}_x$. This matrix, or its finite sample realization $\hat{\boldsymbol{R}}_x$, may be rank-deficient or ill-conditioned in practice. Hence, diagonal loading is often employed, i.e., a heuristically chosen diagonal matrix is added to $\hat{\boldsymbol{R}}_x$ prior to inversion. Diagonal loading and other robust beamforming techniques [283, 282] decrease sensitivity to model mismatch and provide numerical stability at the cost of added bias.

Assuming $\boldsymbol{w}$ is data-independent, the power of the beamformed signal is

$$\mathbb{E}(|y|^2) = (\boldsymbol{w}^* \otimes \boldsymbol{w})^{\mathrm{H}} \boldsymbol{r}_x = (\boldsymbol{w}^* \otimes \boldsymbol{w})^{\mathrm{H}} \big((\boldsymbol{A}^* \odot \boldsymbol{A}) \boldsymbol{p} + \sigma^2 \operatorname{vec}(\boldsymbol{I}) \big),$$

which is itself the output of a beamformer with weight vector $\boldsymbol{w}^* \otimes \boldsymbol{w}$ operating on the vectorized covariance matrix [200]. In general, the output of this beamformer is $\boldsymbol{w}_{\mathrm{eff}}^{\mathrm{H}} \boldsymbol{r}_x$, where $\boldsymbol{w}_{\mathrm{eff}}$ is an N^2-dimensional complex-valued effective beamforming weight vector. Vector $\boldsymbol{w}_{\mathrm{eff}}$ shapes the beamforming weights of the difference co-array, similarly to how vector $\boldsymbol{w}$ determines the beamforming weights of the physical array. The extra DoFs provided by the co-array can be leveraged in DoA estimation or imaging, as Fig. 2.4 illustrates in case of the MRA of Fig. 2.3. The beamforming weights are computed both using the conventional MVDR to obtain $\boldsymbol{w}$, and the difference co-array-based MVDR (see [200, Eq. (22)] for details) to solve for $\boldsymbol{w}_{\mathrm{eff}}$. The beamformer utilizing the co-array successfully resolves all sources, unlike the conventional beamformer. Note that the number of sources is $K = 7$, which is larger than the number of sensors $N = 6$.

The covariance matrix inevitably loses some information contained in the received signal, such as the temporal structure of the source signal waveforms $\boldsymbol{\gamma}(t)$. Consequently, in contrast to the DoAs, estimating the impinging source waveforms, which is also known as the *signal copy* problem [199], does not directly benefit from the co-array model.

An alternative approach to beamforming is also suggested by the structure of certain array configurations. In particular, sparse arrays that decompose into appropriate subarrays, such as the CPA and NA, can use the nulls in the beampattern of one subarray to cancel the grating lobes of the other. This is achieved by multiplying the beamformed outputs of the subarrays, or by using one subarray as a transmitter and the other as a receiver [276, 5, 6].

The main drawback of beamforming is its diffraction limited resolution. Although advanced beamforming techniques, such as monopulse (simultaneous lobe comparison) [29], can improve accuracy in the single target case, beamforming cannot generally resolve sources spaced closer than approximately half a beamwidth. The beamwidth is primarily determined by the array aperture. High-resolution methods may overcome this limitation by leveraging additional information about the signal model, such as the point source property, number of emitters, possible low-rank structure of the covariance matrix, or the orthogonality of signal and noise subspaces.

2.3.2 Compressive sensing

The estimation of the DoAs from (2.4) can be formulated as an optimization problem using the compressive sensing framework [74]. For example, the *on-grid sparse support recovery* problem performs simultaneous variable selection and estimation to recover the source DoAs and powers, respectively [305, 203]. This is achieved by evaluating the array response on a grid of source directions and enforcing a sparsity constraint on the unknown source power vector. The convex ℓ_1 norm is commonly employed instead of a non-convex constraint on the number of nonzero entries of the unknown vector [305, 203, 246]. The sparsity of the model can also be learned directly from the data as in sparse Bayesian learning [299, 196]. Alternatively, the original problem may be solved approximately using greedy methods, such as orthogonal matching pursuit [270]. Ultimately, the maximum number of non-zero entries in the unknown source power vector is determined by the Kruskal rank[1] of the dictionary matrix, which is upper bounded by the number of difference co-array elements [203, Lemma 3]. A sparse array with N sensors can hence resolve $\mathcal{O}(N^2)$ sources by solving a convex compressive sensing problem—with high probability even for a finite number of snapshots [138, 217].

In practice, the true source directions may not lie on the grid of candidate directions, which may lead to biased DoA estimates. This issue may be alleviated by increasing the number of grid points, allowing for off-grid sources [264], or adopting a completely gridless (continuous) approach [263, 301]. These modifications typically come at the expense of an increase in computational complexity. For example, the continuous approach, also known as super-resolution [45, 46], requires solving a semidefinite (rather than linear) program.

2.3.3 Subspace methods

Subspace methods are a prominent family of high-resolution DoA estimation techniques. This category includes algorithms such as MUSIC [240] and ESPRIT [236], as well as their co-array-based extensions [200, 253]. Maximum-likelihood methods also rely on projections to subspaces. Particularly MUSIC is

[1]The largest $i \in \mathbb{N}$, such that every subset of i columns are linearly independent.

widely-studied and applied in practice due to its ability to achieve comparable performance to the optimal maximum-likelihood estimator at a significantly lower computational cost. The estimation error of MUSIC can also be shown to approach the CRLB as the sample size or SNR goes to infinity, assuming uncorrelated sources [256].

The core idea of subspace methods is to decompose the vector space spanned by the measurement vectors in (2.1) into a signal and noise subspace. The signal subspace is spanned by the eigenvectors associated with the K largest eigenvalues of the covariance matrix $\boldsymbol{R}_x$, whereas the noise subspace is spanned by the remaining $N-K$ eigenvectors. The number of sources K may need to be estimated using model order selection techniques [258]. MUSIC exploits the orthogonality of the noise subspace and array steering matrix to identify the source DoAs by searching for the K largest peaks in the MUSIC pseudospectrum [240] or by polynomial rooting [28]. ESPRIT leverages the rotational invariance of the signal subspace when the physical array or co-array has translational invariance.

Subspace methods can resolve at most $N-1$ sources when applied to the covariance matrix of the physical array, since the rank of $\boldsymbol{R}_x$ is at most N. However, up to $\mathcal{O}(N^2)$ sources can be resolved by mapping the entries of $\boldsymbol{R}_x$ to a higher dimensional virtual measurement space supported on the difference co-array. There are several approaches to accomplishing this, including spatial smoothing [200] and covariance matrix augmentation techniques [208, 209, 2, 4, 162, 48]. Recovering the virtual (co-array) covariance from the sparse array measurements is also know as compressive covariance sensing [233, 214].

Spatial smoothing [69, Section II-B-2] was originally developed for building the rank of the covariance matrix to decorrelate coherent sources, which can severely degrade DoA estimation performance [262, 210]. The method is directly applicable to the vectorized covariance $\boldsymbol{r}_x$ in (2.4), since the source power vector $\boldsymbol{p}$ is deterministic and therefore coherent [200]. Spatial smoothing builds the rank of the virtual covariance matrix by averaging the measurements of identical, but spatially translated, subarrays of the difference co-array. The difference co-array is typically designed to be uniform in order to simplify the selection of the subarrays. A uniform co-array also guarantees that the DoAs are uniquely identified by MUSIC as the number of snapshots approaches infinity. This is due to the Vandermonde structure of the virtual array steering matrix. For details, see [255, Eq. (4.5.13)].

A drawback of co-array MUSIC and ESPRIT is that they do not generally attain the CRLB in the underdetermined regime, $K \geq N$. This limitation may be overcome by using weighted least squares to refine the estimates provided by the methods [243].

2.4 Sparse active arrays and the sum co-array

Despite the great deal of attention afforded to sparse arrays in the context of passive sensing and the difference co-array, considerably less research has been conducted on the sum co-array and active sensing. The sum co-array consists of the pairwise sensor position sums, rather than differences, and is particularly relevant in active sensing. The sum co-array also emerges in passive sensing applications with conjugate cyclostationary signaling [89]. Next, we briefly review prior works on sum co-array-based sparse array design and signal processing, as our focus is henceforth on active sensing.

2.4.1 Designs and architectures

Array configurations designed for the sum co-array are typically dissimilar to their difference co-array counterparts, due to the distinct algebraic structure of the two co-arrays. In particular, "sum MRAs" tend to have more physical sensors than "difference MRAs" with the same number of virtual co-array sensors. This is due to the commutativity of the sum, i.e., $a+b=b+a$, but $a-b\neq b-a$ for $a\neq b$. Specifically: N numbers produce at most $N+(N-1)+(N-2)+\ldots+1=N(N+1)/2$ unique sums, but $N+(N-1)+\ldots+(N-1)=N(N-1)+1$ unique differences. Covering the same set of numbers therefore requires approximately $\sqrt{2}\approx 1.414$ more sums than differences. Indeed, this seems to empirically hold for MRAs as well. For example, the sum MRA with aperture 213 (unit inter-element spacings) requires 35 sensors [132], whereas the difference MRA for the same aperture requires 25 sensors [242]. This results in a ratio of $35/25=1.4\approx\sqrt{2}$.

Surprisingly few works have considered sum MRAs since the 1990s [110, 113]. Especially the MRA with shared transmitting (Tx) and receiving (Rx) sensors (i.e., all sensors are transceivers) has received little attention in the array processing literature. Nevertheless, the mathematical structure underlying MRAs has been studied in number theory since the 1930s [232]. In the field of additive combinatorics, the linear MRA problem is informally known as the postage stamp problem [177, 191], and the respective solutions as extremal additive 2-bases (restricted or otherwise) [49, 230, 132]. However, higher dimensional extensions to the postage stamp problem remain unexplored. In particular, little is known about two-dimensional extremal additive 2-bases, which are relevant in the design of planar MRAs. Planar arrays are relevant in applications, such as volumetric imaging, where beam steering or resolution in two angular dimensions is essential.

In contrast, many works consider array configurations with independently placeable Tx and Rx sensors, which means that the two arrays can, but need not, overlap. In this case, the MRA has at least one simple closed-form solution [174, 56]. Alternative sparse array designs have also been proposed in both the linear [174, 186, 181] and planar cases [176, 24, 25]. The reason is that a low-redundancy array may not be able to synthesize the desired beampat-

tern in a single transmission when the Tx array operates in a phased array manner, i.e., all Tx sensors simultaneously transmit delayed copies of a single waveform. Non-overlapping sparse array configurations are also encountered in systems employing multiple linearly independent transmit waveforms or synthetic aperture techniques. Prime examples include MIMO (multiple-input multiple-output) radar [155, 204] and medical ultrasonography [71].

Synthetic aperture methods typically exploit either array motion [175, 225] or subarray switching [124, 126, 181] to synthesize a large virtual aperture using a reduced number of expensive front ends. Array motion provides the spatial diversity of the synthetic aperture by temporal multiplexing, and is regularly employed in, for instance, synthetic aperture radar for remote sensing [190]. Subarray switching uses a dynamically changing subset of the sensors during each transmission to a similar effect. For example, ULA subarrays on the boundary of a sparse rectangular array can be used to synthesize a desired sum co-array in a controlled manner [122, 139, 142]. Synthetic aperture and MIMO techniques can ultimately be interpreted as different physical implementations of synthesizing a desired sum co-array. That is, space or time multiplexing is used to trade off among hardware complexity, computational cost, power consumption, image acquisition time, and SNR.

A reduction in hardware costs may also be achieved without necessarily sacrificing array gain by connecting each front end and sensor via an inexpensive phase shifter. Such hybrid beamforming architectures have been extensively studied in the context of mmWave communications, where a fully digital implementation of the envisioned array configurations with many sensors and small form factors can be impractical [26, 17, 188]. Hybrid beamforming may, for similar reasons, provide useful in future sensing or imaging systems operating at up to THz frequencies [227]. However, the use of hybrid beamforming in these applications, specifically in conjunction with sparse arrays, has not been extensively investigated. Especially the active sensing case remains largely unexplored, despite some recent works on the passive case [292, 114, 96, 137]. Combining sparse arrays with hybrid beamforming has the potential to drastically reduce hardware complexity for a given aperture, or provide increased aperture and DoFs at a low cost for a given number of physical sensors. Chapter 5 explores this prospect further.

Finally, we note that if the scatterers are uncorrelated, then the difference co-array of the sum co-array is actually a more appropriate virtual array model than the sum co-array. Accordingly designed sparse array configurations can provide an increased number of DoFs [51, 293]. The sum co-array remains relevant if some of the scatterers are coherent, or estimating the required second-order statistics is prohibitive, due to a lack of computational resources or limited acquisition time.

2.4.2 Active sensing and imaging

A significant fraction of the literature on sparse active arrays focuses on linear imaging. This is partly because of the natural connection between the sum co-array and the two-way beampattern of the imaging system. Indeed, the effective beampattern is the product of the Tx and Rx beampatterns, which is the Fourier transform of the convolution of the Tx and Rx beamforming weights [250]. The output of the convolution can in turn be interpreted as a virtual beamforming weight function supported on the sum co-array [111]. Hence, a desired two-way beampattern can be synthesized by appropriately choosing the Tx and Rx array configurations and beamforming weights.

Since the tasks of designing the Tx/Rx arrays and the effective beampattern are fundamentally coupled, many works tackle the two problems jointly. Typical approaches using heuristic designs [176, 24, 25] or polynomial factorization [186, 56] consider the effective beampatterns achievable using a single set of transmit and receive beamforming weights. However, by allowing for multiple transmissions, or by using synthetic aperture or waveform diversity techniques, it is possible to synthesize any set of virtual beamforming weights supported on the sum co-array, thereby extending the range of beampatterns achievable by a given array configuration [111, 9, 181]. This decouples the array and beampattern design problems to a certain degree, which considerably simplifies both tasks.

Active sensing and imaging leveraging the sum co-array is obviously not limited to linear processing. For example, convolutional beamforming [57, 60, 180] synthesizes the sum co-array in receive-only beamforming by multiplying channel outputs with each other, similarly to the other multiplicative beamforming methods [276, 5, 6] mentioned in Section 2.3.1. Non-linear beamforming has the advantage of avoiding the multiple transmissions that may be required by linear methods to achieve a desired co-array weighting. Compressive sensing techniques [35, 213] or subspace methods [112, 193] can also improve the resolution and statistical performance similarly to the passive sensing case.

In this thesis, we focus on linear processing with multiple component images, which may correspond to separate transmissions depending on the employed system architecture. We separately consider the tasks of designing minimally redundant array configurations achieving a large uniform sum co-array in Chapter 4, and optimizing the beamforming weights to achieve a desired co-array weighting using a minimum number of component images in Chapter 5. In the next chapter, however, we present the active array signal model and establish some necessary definitions.

3. Active sensing sensor array model

A sensor array for active sensing consists of a transmitting and a receiving array. As illustrated in Fig. 3.1a, the transmitter (Tx) actively probes the environment by radiating a waveform from each sensor. The waveforms can be either fully correlated, partially correlated, or uncorrelated depending on the architecture of the transmitter. The propagating wavefield is backscattered from objects, generally referred to as *scatterers*, with a differing impedance from the propagation medium, before being observed at the receiving (Rx) array. Typical active sensing applications include radar [248], microwave imaging [13], sonar [131], and diagnostic ultrasound [179, 261].

This chapter introduces the sensor array model for active sensing in detail. Section 3.1 outlines the main assumptions underlying the the received signal model, which is presented in Section 3.2. Section 3.3 discusses various array architectures emerging from typical system design choices. Section 3.4 examines the sum co-array model arising from the received signal model, and describes its role in active sensing. Section 3.5 concludes the chapter by discussing some extensions and connections to the presented signal model.

3.1 Assumptions

Before deriving the signal model in Section 3.2, we introduce a few simplifying and commonly used assumption in active sensing. The purpose of these standard assumptions is to strike a balance between the generality of the model and the accessibility of the presentation—bearing in mind that our aim is to ultimately present the sum co-array concept in Section 3.4. Most importantly, we omit delay (range) and Doppler shift that are typical parameters of interest in radar, and focus on the angular domain (azimuth and elevation) instead. We also restrict our exposition to scalar wavefields, such as pressure fields or fields of polarized electromagnetic radiation. We do not consider path loss, fading, higher-order reflections (Born approximation), or signal dependent noise, such as clutter or interference. Extensions and relaxations to the signal model are briefly considered in Section 3.5 and Appendix A.2.

The main assumptions of this work are (see also Fig. 3.1):

(A1) Narrowband transmitted waveforms

(A2) K coherent far field point scatterers with reflectivities $\{\gamma_k\}_{k=1}^{K} \subseteq \mathbb{C}$

(A3) Co-located planar Tx and Rx arrays with sensors on a regular grid

(A4) Ideal omnidirectional sensors that do not interact with each other

(A5) Spatio-temporally white Rx noise, following a circularly symmetric complex normal distribution with zero mean and covariance $\sigma^2 \boldsymbol{I}$.

Assumption (A1) follows from the fact that the carrier frequency is typically much larger than the bandwidth of transmitted pulse, which implies that signals do not decohere across the array. A common rule of thumb is that the bandwidth is less than a few percent of the carrier frequency[1]. Under the narrowband assumption, the true frequency dependent array response may be approximated by the narrowband response at the carrier wavelength, which considerably simplifies the signal model.

By (A2), the scattering coefficients stay fixed during the coherent processing interval, or *coherence time* of the scene. This is similar, although not identical, to the Swerling I fluctuation model, which assumes constant power radar target returns between pulses in the same coherent processing interval [260]. The coherence time may consist of one or several pulses, depending on how rapidly the scattering environment changes. The scatterers are also assumed to be located in the far field of the transmitter and receiver, such that the plane wave approximation holds.

By (A3), the Tx and Rx arrays are located spatially close to each other, such that both arrays observe the same scatterer directions/scattering coefficients, and phase coherence at the receivers is possible. This is akin to monostatic or co-located MIMO radar [155], and contrary to (statistical) MIMO radar with widely separated transmitters and receivers [32, 152, 73, 97]. The Tx and Rx arrays do not necessarily overlap, but may have distinct sensors and front ends (see Section 4.1.1). Both the Tx and Rx sensors lie on a planar regular grid or lattice, such that the sensor positions in $\mathbb{R}^2$ can be conveniently written as the product of a 2×2 real-valued matrix $\boldsymbol{\Delta}$ and a 2-dimensional integer-valued vector $\boldsymbol{d}_\xi$. In particular, $\boldsymbol{d}_{\xi,n} \in \mathscr{D}_\xi$ denotes the normalized position of the nth Tx or Rx sensor, where $\mathscr{D}_\xi$ is the set of Tx or Rx sensors. Subscript "ξ" is shorthand for both "t" (Tx) and "r" (Rx), henceforth used to avoid repetition. Matrix $\boldsymbol{\Delta} \in \mathbb{R}^{2\times 2}$ defines the lattice, which is assumed rectangular. This yields the diagonal matrix

$$\boldsymbol{\Delta} = \begin{bmatrix} \delta_x & 0 \\ 0 & \delta_y \end{bmatrix},$$

[1] A more rigorous definition of narrowband involves comparing the noise variance and the second largest eigenvalue of the single-source Rx covariance matrix [303].

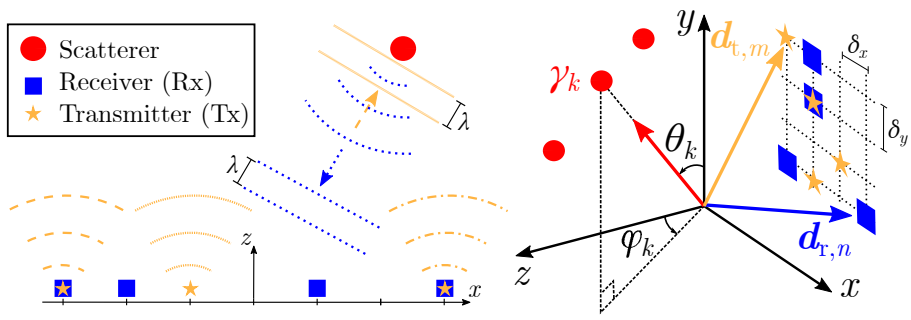

(a) Active sensing

(b) Geometry of active array

Figure 3.1. Active array model. (a) Each Tx sensor transmits a narrowband waveform, which is then backscattered from a set of far field point scatterers before being measured at the Rx sensors. (b) The Tx and Rx arrays are planar, with sensors located on a rectangular grid in the xy-plane, where δ_x and δ_y are the unit inter-sensor spacings.

where, $\delta_x, \delta_y \in \mathbb{R}_+$ are the unit spacings of the grid in the x and y dimensions. Typically, aliasing due to spatially sampling the observed wavefields is avoided by setting $\delta_x \leq \lambda/2$ and $\delta_y \leq \lambda/2$.

By (A4), the Tx or Rx array *steering vector*, which characterizes the array's (narrowband) response at the carrier wavelength λ, simplifies to

$$\boldsymbol{a}_\xi(\boldsymbol{v}_k) = \exp\left(j2\pi/\lambda \boldsymbol{v}_k^{\mathrm{T}} \boldsymbol{\Delta} \boldsymbol{d}_{\xi,n}\right). \tag{3.1}$$

Here, $\boldsymbol{v}_k \in \mathbb{R}^2$ is the direction of the kth scatterer projected to the sensor plane,

$$\boldsymbol{v}_k = \begin{bmatrix} \sin\varphi_k \sin\theta_k & \cos\theta_k \end{bmatrix}^{\mathrm{T}},$$

parameterized by an azimuth angle $\varphi_k \in [-\pi/2, \pi/2]$ and an elevation angle $\theta_k \in [0, \pi]$ as illustrated in Fig. 3.1b. Collecting the steering vectors corresponding to the K scatterers yields the Tx/Rx *steering matrix* $\boldsymbol{A}_\xi \triangleq [\boldsymbol{a}_\xi(\boldsymbol{v}_1), \ldots, \boldsymbol{a}_\xi(\boldsymbol{v}_K)]$, whose (n,k)th entry (n is the sensor and k the scatterer index) is given by

$$\left[\boldsymbol{A}_\xi\right]_{n,k} = \exp\left(j2\pi/\lambda \boldsymbol{v}_k^{\mathrm{T}} \boldsymbol{\Delta} \boldsymbol{d}_{\xi,n}\right). \tag{3.2}$$

Finally, (A5) accounts for thermal receiver noise, which is commonly assumed to be white and Gaussian. As a consequence, the noise statistics remain unaffected by matched filtering of the received signal.

3.2 Signal model

We consider a generic MIMO array with digital, hybrid or analog Tx and Rx beamforming architectures. The array consists of N_{t} transmitters, N_{r} receivers, and $M_\xi \leq N_\xi$ Tx/Rx front ends. Let $N_s \leq M_{\mathrm{t}}$ denote the number of transmitted waveforms represented by the waveform matrix $\boldsymbol{S} \in \mathbb{C}^{N_s \times T}$, where T is the waveform length in samples. Assuming w.l.o.g. that the waveforms are linearly independent, we define the Hermitian positive definite (full rank) $N_s \times N_s$

waveform cross-correlation matrix

$$\boldsymbol{R}_s \triangleq \boldsymbol{S}\boldsymbol{S}^{\mathrm{H}}. \tag{3.3}$$

Hence, the received data after matched filtering becomes (see Appendix A.1)

$$\boldsymbol{X} = \boldsymbol{F}_{\mathrm{r}}^{\mathrm{T}}(\boldsymbol{A}_{\mathrm{r}}\boldsymbol{\Gamma}\boldsymbol{A}_{\mathrm{t}}^{\mathrm{T}}\boldsymbol{F}_{\mathrm{t}}\boldsymbol{C}_s\boldsymbol{R}_s + \boldsymbol{N}\boldsymbol{S}^{\mathrm{H}}), \tag{3.4}$$

where $\boldsymbol{F}_\xi \in \mathbb{C}^{N_\xi \times M_\xi}$ is an analog Tx/Rx preprocessing matrix[2] determined by the architecture of the transmitter and receiver (see Section 3.3 for details). Furthermore, $\boldsymbol{C}_s \in \mathbb{C}^{N_{\mathrm{t}} \times N_s}$ is a digital *waveform mixing matrix*. Matrices $\boldsymbol{R}_s$, $\boldsymbol{F}_\xi$ and $\boldsymbol{C}_s$ have full column rank and are fixed for the duration of the pulse. We distinguish between these three matrices because $\boldsymbol{F}_\xi$ is typically a constrained matrix (cf. Section 3.3.2), and the $N_{\mathrm{t}} \times N_{\mathrm{t}}$ *effective* Tx sensor cross-correlation matrix $\boldsymbol{F}_{\mathrm{t}}\boldsymbol{C}_s\boldsymbol{R}_s\boldsymbol{C}_s^{\mathrm{H}}\boldsymbol{F}_{\mathrm{t}}^{\mathrm{H}}$ is rank deficient when $N_s < M_{\mathrm{t}}$.

The spatio-temporally white receiver noise is modeled by Gaussian matrix $\boldsymbol{N} \in \mathbb{C}^{N_{\mathrm{r}} \times T}$ with identically and independently distributed (i.i.d.) entries. Scattering coefficient matrix $\boldsymbol{\Gamma} = \mathrm{diag}(\boldsymbol{\gamma})$ with diagonal $\boldsymbol{\gamma} \in \mathbb{C}^K$ contains the K scattering coefficients. The received data after prewhitening can then be expressed as the $M_{\mathrm{r}}N_s$-dimensional vector

$$\boldsymbol{x} = \left(\boldsymbol{F}_{\mathrm{t}}\boldsymbol{C}_s\boldsymbol{R}_s^{1/2} \otimes \boldsymbol{F}_{\mathrm{r}}(\boldsymbol{F}_{\mathrm{r}}^{\mathrm{H}}\boldsymbol{F}_{\mathrm{r}})^{-1/2}\right)^{\mathrm{T}}(\boldsymbol{A}_{\mathrm{t}} \odot \boldsymbol{A}_{\mathrm{r}})\boldsymbol{\gamma} + \boldsymbol{n}. \tag{3.5}$$

In particular, (3.5) follows from applying the Kronecker and Khatri-Rao identities in Section 1.5, and premultiplying the vectorized data matrix $\mathrm{vec}(\boldsymbol{X})$ by the prewhitening matrix $\left(\boldsymbol{R}_s^{-1/2} \otimes (\boldsymbol{F}_{\mathrm{r}}^{\mathrm{H}}\boldsymbol{F}_{\mathrm{r}})^{-1/2}\right)^{\mathrm{T}}$. Here $\boldsymbol{R}_s^{1/2}$ denotes the unique positive definite square-root matrix satisfying $\boldsymbol{R}_s^{\mathrm{H}/2}\boldsymbol{R}_s^{1/2} = \boldsymbol{R}_s^{1/2}\boldsymbol{R}_s^{1/2} = \boldsymbol{R}_s$. By (A5), vector $\boldsymbol{n} \sim \mathcal{CN}(\boldsymbol{0}, \sigma^2\boldsymbol{I})$ is white and normally distributed. We refer to (3.5) as the *general* MIMO model. Section 3.3 considers special cases of this general model—specifically, choices affecting matrices $\boldsymbol{F}_{\mathrm{t}}, \boldsymbol{F}_{\mathrm{r}}$, and $\boldsymbol{R}_s$.

3.3 System design parameters and trade-offs

The overall complexity and performance of both the transmitter and receiver is influenced by a handful of design parameters. In particular, the choice of the Tx/Rx *beamforming architecture* and the degree of *waveform diversity* have a major impact on the received signal model in (3.5). The beamforming architecture broadly refers to the pre-processing network of radio and intermediate frequency (RF-IF) components connecting the Tx or Rx sensors to digital channel inputs or outputs. Beamforming can be interpreted as spatial filtering operation that focuses energy at transmission in, or observes signals at reception from desired directions. In terms of (3.5), the beamforming architecture determines the structure and dimensions of the analog Tx and Rx preprocessing matrices $\boldsymbol{F}_{\mathrm{t}}$

[2] We use the unconjugated transpose (somewhat against convention) to simplify notation by avoiding conjugation when applying Kronecker and Khatri-Rao product identities.

and $\boldsymbol{F}_{\mathrm{r}}$. Waveform diversity refers to the number of waveforms and their relative correlations, which determine the dimensions and properties of the correlation matrix $\boldsymbol{R}_s$. We now briefly discuss both of these design aspects in more detail, and review typical array architectures considered in the literature.

3.3.1 Beamforming architecture

The beamforming architecture is largely dictated by the manufacturing and operational costs of the array. The costs in turn mainly depend on the number of Tx and Rx front ends, which determines the required number of RF-IF components and analog-to-digital or digital-to-analog converters (ADCs and DACs). Since these components are typically expensive and power-hungry—especially at higher frequencies [226, p. 128]—it may be impractical to have a dedicated digital channel that requires a separate front end for each sensor in the array. Many modern applications in radar, communications, and imaging require a large number of sensors and front ends because of high spatial resolution requirements.

A completely digital beamforming architecture has the advantage of simple and flexible signal processing, whereas a completely analog architecture is inexpensive and energy efficient. *Hybrid* beamforming trades off between the flexibility provided by digital processing and the cost efficiency of analog processing [188, 12]. Hybrid beamforming architectures reduce the number of front ends, and offset the resulting performance loss using an analog preprocessing network of phase shifters.

Fig. 3.2 illustrates the general beamforming architecture. The N_ξ-dimensional hybrid beamforming weight vector can be written as

$$\boldsymbol{w}_\xi = \boldsymbol{F}_\xi \boldsymbol{c}_\xi, \tag{3.6}$$

where $\boldsymbol{F}_\xi$ is an $N_\xi \times M_\xi$ analog beamforming matrix, $\boldsymbol{c}_\xi$ is an M_ξ-dimensional digital beamforming vector, and M_ξ is the number of Tx or Rx front ends. Depending on the value of M_ξ, the beamforming architecture is called

- *fully digital*, if $M_\xi = N_\xi$
- *hybrid*, if $1 < M_\xi < N_\xi$
- *fully analog*, if $M_\xi = 1$

In the fully digital case, the analog beamforming network is absent, and matrix $\boldsymbol{F}_\xi$ equals the identity matrix. In the hybrid case, $\boldsymbol{F}_\xi$ is a matrix of complex exponentials. In the fully analog case, this analog beamforming matrix reduces to an N_ξ-dimensional vector $\boldsymbol{f}_\xi$.

The phase shifters in the analog beamforming network typically have finite phase quantization in order conserve power and reduce costs. Consequently, the entries of $\boldsymbol{F}_\xi$ belong to a finite alphabet. Specifically, $\boldsymbol{F}_\xi \in \mathscr{F}_\xi(B) \subset \mathbb{C}^{N_\xi \times M_\xi}$,

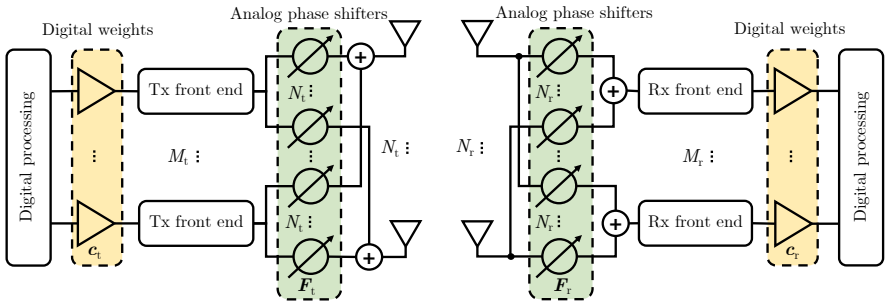

(a) Transmitter **(b)** Receiver

Figure 3.2. General beamforming architecture. The cost of the array may be lowered by reducing the number of front ends and employing an analog preprocessing network of phase shifters. Adapted from Publication VIII, Fig. 1 © 2020 IEEE.

where the set of feasible Tx/Rx phase shift matrices is defined as

$$\mathscr{F}_\xi(B) \triangleq \left\{ \exp(j\boldsymbol{\Phi}) \mid \boldsymbol{\Phi} \in \mathbb{R}^{N_\xi \times M_\xi}, \Phi_{nm} \in \Phi(B) \right\}. \tag{3.7}$$

Here B denotes the number of bits used to uniformly quantize the phase between 0 and 2π. This results in the set of discrete phases

$$\Phi(B) \triangleq \left\{ 0, 2\pi/2^B, \ldots, (2^B - 1)2\pi/2^B \right\}. \tag{3.8}$$

Section 5.3 considers the fully digital, hybrid, and fully analog beamforming architectures in further detail.

3.3.2 Waveform diversity

In the context of this work, *waveform diversity* refers to the number of transmit waveforms and their mutual correlations (see [34] for a broader definition, including, e.g., the ability to change or optimize the waveforms between pulses). In particular, waveform diversity manifests itself in the general MIMO signal model (3.5) in the form of the full rank $N_s \times N_s$ matrix $\boldsymbol{R}_s$. Waveform diversity also indirectly influences the Tx and Rx architectures, by constraining the minimum number of Tx/Rx front ends and matched filters. In this work, we consider the extreme cases of *coherent* (fully correlated) and *uncorrelated* transmission. These correspond to the canonical *phased array* and *orthogonal MIMO array* models, which have the following received signal models.

1. **Phased array (PA)**, i.e., coherent transmission:

$$\boldsymbol{x} = \left(\boldsymbol{w}_\mathrm{t} \otimes \boldsymbol{F}_\mathrm{r} (\boldsymbol{F}_\mathrm{r}^\mathrm{H} \boldsymbol{F}_\mathrm{r})^{-1/2} \right)^\mathrm{T} (\boldsymbol{A}_\mathrm{t} \odot \boldsymbol{A}_\mathrm{r}) \boldsymbol{\gamma} + \boldsymbol{n}. \tag{3.9}$$

   The PA transmits a scaled and phase shifted copy of a single ($N_s = 1$) waveform from each Tx element. Consequently, the waveform correlation matrix reduces to a scalar. For convenience, let the transmitted waveform have unit power, $R_s = 1$. Similarly, the transmit beamforming matrix simplifies to a vector $\boldsymbol{w}_\mathrm{t} \in \mathbb{C}^{N_\mathrm{t}}$ following (3.6).

2. **Orthogonal MIMO (O-MIMO)**, i.e., uncorrelated transmission:

$$\boldsymbol{x} = (\boldsymbol{A}_{\mathrm{t}} \odot \boldsymbol{A}_{\mathrm{r}})\boldsymbol{\gamma} + \boldsymbol{n}. \tag{3.10}$$

   The O-MIMO array launches mutually orthogonal waveforms from each Tx element, which implies that $N_s = N_{\mathrm{t}}$ and $\boldsymbol{F}_{\mathrm{t}} = \boldsymbol{C}_s = \boldsymbol{R}_s = \boldsymbol{I}$. Typically, the receiver is also assumed to be fully digital, such that $\boldsymbol{F}_{\mathrm{r}} = \boldsymbol{I}$.

The intermediate form of the PA and O-MIMO schemes corresponds to *partially correlated* transmit waveforms that may be used to design arbitrary Tx beampatterns. The PA is predominantly considered in radar and medical ultrasound applications [248, Chapter 8], [261, Chapter 7], whereas the O-MIMO model has been extensively studied in the context of MIMO radar [155]. For example, see [1, 77, 63, 80] for a comparison of the advantages and disadvantages of PA and O-MIMO in radar. In general, the relevant model is application dependent and primarily determined by the (i) required SNR or Tx combining gain, (ii) dynamics of the scattering scene or tolerated scan time, and (iii) constraints on the Tx/Rx architecture or cost of the array. Another important factor is the available DoFs [32, 158], which determines the number of identifiable scatterers or sources—an aspect Section 3.4 discusses in more detail. We briefly elaborate Items (i) to (iii) below. The main points are summarized in Table 3.1.

(i) SNR: The PA applies Tx beamforming to spatially focus the radiated wavefield and enhance the SNR of the received signal [157]. In contrast, the O-MIMO transmitters operate in a space-multiplexed manner.[3] As a result, the full $N_{\mathrm{r}}N_{\mathrm{t}}$-dimensional virtual measurement vector is accessed in a single pulse-echo cycle. This is achieved at the expense of reduced SNR (for a fixed Tx power), due to lack of Tx combining gain. The Rx combining gain, which also affects the SNR, is equal for both the PA and O-MIMO models.

(ii) Scan time: On one hand, the PA experiences an SNR gain when the Tx beam is focused on a scatterer of interest. This is the case, e.g., for a target tracking radar. However, if the beam is directed in a direction absent of scatterers, or multiple beams are formed, the potential combining gain of Tx beamforming is lost. This may occur when a radar is searching for and resolving targets, instead of tracking or imaging them. On the other hand, O-MIMO illuminates the whole scattering scene in a single pulse, which results in a more evenly distributed spatial power density. This may be an attractive feature in environments with rapidly varying dynamics, strong scatterers, or a large number of targets of interest.

(iii) Architecture: The hardware requirements of O-MIMO are more stringent than those of the PA, due to the need for multiple matched filters at the

[3] Time-multiplexing is also possible by transmitting the same waveform sequentially from each transmitter within the coherence time of the scene [112, 77, 8, 35].

Table 3.1. Comparison of canonical active array models. The phased array offers improved Tx combining gain and flexibility in the choice of beamforming architecture, whereas the orthogonal MIMO array fully utilizes waveform diversity.

Model	SNR	Scan time	Architecture	Eq.
PA	$\propto N_{\mathrm{t}}$	$\propto$ Beamwidth^{-1}	No constraints	(3.9)
O-MIMO	1	1	Fully digital Tx (and Rx)	(3.10)

receiver and a fully digital transmit beamforming architecture. O-MIMO implicitly assumes that the transmitter has N_{t} RF-IF front ends, since an independent waveform is launched from each Tx element. This is in stark contrast to the PA, which can have a fully analog beamforming architecture, since only one waveform is transmitted.

The various advantages and disadvantages of the PA and O-MIMO schemes may also be traded off by allowing for correlated waveforms [155, 86, 154, 102, 14]. The number of linearly independent waveforms should nevertheless be less than or equal to the number of Tx front ends M_{t}, if the transmitting array has a hybrid beamforming architecture.

3.4 Sum co-array

The co-array is a virtual array model arising from the structure of the array manifold. It controls key aspects of the array performance, such as the effective point spread function, and the number of identifiable scatterers or sources. We focus on the sum co-array, which is of particular interest in active sensing.

3.4.1 Effective steering matrix and sum co-array

The received signal of the O-MIMO model in (3.10) may be interpreted as the received signal of a virtual array with the *effective* steering matrix $\boldsymbol{A}_{\mathrm{t}} \odot \boldsymbol{A}_{\mathrm{r}}$. This matrix has many more rows ($N_{\mathrm{t}}N_{\mathrm{r}}$) than either the Tx or Rx steering matrix (N_{t} and N_{r}). Clearly, the number of unique (noiseless) equations is upper bounded by the product $N_{\mathrm{t}}N_{\mathrm{r}}$, rather than the sum $N_{\mathrm{t}} + N_{\mathrm{r}}$, which is the maximum number of unique physical sensors. This is also the case in the general MIMO model (3.5), where we observe linear combinations of the outputs of this virtual array, due to the possibly hybrid or analog Tx/Rx architecture and lack of full waveform diversity. Specifically, if $M_{\mathrm{r}} < N_{\mathrm{r}}$ or $N_s < N_{\mathrm{t}}$, then multiple pulses may be required to obtain the full virtual array output. In any case, by (3.2), the entries of the effective steering matrix are

$$\left[\boldsymbol{A}_{\mathrm{t}} \odot \boldsymbol{A}_{\mathrm{r}}\right]_{(m-1)N_{\mathrm{r}}+n,k} = \exp\left(j2\pi/\lambda \boldsymbol{v}_k^{\mathrm{T}} \boldsymbol{\Delta}(\boldsymbol{d}_{\mathrm{t},m} + \boldsymbol{d}_{\mathrm{r},n})\right), \tag{3.11}$$

where the set of pairwise sums of the element positions is called the *sum co-array*[4] [111]. The sum co-array is defined as the set

$$\mathscr{D}_\Sigma \triangleq \mathscr{D}_\mathrm{t} + \mathscr{D}_\mathrm{r} = \left\{ \boldsymbol{d}_{\mathrm{t},m} + \boldsymbol{d}_{\mathrm{r},n} \mid \boldsymbol{d}_{\mathrm{t},m} \in \mathscr{D}_\mathrm{t};\ \boldsymbol{d}_{\mathrm{r},n} \in \mathscr{D}_\mathrm{r} \right\}, \tag{3.12}$$

which by (A3) is supported on the lattice $\mathbb{Z}^2$ (or conversely $\mathbb{N}^2$, if $\mathscr{D}_\xi \subseteq \mathbb{N}^2$). As more than one sensor pair may contribute to the same co-array element, the number of repetitions of sum co-array element $\boldsymbol{d}_\Sigma \in \mathscr{D}_\Sigma$ may be expressed as

$$v_\Sigma(\boldsymbol{d}_\Sigma) \triangleq \sum_{\boldsymbol{d}_{\xi,i} \in \mathscr{D}_\xi} \mathbb{1}\left(\boldsymbol{d}_{\mathrm{t},m} + \boldsymbol{d}_{\mathrm{r},n} = \boldsymbol{d}_\Sigma\right). \tag{3.13}$$

This is known as the *multiplicity function* or the (co-array) weight function [200].

Example 3.1 (Sum co-array)**.** *Consider a linear array with two sensors acting as both transmitters and receivers (transceivers):* $\mathscr{D}_\mathrm{t} = \mathscr{D}_\mathrm{r} = \{0, 1\}$*. The sum co-array consists of four pairwise sums of which* $|\mathscr{D}_\Sigma| = 3$ *are unique. The elements of the sum co-array, and their respective multiplicities, are* $\mathscr{D}_\Sigma = \{0+0, 0+1, 1+0, 1+1\} = \{0, 1, 2\}$*,* $v_\Sigma(0) = v_\Sigma(2) = 1$*, and* $v_\Sigma(1) = 2$*.*

Two distinct array configurations are *sum co-array equivalent* if they have the same sum co-array $\mathscr{D}_\Sigma$. Their multiplicity functions v_Σ need not be equal. A sum co-array equivalent array can always be constructed by simply swapping the positions of the Tx and Rx sensors. In this case, the modified and original array will also have the same multiplicity functions.

3.4.2 Degrees of freedom and aspect ratio

The total number of DoFs in the defined array model is given by the number of unique sum co-array elements $N_\Sigma \triangleq |\mathscr{D}_\Sigma|$. Moreover, the number of *contiguous* DoFs, H_Σ, equals the number of virtual elements in the largest rectangle of contiguous lattice points embedded in the sum co-array. Denoting the dimensions of this rectangle as h_x and h_y, and the respective offset vector as $\boldsymbol{l} \in \mathbb{N}^2$, we have

$$H_\Sigma \triangleq \max_{h_x, h_y \in \mathbb{N};\ \boldsymbol{l} \in \mathbb{Z}^2} \left(h_x h_y \;\middle|\; \{0 : h_x - 1\} \times \{0 : h_y - 1\} + \boldsymbol{l} \subseteq \mathscr{D}_\Sigma \right). \tag{3.14}$$

The sum co-array is *contiguous* if $H_\Sigma = N_\Sigma$. A contiguous co-array is also called uniform, gapless, or hole-free. In the one-dimensional (linear array) case, H_Σ equals the position of the first gap in the sum co-array, provided that the first virtual element of the co-array is located at the origin.

The main advantage of a contiguous co-array is that it maximizes the number of total DoFs for a given physical aperture. It also facilitates the use of many array processing algorithms designed for uniform arrays. For example, co-array MUSIC [200, 162] leverages the Vandermonde structure of the virtual

[4] In the nomenclature of MIMO radar, this is typically called the *virtual array* [156, p. 240]. However, we use the terms virtual array and sum co-array interchangeably, since they are mathematically equivalent.

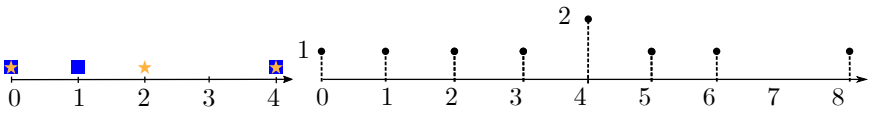

(a) Tx (★) & Rx (■) array **(b)** Sum co-array

Figure 3.3. Physical array and its sum co-array. The sum co-array becomes contiguous by adding a Tx or Rx sensor at position 3 of the physical array in (a). The transmitters and receivers are interchangeable in terms of achieving the same sum co-array in (b).

array steering matrix to identify more sources than sensors unambigously in the asymptotic (infinite snapshot) regime, as discussed in Section 2.3.3. Consequently, a large H_Σ is desirable even when the sum co-array is non-contiguous.

Example 3.2. *(Degrees of freedom) Fig. 3.3 shows a linear array, whose sum co-array has a gap at position* 7*. The total DoFs is* $N_\Sigma = 8$*, whereas the contiguous DoFs is* $H_\Sigma = 7$*. The sum co-array becomes contiguous by adding a transmitter or receiver at position* 3 *of the physical array.*

Also the dimensions of the co-array are relevant, as they determine the achievable resolution in azimuth and elevation. For example, air-surveillance radars typically require higher resolution in azimuth than in elevation [248, pp. 536–541]. Along with H_Σ, the size of the largest contiguous subarray contained in the sum co-array is most conveniently described by its *aspect ratio*, defined as

$$\rho \triangleq \frac{h_y}{h_x}. \tag{3.15}$$

Assuming w.l.o.g. that $h_y \leq h_x$, yields $\rho \in (0,1]$, where $\rho = 1/h_x$ corresponds to a linear co-array and $\rho = 1$ to a square co-array. Generally, the aspect ratio of the co-array, or the largest contiguous subarray thereof, is of primary interest, since a multitude of Tx or Rx arrays with wildly differing physical aspect ratios can be co-array equivalent. Only when the Tx and Rx arrays are identical and the sum co-array is contiguous, is (3.15) guaranteed to equal the aspect ratio of the physical array—approximately for finite h_x, h_y and exactly as $h_x \to \infty$. Specifically, if the side lengths of the physical array are L_x and L_y, then the aspect ratio of the co-array is $\rho = (2L_y+1)/(2L_x+1)$, whereas the aspect ratio of the physical array is $(L_y+1)/(L_x+1)$.

3.4.3 Co-array selection and steering matrices

The effective array steering matrix can be conveniently expressed as[5]

$$\boldsymbol{A}_\mathrm{t} \odot \boldsymbol{A}_\mathrm{r} = \boldsymbol{\Upsilon}^\mathrm{T} \boldsymbol{A}_\Sigma, \tag{3.16}$$

where $\boldsymbol{\Upsilon}$ is the $N_\Sigma \times N_\mathrm{r} N_\mathrm{t}$ binary *sum co-array selection matrix*, defined as

$$\Upsilon_{n,m} = \begin{cases} 1, \text{ if } \boldsymbol{d}_{\Sigma,n} = \boldsymbol{d}_{\mathrm{t},\lceil m/N_\mathrm{r} \rceil} + \boldsymbol{d}_{\mathrm{r},1+(m-1) \bmod N_\mathrm{r}} \\ 0, \text{ otherwise,} \end{cases} \tag{3.17}$$

[5]The assumption of omnidirectional sensors (A4) is *sufficient* for (3.16) to hold.

and $\boldsymbol{A}_\Sigma$ is the $N_\Sigma \times K$ *sum co-array steering matrix* with entries

$$\left[\boldsymbol{A}_\Sigma\right]_{m,k} = \exp\left(j2\pi/\lambda \boldsymbol{v}_k^{\mathrm{T}} \boldsymbol{\Delta} \boldsymbol{d}_{\Sigma,m}\right). \tag{3.18}$$

The N_Σ elements of the sum co-array $\{\boldsymbol{d}_{\Sigma,l}\}_{l=1}^{N_\Sigma} = \mathscr{D}_\Sigma$ are sorted in ascending order, such that, $\|\boldsymbol{d}_{\Sigma,1}\|_2 \leq \|\boldsymbol{d}_{\Sigma,2}\|_2 \leq \ldots \leq \|\boldsymbol{d}_{\Sigma,N_\Sigma}\|_2$. If the sum co-array is linear and contiguous, then $\boldsymbol{A}_\Sigma$ is a Vandermonde matrix. Moreover, if the sum co-array is non-redundant, then $\boldsymbol{\Upsilon}$ reduces to the identity matrix. In general, $\boldsymbol{\Upsilon}$ satisfies the identity

$$\boldsymbol{\Upsilon}\boldsymbol{\Upsilon}^{\mathrm{T}} = \mathrm{diag}(\boldsymbol{v}_\Sigma), \tag{3.19}$$

where $\boldsymbol{v}_\Sigma \triangleq [v_\Sigma(\boldsymbol{d}_{\Sigma,1}), \ldots, v_\Sigma(\boldsymbol{d}_{\Sigma,N_\Sigma})]$ is a vector containing the multiplicities of the sum co-array elements, per (3.13).

Example 3.3 (Selection matrix)**.** *Recall the two element array of Example 3.1. In this case, matrix* $\boldsymbol{\Upsilon}$*, which maps each pairwise sum to a (unique) co-array element assumes the form*

$$\boldsymbol{\Upsilon} = \begin{bmatrix} 1 & 0 & 0 & 0 \\ 0 & 1 & 1 & 0 \\ 0 & 0 & 0 & 1 \end{bmatrix}.$$

It follows that $\boldsymbol{\Upsilon}\boldsymbol{\Upsilon}^{\mathrm{T}} = \mathrm{diag}([1,2,1])$*, where the diagonal contains the multiplicities of the sum co-array elements.*

3.5 Extensions

We conclude the chapter by discussing an extension of the presented signal model to range-Doppler processing. We also shortly consider the connection between the active and passive array models. Appendix A.2 examines the effects of relaxing the signal model assumptions in Section 3.1.

Extension to range-Doppler processing

The co-array mainly affects the resolution of the array in the azimuth-elevation domain. In contrast, properties of the transmitted waveforms are key in determining the range-Doppler resolution, which is characterized by the matrix-valued delay-Doppler ambiguity function [79]

$$\boldsymbol{R}_s(\Delta\tau, \Delta\omega) \triangleq \int_0^{T_\mathrm{p}} \boldsymbol{s}(t-\Delta\tau)\boldsymbol{s}^{\mathrm{H}}(t) e^{-j\Delta\omega t} dt.$$

This can be interpreted as a generalization of the waveform cross-correlation matrix in (3.3), where $\boldsymbol{s}(t) \in \mathbb{C}^{N_s}$ is the waveform vector, $T_\mathrm{p} \in \mathbb{R}_+$ the pulse length, and $\Delta\tau, \Delta\omega \in \mathbb{R}$ the delay and Doppler differences, respectively. Delay

and Doppler enable discriminating between close/far and stationary/moving scatterers within the same spatial resolution cell. Ambiguities in these two domains are also influenced by the pulse repetition rate, see [248, p. 139]. The ideal ambiguity function is a two-dimensional Dirac delta ("thumbtack") function.

The signal model (3.5) can be easily extended to account for the range-Doppler ambiguity function. For example, the matched filter output of the O-MIMO array ($\boldsymbol{R}_s(0,0) = \boldsymbol{I}$) at delay τ and Doppler frequency ω is [79]

$$\boldsymbol{x}(\tau,\omega) = \sum_{k=1}^{K} \left(\boldsymbol{R}_s(\tau-\tau_k,\omega-\omega_k)\otimes\boldsymbol{I}\right)^{\mathrm{H}} \left(\boldsymbol{a}_{\mathrm{t}}(\boldsymbol{v}_k)\otimes\boldsymbol{a}_{\mathrm{r}}(\boldsymbol{v}_k)\right)\gamma_k + \boldsymbol{n}, \tag{3.20}$$

where $\boldsymbol{n} \sim \mathscr{CN}(\boldsymbol{0},\sigma^2\boldsymbol{I})$ is a circularly symmetric complex Gaussian noise vector, and τ_k,ω_k are the delay and Doppler of the kth scatterer. Eq. (3.20) can be interpreted as a direction-dependent weighted sum of effective steering vectors supported on the sum co-array. Note that sparse array techniques can also be applied to pulse sequence design to, e.g., reduce power consumption [58, 267].

Connection to passive sensing

The passive sensing model in (2.4) can be viewed as a special case of the active sensing model (3.5) with a single transmitter, $N_{\mathrm{t}} = 1$, and a time-varying scattering coefficient (source waveform) vector $\boldsymbol{\gamma}$. Extending (2.4) to planar arrays and possibly non-digital beamforming networks similar to (3.5) is straightforward.

The main conceptual difference between the active and passive model is that the latter does not assume any knowledge of the transmitter. The superimposed signals observed at the receiver may therefore just as well be generated by a collection of uncorrelated emitters, as opposed to some unknown and possibly time-varying scattering coefficients modulating the unknown transmitted waveforms. The passive array model is also relevant for active sensing, since the sensing environment may contain emitters that do not interact with active illumination. A typical example is an active radar in the presence of both targets and interference. As the same array may be used for a variety of tasks, including passive and active sensing or communications, versatile multi-function sparse array configurations are of high practical interest.

Finally, we note that the sum co-array related concepts introduced in Section 3.4, such as the multiplicity function, number of contiguous DoFs, and the co-array steering or selection matrix can equivalently be defined for the difference co-array (e.g., see [165, Appendix B]). The definitions are usually simplified by the fact that the difference co-array is symmetric.

4. Design of sparse arrays with a contiguous sum co-array

As discussed in Section 2.2, sparse array designs can be either adaptive or static, depending on how the array configuration changes in response to the sensing environment. Designs may also be classified based on if the set of feasible sensor positions is continuous or discrete. This chapter takes a non-adaptive approach, where the sensors are confined to a finite number of positions on a uniform grid, per assumption (A3) in Section 3.1. In particular, we consider sparse array configurations of the minimum-redundancy type, which have a contiguous sum co-array covering as large a set of lattice points as possible. The adopted design methodology has two main advantages. Firstly, the array design problem needs to be solved only once, and in an offline fashion. Secondly, the array architecture is simplified, as no switching network is needed. The uniformity of the sum co-array also simplifies computational and theoretical aspects of array processing.

The chapter is organized as follows. Section 4.1 reviews the preliminaries of active array design. Section 4.2 formulates the sum co-array based Minimum-Redundancy Array (MRA) problem and presents some solutions. Section 4.3 introduces scalable parametric configurations, which allow generating low-redundancy arrays of arbitrary size. Section 4.4 concludes the chapter by discussing extensions and alternative array design criteria.

4.1 General design considerations and criteria

We shortly discuss a categorization of active arrays that will provide useful later when considering different solutions to the MRA problem. This categorization is based on the fraction of sensors shared by the transmitting and receiving arrays, with the three main categories being *non-overlapping*, *partially overlapping* and *fully overlapping* Tx and Rx arrays. We then review two figures of merit that play a key role in array design: the redundancy and the d-spacing multiplicity.

4.1.1 Overlap between Tx and Rx arrays

The spatially co-located Tx and Rx arrays may or may not share sensors. As we will see in Section 4.1.2, it is important to take into account the freedom one has in choosing the sensor positions when evaluating the redundancy of the combined Tx-Rx array. The number of distinct sensors (either transmitting, receiving or transceiving), $|\mathscr{D}_\mathrm{t} \cup \mathscr{D}_\mathrm{r}|$, may be less than the total number of transmitters and receivers, $|\mathscr{D}_\mathrm{t}| + |\mathscr{D}_\mathrm{t}|$. In fact, these two quantities and the number of shared sensors (transceivers) satisfy the following relation:

$$|\mathscr{D}_\mathrm{t}| + |\mathscr{D}_\mathrm{r}| = |\mathscr{D}_\mathrm{t} \cup \mathscr{D}_\mathrm{r}| + |\mathscr{D}_\mathrm{t} \cap \mathscr{D}_\mathrm{r}|. \tag{4.1}$$

Depending on the overlap between the Tx and Rx arrays, it is natural to divide active array configurations into the following three categories (see Fig. 4.1):

a) *Non-overlapping* Tx and Rx arrays, $\mathscr{D}_\mathrm{t} \cap \mathscr{D}_\mathrm{r} = \emptyset$.

b) *Partially overlapping* Tx and Rx arrays, $\emptyset \subset \mathscr{D}_\mathrm{t} \cap \mathscr{D}_\mathrm{r} \subset \mathscr{D}_\mathrm{t} \cup \mathscr{D}_\mathrm{r}$

c) *Fully overlapping* Tx and Rx arrays, $\mathscr{D}_\mathrm{t} = \mathscr{D}_\mathrm{r} = \mathscr{D}$.

The number of sensors thus satisfies $|\mathscr{D}_\mathrm{t} \cup \mathscr{D}_\mathrm{r}| \in \{\max(|\mathscr{D}_\mathrm{t}|, |\mathscr{D}_\mathrm{r}|) : |\mathscr{D}_\mathrm{t}| + |\mathscr{D}_\mathrm{r}|\}$, which in the non-overlapping and fully overlapping cases simplifies to

$$|\mathscr{D}_\mathrm{t} \cup \mathscr{D}_\mathrm{r}| = \begin{cases} |\mathscr{D}_\mathrm{t}| + |\mathscr{D}_\mathrm{r}|, & \text{if } \mathscr{D}_\mathrm{t} \cap \mathscr{D}_\mathrm{r} = \emptyset \\ |\mathscr{D}|, & \text{if } \mathscr{D}_\mathrm{t} = \mathscr{D}_\mathrm{r} = \mathscr{D}. \end{cases}$$

Non-overlapping transmitters and receivers are often found in MIMO radar applications, such as automotive radar [204]. The fully overlapping case is common in phased array radar [248, p. 5] and medical ultrasound [179], which also occasionally consider the partially overlapping case [176, 24].

4.1.2 Redundancy

Redundancy quantifies the degree of virtual element repetition in the co-array. Originally defined by Moffet for passive arrays and the difference co-array [187], the definition of redundancy was later extended by Hoctor and Kassam to active arrays and the sum co-array [113]. We exclusively consider the redundancy of the sum co-array in this work. In contrast to [113] that only considered fully overlapping and non-overlapping linear Tx and Rx arrays, we propose the following general definition of redundancy, which is also applicable to partially overlapping and planar arrays:

$$R \triangleq \frac{|\mathscr{D}_\mathrm{t}||\mathscr{D}_\mathrm{r}| - \frac{1}{2}|\mathscr{D}_\mathrm{t} \cap \mathscr{D}_\mathrm{r}|\big(|\mathscr{D}_\mathrm{t} \cap \mathscr{D}_\mathrm{r}| - 1\big)}{H_\Sigma}. \tag{4.2}$$

The numerator in (4.2) is the maximum number of total DoFs, i.e., the maximum number of unique elements in the sum co-array. This expression follows from

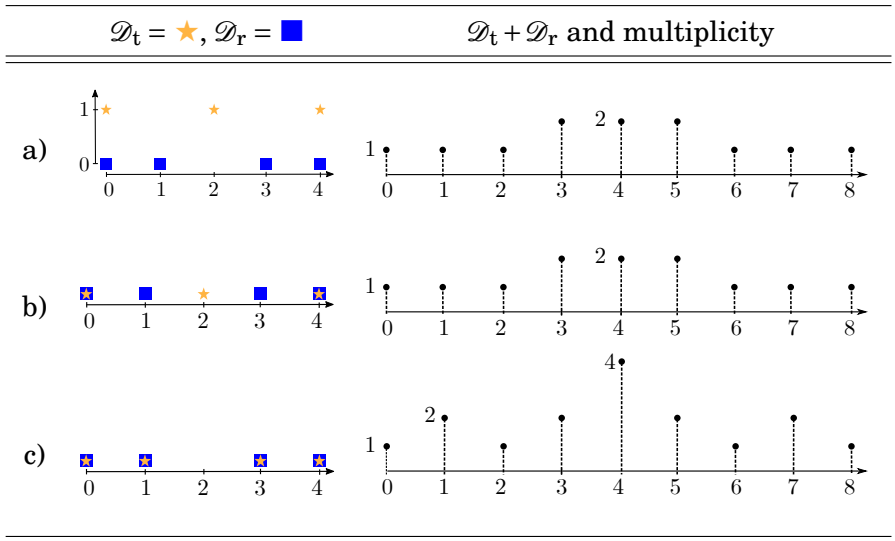

Figure 4.1. Diversely overlapping Tx and Rx arrays with the respective sum co-array: a) non-overlapping, b) partially overlapping, and c) fully overlapping.

decomposing the Tx and Rx arrays, as well as the sum co-array, into subsets of overlapping and non-overlapping elements, as shown in Appendix A.3.

The denominator in (4.2) is the number of contiguous DoFs, defined in (3.14). This is consistent with Moffet's definition of redundancy[1] [187], but differs from Hoctor and Kassam's definition in [113, Eq. (7)]. Their definition replaces H_Σ in (4.2) by the total number of DoFs $|\mathscr{D}_\Sigma|$, which allows any array with strictly unique sum co-array elements to achieve $R = 1$. In contrast, (4.2) requires that the unique sum co-array elements are also contiguous, which is in agreement with the conventional understanding of redundancy in the context of sparse arrays, and particularly, the MRA.

In the extreme cases of fully overlapping non-overlapping Tx and Rx arrays, the redundancy reduces to (cf. [113, Eq. (7) and (8)])

$$R = \begin{cases} |\mathscr{D}_\mathrm{t}||\mathscr{D}_\mathrm{r}|/H_\Sigma, & \text{if } \mathscr{D}_\mathrm{t} \cap \mathscr{D}_\mathrm{r} = \emptyset \\ \frac{1}{2}|\mathscr{D}|(|\mathscr{D}|+1)/H_\Sigma, & \text{if } \mathscr{D}_\mathrm{t} = \mathscr{D}_\mathrm{r} = \mathscr{D}. \end{cases}$$

In either case, a non-redundant array achieves $R = 1$, whereas $R > 1$ holds for a redundant array. This is also true in the partially overlapping case.

Example 4.1 (Redundancy)**.** *Table 4.1 shows the redundancy of the three array configurations in Fig. 4.1. Each array is redundant and $R > 1$. The non-overlapping configuration in a) is the most redundant, since the freedom in placing the sensors independently is inefficiently utilized. The fully overlapping configuration in c) is less redundant than the partially overlapping array in b), despite having one more transmitter.*

[1] Moffet's definition is $R = N(N-1)/(H_\Delta - 1)$, whereas actually $R = (N(N-1)+1)/H_\Delta$ would be entirely consistent with (4.2). Here $H_\Delta \triangleq \max_{h \in \mathbb{N}_+} \left(2h-1 \mid \mathscr{D}_\Delta \supseteq \{0:h-1\}\right)$ is the number of contiguous difference co-array elements.

Table 4.1. Redundancy of array configurations in Fig. 4.1. Configuration c) achieves the lowest redundancy, as it makes the most efficient use of its physical sensors in achieving a contiguous sum co-array for the given overlap between the Tx and Rx arrays.

	$\lvert\mathscr{D}_\mathrm{t}\rvert$	$\lvert\mathscr{D}_\mathrm{r}\rvert$	$\lvert\mathscr{D}_\mathrm{t}\cap\mathscr{D}_\mathrm{r}\rvert$	H_Σ	R
a)	3	4	0	9	$12/9\approx 1.33$
b)	3	4	2	9	$11/9\approx 1.22$
c)	4	4	4	9	$10/9\approx 1.11$

In the case of fully overlapping Tx and Rx arrays, it is often of interest to evaluate the *asymptotic redundancy* for a fixed aspect ratio $\rho = h_y/h_x$,

$$R_\infty \triangleq \lim_{h_x\to\infty} R = \lim_{h_x\to\infty} \frac{|\mathscr{D}|(|\mathscr{D}|+1)}{2\rho h_x^2}. \tag{4.3}$$

By (3.15), the sum co-array is assumed w.l.o.g. to be a wide rectangle ($h_y \le h_x$) with aspect ratio $\rho \in (0,1]$. In case of a linear array, the limit in (4.3) is evaluated for the non-constant aspect ratio $\rho = 1/h_x$.

4.1.3 d-spacing multiplicity

The *d-spacing multiplicity*, $S(d)$, enumerates the number of inter-sensor spacings of a given displacement $d \in \mathbb{N}_+$. For example, in an array where the smallest physical inter-sensor spacing is half a wavelength, $S(2)$ denotes the number of sensor pairs separated by one wavelength. Denoting by $\mathscr{D}_\Delta$ the difference co-array of the union of the Tx and Rx arrays $\mathscr{D}_\mathrm{t}\cup\mathscr{D}_\mathrm{r}$, the multiplicity of displacement $d \ge 1$ is defined as

$$S(d) \triangleq \frac{1}{2}\sum_{\boldsymbol{d}_\Delta\in\mathscr{D}_\Delta} v_\Delta(\boldsymbol{d}_\Delta)\,\mathbb{1}(\|\boldsymbol{d}_\Delta\|_2 = d). \tag{4.4}$$

For linear arrays, d is a positive integer, and $S(d)$ simplifies to the multiplicity function of the positive difference co-array elements. In the planar case, d may also assume non-integer values, i.e., $d = 1, \sqrt{2}, 2, \sqrt{5}, \sqrt{8}, 3$, etc.

Typically, a low value for $S(d)$ is desired for small d, as sensors that are closer interact more strongly with each other [83]. In particular, the severity of mutual coupling effects may controlled by decreasing $S(d)$ [36, 163, 166, 307]. This simplifies array design, but has its limitations. Specifically, the d-spacing multiplicity neglects important factors impacting coupling, such as the element gain patterns, mounting platform, and isolation between, as well as the scan angle and regularity of the Tx and Rx arrays [27, Ch. 8]. Since treating such effects in a mathematically tractable way is challenging (without resorting to numerical methods), proxies like the *number of unit spacings* $S(1)$ are occasionally considered instead to simplify array design

Example 4.2 (d-spacing multiplicity)**.** *Table 4.2 shows the d-spacing multiplicities of the three array configurations in Fig. 4.1. Configuration c) has the fewest*

Table 4.2. d-spacing multiplicity of array configurations in Fig. 4.1.

	$S(1)$	$S(\sqrt{2})$	$S(2)$	$S(\sqrt{5})$	$S(\sqrt{8})$	$S(3)$	$S(\sqrt{10})$	$S(\sqrt{13})$	$S(4)$	$S(\sqrt{17})$
a)	4	4	3	2	0	2	2	0	1	2
b)	4	0	3	0	0	2	0	0	1	0
c)	2	0	1	0	0	2	0	0	1	0

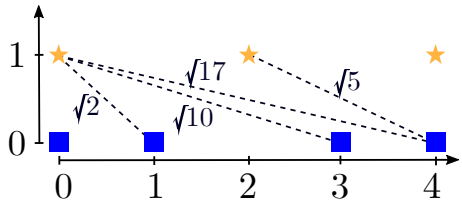

Figure 4.2. Unique diagonal inter-sensor spacings of the planar array in Fig. 4.1 a) with a linear sum co-array and non-overlapping Tx (★) and Rx (■) sensors.

unit spacings, i.e. $S(1) = 2$. *In contrast to the linear arrays in c) and b), the planar array in a) also contains non-integer valued spacings, which correspond to the diagonal distances between sensors (see Fig. 4.2).*

Weighted sum of d-spacing multiplicities

In order to prioritize the d-spacing multiplicity for different values of d, the *weighted sum of d-spacing multiplicities* may be defined as

$$\varsigma \triangleq \sum_{d \leq \|\max(\mathscr{D}_\mathrm{t} \cup \mathscr{D}_\mathrm{r})\|_2} S(d) \cdot 10^{-\sum_{l \leq d} \left(\lfloor \log U(l) \rfloor + 1 \right)}. \tag{4.5}$$

Here, $S(d)$ is the d-spacing multiplicity defined in (4.4), and $U(d)$ is an upper bound on $S(d)$. The weight of each $S(d)$ in (4.5) controls the relative emphasis given to different d-spacing multiplicities. In general, these weights can be any user-defined non-negative numbers. The particular (non-unique) choice in (4.5) ensures that ς is minimized for the array with the *fewest closely spaced sensors* among a set of sum co-array equivalent arrays with an equal number of physical sensors. This suggests a monotonically decreasing weight function that promotes large sensor displacements by prioritizing a low value of $S(d)$ for small d. Specifically, we require that any two arrays, say $\mathscr{D}_a$ and $\mathscr{D}_b$, satisfy $\varsigma_a < \varsigma_b$, if and only if there exists some d such that $S_a(d) < S_b(d)$ and for all $l < d$ it holds that $S_a(l) = S_b(l)$.

A natural choice for the upper bound $U(d)$ is the d-spacing multiplicity of the smallest URA that is larger than or equal to each array being considered. That is, each candidate array configuration and the $N_x \times N_y$ sensor URA satisfy

$$\max(\mathscr{D}_\mathrm{t} \cup \mathscr{D}_\mathrm{r}) - \min(\mathscr{D}_\mathrm{t} \cup \mathscr{D}_\mathrm{r}) \subseteq \{0 : N_x - 1\} \times \{0 : N_y - 1\}.$$

Table 4.3. Weighted sum of d-spacing multiplicities of array configurations in Fig. 4.1.

	$S(1)$	$S(\sqrt{2})$	$S(2)$	ς
a)	4	4	3	0.0443…
b)	4	0	3	0.0403…
c)	2	0	1	0.0201…
URA	13	8	6	0.1386…

Consequently, for a linear array of aperture L, (4.5) reduces to

$$\varsigma = \sum_{d=1}^{L} S(d) \cdot 10^{-\sum_{l=1}^{d} \left(\lfloor \log(L-l+1) \rfloor + 1 \right)}, \tag{4.6}$$

since d only assumes (positive) integer values.

Example 4.3 (Weighted sum of d-spacing multiplicities)**.** *Table 4.3 shows the weighted sum of d-spacing multiplicities for the three MRAs in Fig. 4.1. Since the 4×2 sensor URA covers all three arrays,* (4.5) *evaluates to* $\varsigma = S(1) \cdot 10^{-2} + S(\sqrt{2}) \cdot 10^{-3} + S(2) \cdot 10^{-4} + \ldots$ *Consequently, c) achieves the lowest ς, followed by b) which has the same $S(1)$ as a), but a lower $S(\sqrt{2})$.*

As we will see next, the MRA is not unique in general. Consequently, it can be useful to rank the different solutions according to the weighted sum of d-spacing multiplicities. Effectively, ς can be thought of as a secondary objective function or a regularizing term (satisfying $0 \leq \varsigma < 1$) that is added to the original (integer-valued) objective function to promote large inter-sensor spacings.

4.2 Minimum-Redundancy Array

A large sum co-array is desirable for resolving as many scatterers as possible. Array processing is also efficient and greatly simplified if the sum co-array is contiguous, or if it contains a large contiguous subarray. The *Minimum-Redundancy Array* (MRA) plays a critical role in this regard, since redundancy quantifies how efficiently the sensors of the physical array and co-array are utilized.

Moffet first proposed the MRA in the context of passive linear arrays and the difference co-array [187]. He distinguished between the *general* and *restricted* solutions, where the latter constrains the difference co-array to be contiguous. The restricted MRA thus yields the maximum number of contiguous co-array elements for a given physical aperture (cf. Section 3.4.2). Note that a general MRA can, but need not be restricted. Hoctor and Kassam later extended the MRA to active sensing [113]. They specifically considered the restricted linear MRA with a contiguous sum co-array. Linear difference and sum MRAs correspond to extremal difference bases [228, 150, 294] and extremal additive bases [232, 49,

230, 132], respectively. Additive bases have been studied in number theory since the early 1900s and are informally known as solutions to the *postage stamp problem* [177, 191]. The canonical postage stamp problem seeks a set of stamps that can represent each non-negative integer fare smaller than some $h \in \mathbb{N}$ using the sum of at most k stamps. The restricted postage stamp basis with maximal h for $k = 2$, or extremal restricted 2-basis, coincides with the linear sum MRA.

In contrast, fewer works have considered the planar MRA or the corresponding planar basis in detail [212]. Particularly planar *sum* MRAs have received scant attention. Such planar arrays are important in many active sensing tasks, including radar, imaging, and direction finding. Even the linear sum MRA lacks a clear definition in the case of partially overlapping Tx and Rx arrays.

Section 4.2.1 proposes a definition of the restricted sum MRA, which not only applies to planar arrays, but also to the three cases of Tx and Rx array overlap listed in Section 4.1.1. This is an extension of the definition the linear fully overlapping (restricted) MRA proposed in Publication IX, which in turn is based on the definitions in [187, 113]. Sections 4.2.2 and 4.2.3 briefly consider the design of non-overlapping, respectively, partially overlapping Tx and Rx arrays. Section 4.2.4 discusses in detail the fully overlapping case, which is the focus of the chapter.

4.2.1 Definition of MRA

Directly minimizing the expression for redundancy in (4.2) yields the most general definition of the planar sum MRA. However, the resulting optimization problem is of limited value unless physically meaningful constraints are included. A more practical formulation is obtained by constraining the number of physical sensors or the virtual array aperture. We propose the following two definitions of the (restricted) MRA—corresponding to minimizing (4.2) subject to a fixed denominator and numerator, respectively:

1. **MRA with constrained number of sensors.** If the number of transmitters and receivers is fixed, in addition to the number of transceivers, then the MRA is any solution to

$$\begin{aligned} \underset{\mathscr{D}_\xi \subseteq \mathbb{N}^2;\, h_x, h_y \in \mathbb{N}}{\text{maximize}} \quad & h_x h_y \\ \text{subject to} \quad & \mathscr{D}_\mathrm{t} + \mathscr{D}_\mathrm{r} = \{0 : h_x - 1\} \times \{0 : h_y - 1\} \\ & |\mathscr{D}_\mathrm{t}| = N_\mathrm{t},\ |\mathscr{D}_\mathrm{r}| = N_\mathrm{r},\ \text{and } |\mathscr{D}_\mathrm{t} \cap \mathscr{D}_\mathrm{r}| = N. \end{aligned} \tag{P4.1}$$

   Problem (P4.1) can have both linear and planar solutions, since the aspect ratio in (3.15) is not constrained. In practice, the aspect ratio is determined by the relative importance of the azimuth and elevation domains.

2. **MRA with constrained co-array aperture.** If the size of the sum co-array is constrained, in addition to the fraction of all Tx or Rx sensors that

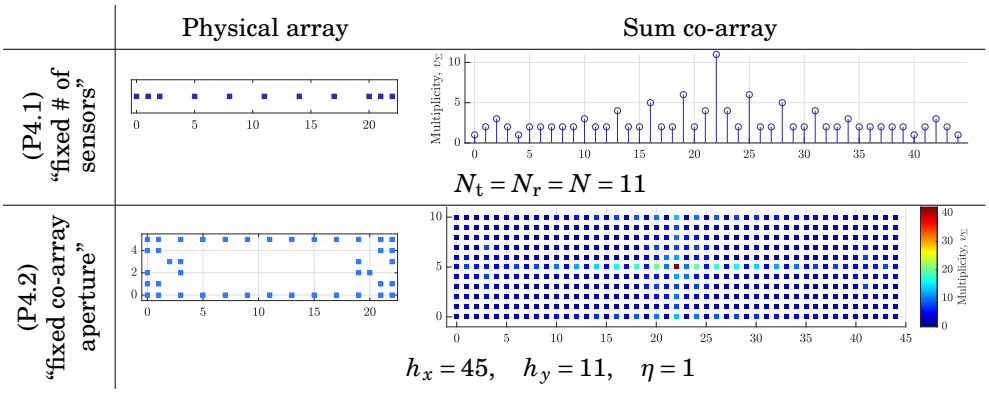

Figure 4.3. MRAs for a fixed number of sensors (top) and a fixed size co-array (bottom). Both solutions assume fully overlapping Tx and Rx arrays.

are transceivers, then the MRA is any solution to

$$\begin{aligned} &\underset{\mathscr{D}_\xi \subseteq \mathbb{N}^2}{\text{minimize}} \ |\mathscr{D}_\mathrm{t}||\mathscr{D}_\mathrm{r}| - \frac{1}{2}|\mathscr{D}_\mathrm{t} \cap \mathscr{D}_\mathrm{r}|\big(|\mathscr{D}_\mathrm{t} \cap \mathscr{D}_\mathrm{r}| - 1\big) \\ &\text{subject to } \mathscr{D}_\mathrm{t} + \mathscr{D}_\mathrm{r} = \{0 : h_x - 1\} \times \{0 : h_y - 1\} \\ &\qquad |\mathscr{D}_\mathrm{t} \cap \mathscr{D}_\mathrm{r}| / |\mathscr{D}_\mathrm{t} \cup \mathscr{D}_\mathrm{r}| = \eta. \end{aligned} \tag{P4.2}$$

Scalar $\eta \in [0, 1]$ controls the degree of overlap between the Tx and Rx arrays, without fixing the number of sensors. Specifically, $\eta = 1$ and $\eta = 0$ correspond to the fully overlapping and non-overlapping cases, respectively. In the partially overlapping case, it may be more convenient to constrain the degree of overlap to an interval of values rather than exactly η.

The "fixed number of sensors" formulation in (P4.1) coincides with the conventional definition of the sum MRA in the restricted linear case, when the Tx and Rx arrays are fully overlapping [113]. The difference MRA is also originally defined for a constrained number of sensors [187]. The linear difference MRA with a constrained aperture [31, 242] is called a *sparse ruler* [244, 233].

The "fixed co-array aperture" formulation in (P4.2) is convenient when only a limited area for placing the sensors is available, or when the desired co-array is strictly planar and nonsquare. Fig. 4.3 illustrates a solution to (P4.1) and (P4.2) in the case of fully overlapping Tx and Rx arrays. Note that we can assume w.l.o.g. that $\min\big(\mathscr{D}_\mathrm{t} + \mathscr{D}_\mathrm{r}\big) = \mathbf{0}$ to exclude trivial offsets of the sum co-array. Nonetheless, (P4.1) and (P4.2) remain combinatorial problems that are usually difficult to solve efficiently for a large number of sensors or co-array aperture.

4.2.2 Non-overlapping Tx and Rx arrays

In the non-overlapping case, or in the case of a single overlapping sensor, (P4.1) and (P4.2) have a simple closed-form solution that achieves $R = 1$. This solution has a nested structure consisting of a dense and a sparse *Uniform Rectangular*

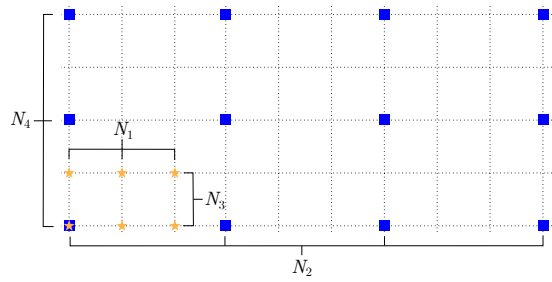

Figure 4.4. MRA in Proposition 4.1. The Tx and Rx arrays (which are interchangeable) are either non-overlapping or have a single common sensor (offset $\boldsymbol{l} = \mathbf{0}$ depicted).

Array (URA). Fig. 4.4 illustrates this nested configuration, where the Tx and Rx arrays are (the definitions may naturally be reversed)

$$\begin{aligned} \mathscr{D}_\mathrm{t} &= \{0 : N_1 - 1\} \times \{0 : N_3 - 1\} + \boldsymbol{l}, \\ \mathscr{D}_\mathrm{r} &= \{0 : N_1 : N_1(N_2 - 1)\} \times \{0 : N_3 : N_3(N_4 - 1)\} - \boldsymbol{l}. \end{aligned} \tag{4.7}$$

Here $\{N_i\}_{i=1}^4 \in \mathbb{N}$ are the array parameters and $\boldsymbol{l} \in \mathbb{Z}^2$ is an offset vector. The following proposition lists the conditions under which (4.7) is an MRA.

Proposition 4.1 (Non-overlapping MRA)**.** *The nested structure in* (4.7) *is a solution to* (P4.1) *if and only if* $N_1N_3 = N_\mathrm{t}$*;* $N_2N_4 = N_\mathrm{r}$*; and* $N \leq 1$*, correspondingly,* (P4.2) *if and only if* $N_1N_2 = h_x$*;* $N_3N_4 = h_y$*; and* $(N_1N_3 + N_2N_4)\eta = 0$ *or* $(1 + \eta)$*.*

Proof. This follows directly from the unit (i.e., minimum) redundancy property of (4.7). Namely, $R = |\mathscr{D}_\mathrm{t}||\mathscr{D}_\mathrm{r}|/|\mathscr{D}_\mathrm{t} + \mathscr{D}_\mathrm{r}| = 1$, since by definition $|\mathscr{D}_\mathrm{t} \cap \mathscr{D}_\mathrm{r}| \leq 1$; $|\mathscr{D}_\mathrm{t}| = N_1N_3$; $|\mathscr{D}_\mathrm{r}| = N_2N_4$; and $\mathscr{D}_\mathrm{t} + \mathscr{D}_\mathrm{r} = \{0 : N_1N_2 - 1\} \times \{0 : N_3N_4 - 1\}$. □

Proposition 4.1 implies that the MRA solving (P4.1) can have several shapes with sum co-arrays of different aspect ratios, as shown in Fig. 4.5. Two of the three solutions in Fig. 4.5 yield linear Tx and Rx arrays. One consists of perpendicular ULAs following from setting $N_1 = N_4 = 1$ or $N_2 = N_3 = 1$. The other, with $N_1 = N_2 = 1$ or $N_3 = N_4 = 1$, has a linear nested structure consisting of a dense and a sparse ULA placed in parallel. Two additional solutions, with the same sum co-arrays as solutions #1 and #3 in Fig. 4.5, follow from swapping the definitions of the Tx and Rx array in (4.7) and setting $N_3 = N_4 = 1$ or $N_1 = N_2 = 1$, and $N_1 = 2$; $N_2 = 3$ or $N_4 = 3$, respectively. Other non-overlapping MRAs may exist too, as the solutions to (P4.1) and (P4.2) need not follow (4.7).

Previous works have also studied the nested configuration (4.7) in the one-dimensional (linear array) case [174, 56]. However, the minimum-redundancy property of (4.7), especially in the two-dimensional (planar array) case, has not been established or explicitly stated before to the best of our knowledge. We note that (4.7) is similar to the passive Nested Array [200, 201, 202], as both leverage arithmetic sequences to ensure a contiguous sum or difference co-array, respectively.

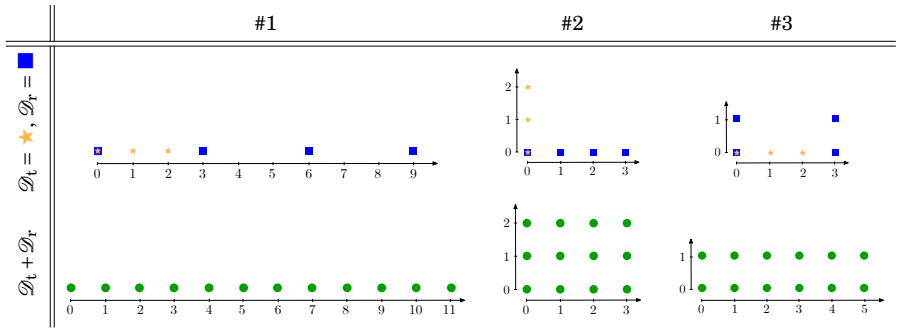

Figure 4.5. Three MRAs with $|\mathscr{D}_t| = 3$ transmitters, $|\mathscr{D}_r| = 4$ receivers, $|\mathscr{D}_t \cap \mathscr{D}_r| = 1$ transceiver, and $H_\Sigma = 12$ contiguous sum co-array elements. Shifting the Tx or Rx array yields a non-overlapping MRA. Each configuration is a solution to (P4.1) by Proposition 4.1.

4.2.3 Partially overlapping Tx and Rx arrays

As previously shown, the MRA with a single overlapping Tx and Rx sensor is practically equivalent to the MRA with no overlap. In contrast, the MRA with an overlap of $|\mathscr{D}_t \cap \mathscr{D}_r| \in \{2 : |\mathscr{D}_t \cup \mathscr{D}_r| - 1\}$ sensors is an open problem. However, we do not pursue this problem further, since the non-overlapping and fully overlapping cases seem to be of greater practical interest in applications. We focus our attention on the fully overlapping MRA, which turns out to be a considerably more challenging problem than the MRA with a single overlapping Tx/Rx sensor.

4.2.4 Fully overlapping Tx and Rx arrays

In the case of fully overlapping Tx and Rx arrays (each sensor is a transceiver) the "fixed co-array size" formulation of the MRA in (P4.2) reduces to

$$\underset{\mathscr{D}\subseteq\mathbb{N}^2}{\text{minimize}}\ |\mathscr{D}| \quad \text{subject to} \quad \mathscr{D}+\mathscr{D} = \{0 : h_x - 1\} \times \{0 : h_y - 1\}. \tag{P4.3}$$

This is a natural definition of the MRA in the strictly planar array case, whereas the "fixed number of sensors" formulation in (P4.1) is more appropriate in the linear array case (with the additional constraint that $h_y = 1$). The rest of this chapter focuses on (P4.3), as we mainly consider planar arrays henceforth.

W.l.o.g., the sensors are constrained to the non-negative orthant, with the first sensor placed at the origin. In fact, any array $\mathscr{D}$ with a contiguous sum co-array satisfies

$$\mathscr{D} \subseteq \{0 : L_x\} \times \{0 : L_y\},$$

where $L_x = (h_x - 1)/2$ and $L_y = (h_y - 1)/2$ are the side lengths of the physical array. This implies that h_x and h_y are odd. Hence, L_x and L_y provide a more convenient parametrization of an array with shared Tx and Rx sensors and a contiguous sum co-array.

Global search algorithm

The number of possible solutions to (P4.3) grows exponentially in L_x and L_y. Specifically, proving that a given array of N sensors is a solution to (P4.3) requires showing that none of the $\binom{(L_x+1)(L_y+1)}{N-1}$ possibilities with $N-1$ sensors are feasible solutions. For example, if $N = 36$ and $L_x = L_y = 9$, then the number of possible 35 sensor solutions is $\binom{100}{35} \propto 10^{27}$. Although the number of cases can be reduced to $\binom{91}{35} \propto 10^{25}$ by deducing the necessity of certain corner sensors (cf. Publication V, Property 1), exhaustively checking these by brute force remains impractical. However, a sensible search strategy can yield an answer even in this seemingly hopeless case.

Publication V proposes a global search algorithm for solving (P4.3) based on concatenating smaller subarrays found by a *branch-and-bound* algorithm into a larger array with a contiguous sum co-array. Using this so-called *meet-in-the-middle* algorithm, we have found all MRAs for $1 \leq L_y \leq L_x \leq 13$. In the following, we briefly summarize the key ideas of both the branch-and-bound and the meet-in-the-middle algorithms, with an emphasis on the latter. The interested reader is referred to Algorithms 1 and 2 of Publication V for details.

1. **Branch-and-bound algorithm.** The branch-and-bound algorithm proposed in Publication V is a two-dimensional extension of *Challis* algorithm [49]. The basic idea of a branch-and-bound search is to traverse a (binary) search tree of possible solutions, and prune branches containing infeasible solutions along the way [147]. Feasibility may be inferred from a problem specific fitness function or condition, which may show that a specific branch of the search tree cannot contain a feasible solution because a better solution or branch is already known. Ideally, this pruning occurs at an early stage of the search, such that a substantial fraction of the potential solutions can be discarded. Consequently, pruning is the key ingredient of any effective branch-and-bound algorithm. In principle, the branch-and-bound algorithm could directly solve (P4.3) to find the MRA. However, we consider a more computationally efficient approach, where the branch-and-bound method serves as an intermediate step of the main (meet-in-the-middle) algorithm described later.

   In particular, the branch-and-bound algorithm is used to find all arrays $\mathscr{D}$ satisfying $\mathscr{D} + \mathscr{D} \subseteq \{0 : h_x - 1\} \times \{0 : h_y - 1\}$ for given h_x, h_y, and $|\mathscr{D}| = N$. We note that any physical sensor outside the desired contiguous part of the sum co-array is wasted, which implies that

   $$\mathscr{D} \subseteq \{0 : h_x - 1\} \times \{0 : h_y - 1\}.$$

   Consequently, each point on the h_x by h_y grid of potential sensor positions can be represented by a binary variable denoting the presence or absence of a sensor. Starting with a total budget of sensors N, we traverse the grid of potential sensor positions row-by-row, considering two simple pruning tests at each position:

- Sum test: Since the algorithm proceeds row-wise (starting from the origin), any sensor added deeper in the search tree cannot contribute to the currently considered point in the sum co-array. Hence, if this point is not covered by the sum of two previously added sensors, then it must contain a sensor.
- Gaps test: Assume that after placing $n \leq N$ sensors, G holes remain in the sum co-array. A simple counting argument shows that the remaining $N-n$ sensors can generate at most $(n+1)+(n+2)+\ldots N = (N+n+1)(N-n)/2$ additional sums. Consequently, if $G > (N+n+1)(N-n)/2$, then the current branch must be pruned.

The solutions found by this algorithm can then be efficiently pieced together to form the MRA, as described next.

2. **Meet-in-the-middle algorithm.** The meet-in-the-middle algorithm proposed in Publication V is a two-dimensional extension of an algorithm by Kohonen [132], who originally used the approach to find the largest (restricted) linear MRA known to date[2] [133]. The algorithm leverages the fact that an MRAs can be constructed by concatenating smaller subarrays found by the branch-and-bound method. Instead of searching for the whole array at once, it is significantly cheaper to first find all subarrays whose concatenation could produce an array with a contiguous sum co-array for the given number of sensors, and then determine by trial-and-error which concatenations actually do. The computational advantage follows from the fact that finding smaller solutions is exponentially faster than finding larger ones due to the combinatorial nature of the problem. Additional speed-up is gained from judiciously selecting the subarrays to concatenate first, as several infeasible concatenations can be eliminated at an early stage. This radically reduces the number of subarray pairings that need to be checked. By carefully constraining the number of sensors and the sum co-array of each subarray, the algorithm is guaranteed to find all MRAs for a given L_x, L_y pair.

   Fig. 4.6 illustrates the partitioning of the candidate MRA, which plays a key role in the proposed two-dimensional meet-in-the-middle method. The algorithm starts by decomposing the array $\mathscr{D}$ into four disjoint subarrays $\{\mathscr{D}_i\}_{i=1}^4$, such that $\mathscr{D} = \bigcup_{i=1}^4 \mathscr{D}_i$ and $\mathscr{D}_i \cap \mathscr{D}_j = \emptyset \ \forall \ i \neq j$. The sum co-array of $\mathscr{D}$ can thus be written as the union of the self, neighboring, and diagonal pairs of sums:

$$\mathscr{D}+\mathscr{D} = \underbrace{\left(\bigcup_{i=1}^{4} \mathscr{D}_i + \mathscr{D}_i\right)}_{\text{self sums}} \cup \underbrace{\left(\bigcup_{i=1}^{4} \mathscr{D}_i + \mathscr{D}_{1+(i \bmod 4)}\right)}_{\text{neighboring sums}} \cup \underbrace{\left(\bigcup_{i=1}^{2} \mathscr{D}_i + \mathscr{D}_{i+2}\right)}_{\text{diagonal sums}}.$$

[2] Corresponding to $|\mathscr{D}| = 48$ physical sensors and $|\mathscr{D}_\Sigma| = 734$ sum co-array elements.

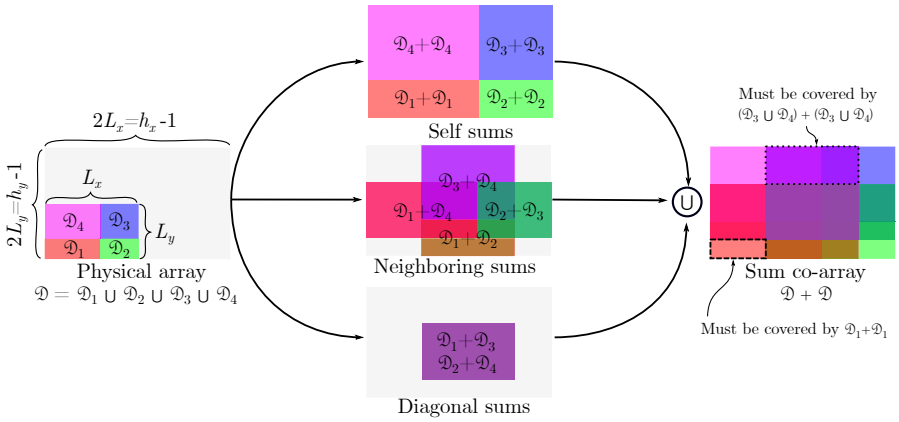

Figure 4.6. Decomposition of planar array leveraged by meet-in-the-middle algorithm. The physical array is partitioned into four disjoint subarrays contained in the colored rectangles (left). The union of the self, neighboring, and diagonal sums of the subarrays (center) constitute the sum co-array (right). For the sum co-array to be contiguous, its boundary must be covered by the self sums of the appropriate subarrays. Adapted from Publication V, Fig. 2.

Each of the four corners of the sum co-array contain patches that must be covered by the self sums alone. It is easy to verify that these patches correspond exactly to the areas containing each subarray $\mathscr{D}_i$ in the assumed partitioning of $\mathscr{D}$. Hence, after appropriate rotations and translations, the subarrays necessarily have a sum co-array covering the respective patches in the partitioning. This, combined with the fact that the number of sensors of $\mathscr{D}$ must satisfy $|\mathscr{D}| = \sum_{i=1}^{4} |\mathscr{D}_i|$, considerably reduces the number of candidate subarrays. Consequently, for a certain partitioning of $\mathscr{D}$ and a given number of sensors, the subarrays $\{\mathscr{D}_i\}_{i=1}^{4}$ can be found by the branch-and-bound algorithm. After this, pairs of neighboring subarray candidates are concatenated and the feasibility of the result is verified. If the sum co-array of the concatenation contains gaps in a region which must be covered by self and cross sums of sensors in those two sets (see Fig. 4.6), then the pair is discarded. Otherwise the pair is retained, and eventually concatenated with another feasible pair to form a candidate for $\mathscr{D}$. If the sum co-array of $\mathscr{D}$ is contiguous, then it is a candidate for an MRA with N sensors. The array is an MRA if the algorithm failed to find a feasible solution for $N-1$ sensors.

Solutions

Publication V, Table 4 summarizes[3] the properties of the MRAs for $1 \le L_y \le L_x \le 13$ found using the meet-in-the-middle algorithm. The number of solutions, after taking into account mirror symmetries, grows rapidly with the number of sensors. For example, the MRA has $N = 52$ sensors and 159744 solutions when $L_x = L_y = 13$. We have also found that the number of sensors in all square MRAs

[3] In the notation of Publication V: $s = 2L = h - 1$, and $k = k^\star = N$.

with side length L is $N = 4L$, when $1 \le L \le 23$. For instance, $N = 92$ when $L = 23$. Fig. 4.7 shows all of the 28 MRAs for $L = 7$ in increasing order of the weighted sum of d-spacing multiplicities ς in (4.5). See also Publication V, Fig. 4 for the MRAs with minimal ς when $1 \le L_y \le L_x = 7$.

4.3 Scalable sparse configurations in fully overlapping case

The main drawback of finding the MRA is that it generally requires solving a combinatorial optimization problem. Consequently, generating MRAs with a large aperture or number of sensors is usually impractical. In contrast, if a sparse array configuration allows a simple parametric description, then arrays of any size can be easily synthesized. For example, some MRAs have a highly regular structure and are thus easily parameterized. This enables generating scalable low-redundancy arrays of practically any size and aspect ratio.

This section discusses parametric sparse array configurations that achieve a low redundancy. We focus on fully overlapping Tx and Rx arrays with an emphasis on restricted configurations. In particular, Section 4.3.1 describes a planar array proposed in Publication IV that is observed to be the MRA with the fewest closely spaced sensors in some cases. Closely spaced sensors can interact strongly and lead to undesired mutual coupling. Section 4.3.2 considers alternative configurations, originally mainly presented in Publication V, that are less sensitive to changes in the array aspect ratio. Finally, Section 4.3.3 discusses a general framework for symmetric linear arrays with a contiguous sum co-array developed in Publication IX.

4.3.1 Square arrays inspired by the MRA

Some MRAs admit a particularly simple parametrization. For example, solution #28 in Fig. 4.7 is known as the *Boundary Array* (BA) [139]. The BA with side lengths L_x and L_y is defined as (see Fig. 4.8 for an illustration)

$$\mathscr{D}_{\mathrm{BA}} \triangleq \big(\{0:L_x\} \times \{0, L_y\}\big) \cup \big(\{0, L_x\} \times \{0:L_y\}\big).$$

The number of physical sensors of the BA is $|\mathscr{D}_{\mathrm{BA}}| = 2(L_x + L_y)$. Although the BA is an not an MRA for any L_x, L_y, less redundant configurations do not always exist when $L_x = L_y = L$. In particular, Publication V, Table 3 reveals that the BA is an MRA for all $L \le 23$. It remains an open question whether the square BA is an MRA also for $L > 23$.

Publication IV shows that the restricted MRA with the fewest closely spaced sensors also follows a remarkably simple pattern for certain L. This so-called *Concentric Rectangular Array* (CRA), depicted in Fig. 4.8, minimizes the weighted sum of d-spacing multiplicities ς in (4.5) among all known square restricted MRAs with even side length $6 \le L \le 12$. For comparison, the BA is typically the MRA with maximal ς. A key property of the CRA is that it has a constant

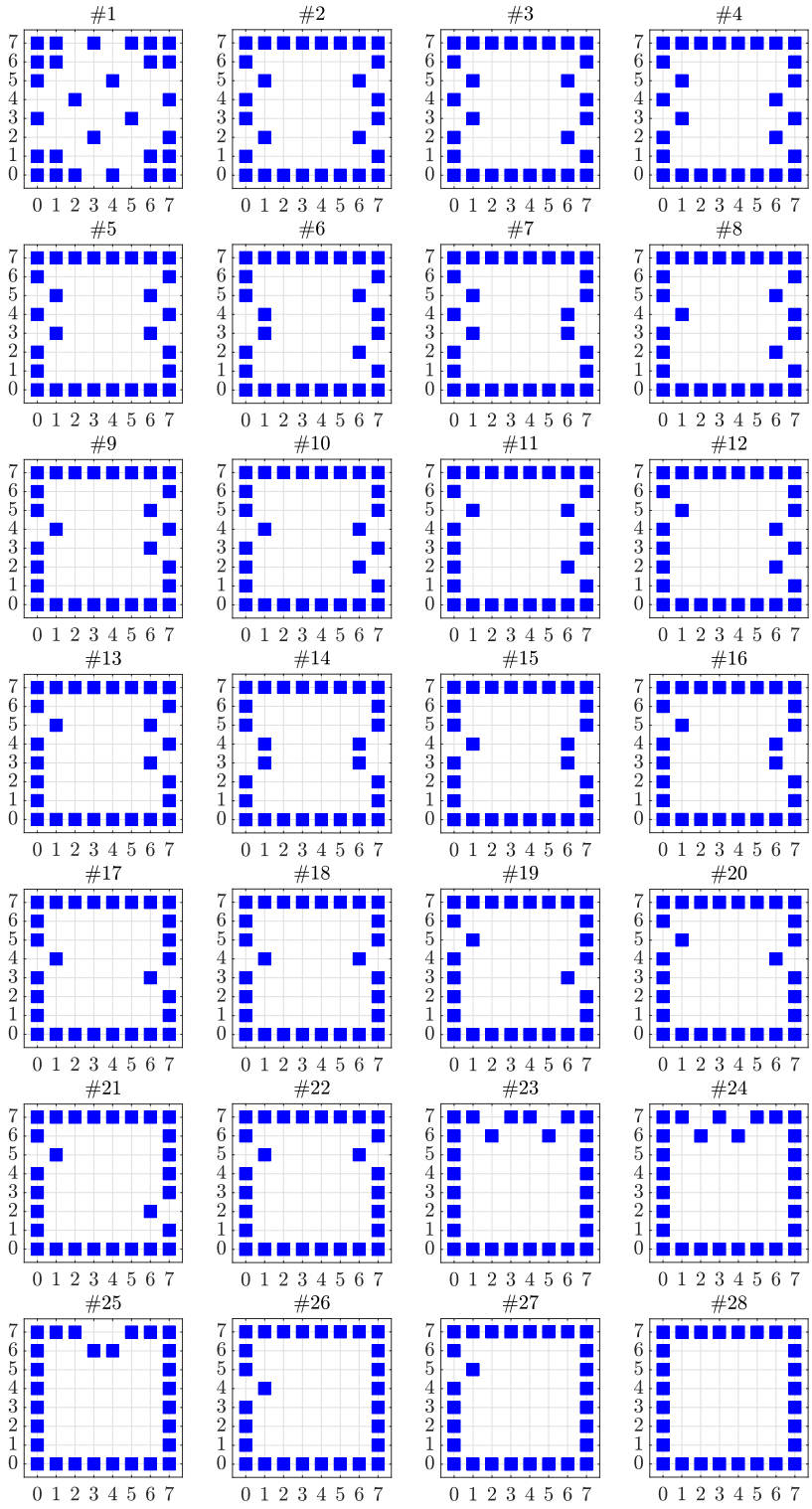

Figure 4.7. Square MRAs with 15×15 element sum co-array. The solutions are in increasing order of the number of closely spaced sensors, i.e., ς in (4.5).

number of unit spacings $S(1)$. In fact, $S(1) = 16$ regardless of aperture, when $L_x, L_y \geq 4$ and even. This is unlike the BA, where $S(1)$ scales linearly with the array dimensions as $S(1) = 2(L_x + L_y)$. Similarly to the BA, the sum co-array of the CRA is contiguous for any feasible choice of parameters L_x and L_y (Publication VIII, Theorem 1). The difference co-array of both arrays is also contiguous, since the physical arrays have mirror symmetry.

A drawback of the CRA and BA is that they become increasingly redundant for non-square arrays, i.e., aspect ratios not equal to unity. In particular, by substituting the number of sensors $N = h_x + h_y - 2$ and aspect ratio $\rho = h_y/h_x$ into (4.3), the asymptotic redundancy evaluates to

$$R_\infty = \lim_{h_x \to \infty} \frac{(h_x(1+\rho)-2)(h_x(1+\rho)-1)}{2\rho h_x^2} = \frac{(1+\rho)^2}{2\rho}.$$

Hence, R_∞ grows without bound with decreasing ρ and reaches its minimum $R_\infty = 2$ at $\rho = 1$. That is, the closer the configurations are to a linear (rather than square) array, the more redundant the sum co-array tends to be.

4.3.2 Rectangular arrays insensitive to aspect ratio

Publication V proposes a novel parametric array configuration called the *Short-Bars Array* (SBA) achieving asymptotic redundancy $R_\infty = 2$ for practically any[4] aspect ratio ρ. The sensor positions of SBA are given by

$$\mathscr{D}_{\text{SBA}} \triangleq \big(\{0 : N_1 - 1\} \times \{0 : N_3 : N_3(N_4 - 1)\}\big) \cup \big(\{0 : N_1 : N_1(N_2 - 1)\} \times \{0 : N_3 - 1\}\big),$$

where array parameters $\{N_i\}_{i=1}^4 \subset \mathbb{N}_+$ satisfy $N_1 N_2 = h_x$ and $N_3 N_4 = h_y$, such that the sum co-array contains a contiguous $h_x \times h_y$ subarray, as shown in Fig. 4.9. The number of sensors of the SBA is $N = N_1 N_4 + N_2 N_3 - 1$. If h_x and h_y are perfect squares, then N is minimized for $N_1 = N_2 = \sqrt{h_x}$ and $N_3 = N_4 = \sqrt{h_y}$. In this case, the SBA has $N = 2\sqrt{h_x}\sqrt{h_y} - 1 = 2\sqrt{\rho} h_x - 1$ sensors and the asymptotic redundancy in (4.3) evaluates to

$$R_\infty = \lim_{h_x \to \infty} \frac{(2h_x\sqrt{\rho} - 1)2h_x\sqrt{\rho}}{2\rho h_x^2} = 2.$$

We may also construct a restricted array achieving $R_\infty = 2$ for practically any aspect ratio. Specifically, the *Restricted Short Bars Array* (R-SBA) is formed by concatenating rotated and shifted copies of the SBA as follows:

$$\begin{aligned}\mathscr{D}_{\text{R-SBA}} \triangleq \mathscr{D}_{\text{SBA}} \cup \big(\max \mathscr{D}_{\text{SBA}} - \mathscr{D}_{\text{SBA}}\big) \cup \big\{L_x \boldsymbol{e}_1 + (\boldsymbol{e}_2 - \boldsymbol{e}_1) \circ \boldsymbol{d} \mid \boldsymbol{d} \in \mathscr{D}_{\text{SBA}}\big\} \\ \cup \big\{L_y \boldsymbol{e}_2 + (\boldsymbol{e}_1 - \boldsymbol{e}_2) \circ \boldsymbol{d} \mid \boldsymbol{d} \in \mathscr{D}_{\text{SBA}}\big\}.\end{aligned} \tag{4.8}$$

Here, $\circ$ is the Hadamard (elementwise) product and $\boldsymbol{e}_i \in \{0,1\}^2$ the standard unit vector. The number of sensors in the R-SBA is $N = 2(N_1 N_4 + N_2 N_3 - 2)$, assuming

[4] More precisely: there exist valid array parameters yielding $R_\infty = 2$ and approximating any $\rho \in (0, 1]$ to an arbitrary precision.

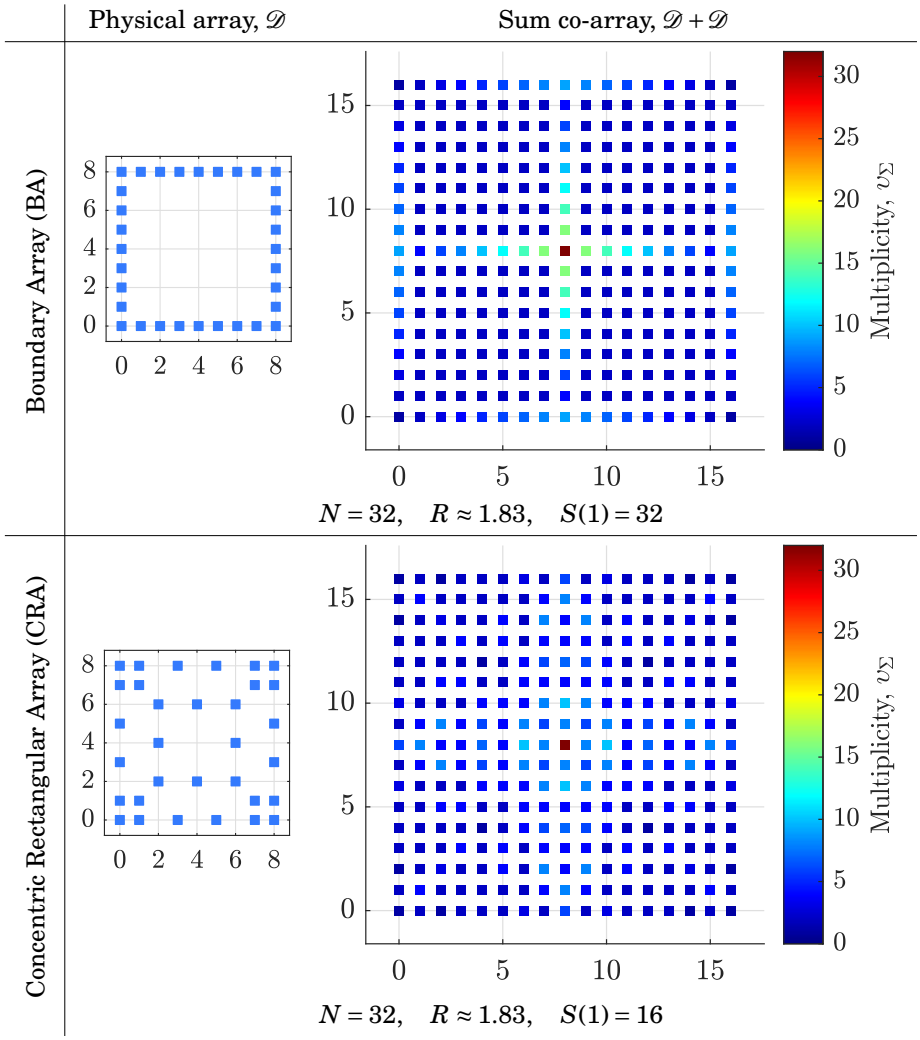

Figure 4.8. Square arrays ($\rho = 1$) with closed-form sensor positions. The BA is an MRA for at least side lengths $L \in \{0:23\}$. The CRA is an MRA for (at least) $L \in \{6:2:22\}$ and the MRA with the fewest closely spaced sensors for $L \in \{6:2:12\}$.

$N_2, N_4 \geq 3$. The array side lengths satisfy $L_x = N_1(N_2 - 1)$ and $L_y = N_3(N_4 - 1)$. If L_x and L_y are perfect squares, then the choice $N_1 = \sqrt{L_x}$ and $N_3 = \sqrt{L_y}$ yields an asymptotic redundancy independent of ρ:

$$R_\infty = \lim_{h_x \to \infty} \frac{2(h_x - 1)(\rho h_x - 1)}{2h_x^2 \rho} = 2.$$

For arbitrary L_x and L_y, the minimum-redundancy parameters $\{N_i\}_{i=1}^4$ can be found numerically, e.g., using a grid search similar to Publication IX, Algorithm 1. Fig. 4.9 illustrates the R-SBA with $L_x = 12$ and $L_y = 4$, corresponding to a 25×9 element contiguous sum co-array with aspect ratio $\rho = 9/25 = 0.36$. The R-SBA has $N = 30$ physical sensors, which is less than the co-array equivalent BA with $N = 32$ sensors, albeit more than the MRA with $N = 28$. The SBA of equivalent physical aperture shown in Fig. 4.9 has a smaller co-array (15×6 contiguous elements), whereas the co-array equivalent SBA has a larger physical aperture (67% larger L_x and 50% larger L_y). The R-SBA and other configurations with a contiguous sum co-array are therefore of primary interest when the physical dimensions of the array are tightly constrained.

If the sum co-array is not required to be contiguous, then less redundant configurations can be constructed. For example, Publication V, Corollary 19 presents a two-dimensional extension of an additive basis by Mrose [194] achieving $R_\infty = 1.75$ for any fixed h_y. Publication V, Corollary 15 also shows that the two-dimensional Nested Array [201, 202] (on a rectangular lattice) achieves $R_\infty = 2$ for practically any ρ.

Fig. 4.10 summarizes our findings regarding planar arrays with a contiguous sum co-array by showing the asymptotic redundancy of the R-SBA, CRA, and BA, along with the (non-asymptotic) redundancy of the MRA with side length $L_y \leq L_x \leq 13$ (see Publication V). The redundancy of the MRA approaches $R \approx 2$ as the aperture grows, providing empirical evidence that the R-SBA, CRA, and BA are close to minimally redundant. The redundancy of the MRA also decreases with the aspect ratio, suggesting that $R_\infty < 2$ may be possible. Indeed, $1.19 < R_\infty < 1.92$ holds for the linear MRA (see Publication IX, Theorem 1), corresponding to aspect ratio $\rho = 0$ as $L_x \to \infty$.

4.3.3 Linear arrays with mirror symmetry

Publication IX proposes a general framework for constructing symmetric linear array configurations with low redundancy. This framework is motivated by the fact that any mirror symmetric[5] array has an identical sum and difference co-array up to a shift[6] [111, p. 740]. Specifically, if $\mathscr{D} = \max\mathscr{D} - \mathscr{D}$, then $\mathscr{D} + \mathscr{D} = \mathscr{D} - \mathscr{D} + \max\mathscr{D}$. By virtue of symmetry, arrays with a contiguous sum co-array can thus be synthesized using configurations with a contiguous difference co-array, such as the ones presented in Section 2.2.2. This greatly simplifies the design of array configurations suitable for not only active, but also passive sensing.

[5] That is, a 180° rotational symmetry along the center point $(\max\mathscr{D} + \min\mathscr{D})/2$.

[6] This also holds for the multiplicity functions of the co-arrays by PIV, Lemma 1.

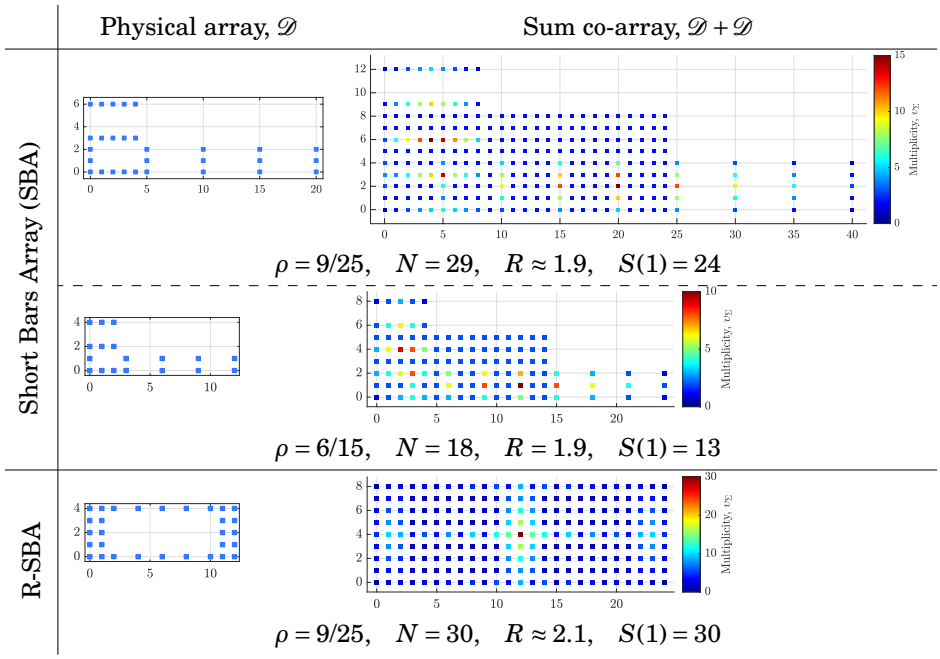

Figure 4.9. Aspect ratio insensitive rectangular arrays ($\rho \approx 0.4$) with closed-form sensor positions. Both the SBA and R-SBA achieve asymptotic redundancy $R_\infty = 2$ irrespective of ρ, unlike the BA and CRA. The SBA requires a larger physical aperture than the R-SBA to achieve a comparable (hole-free) sum co-array.

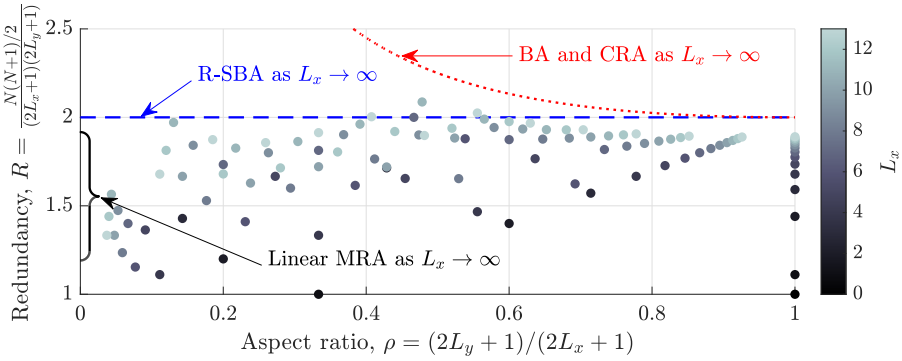

Figure 4.10. Redundancy of MRA for different aspect ratios ρ. The scalable planar array configurations presented in Sections 4.3.1 and 4.3.2 provide upper bounds on the asymptotic redundancy R_∞ of the MRA.

General structure of symmetric linear array

In general, a symmetric linear array can be described by a generator array $\mathcal{G} \subset \mathbb{N}$ and a non-negative offset $l \in \mathbb{N}$, which determines the spacing between $\mathcal{G}$ and its mirror image $\max\mathcal{G} - \mathcal{G}$:

$$\mathcal{D}_{\text{S-}\mathcal{G}} \triangleq \mathcal{G} \cup (\max\mathcal{G} - \mathcal{G} + l).$$

The properties of this *symmetric array with generator* $\mathcal{G}$ (S-$\mathcal{G}$) are primarily determined by $\mathcal{G}$, which can be any array of choice. However, for the sum co-array of the S-$\mathcal{G}$ to be contiguous, both $\mathcal{G}$ and l should satisfy certain conditions (see Publication IX, Theorem 2, Corollaries 1 and 2).

A particularly useful sufficient condition is the following: if $\mathcal{G}$ has a contiguous difference co-array and the offset l is no larger than the number elements in the hole-free part of the sum co-array of $\mathcal{G}$, then the S-$\mathcal{G}$ has a contiguous sum (and difference) co-array. That is, if $\mathcal{G} - \mathcal{G} \supseteq \{0 : \max\mathcal{G}\}$ and $l \leq \max_{h \in \mathbb{N}_+}(h \mid \mathcal{G} + \mathcal{G} \supseteq \{0 : h-1\})$, then $\mathcal{D}_{\text{S-}\mathcal{G}} + \mathcal{D}_{\text{S-}\mathcal{G}} = \{0 : 2\max\mathcal{D}_{\text{S-}\mathcal{G}}\}$. Given a parametric $\mathcal{G}$ that satisfies this property, both the parameters of $\mathcal{G}$ and the offset l may be optimized.

Low-redundancy symmetric arrays with contiguous sum co-array

Publication I, III, and VII consider three symmetric arrays optimized for minimum redundancy: the *Concatenated Nested Array* (CNA), the *Interleaved Wichmann Array* (IWA), and the *Kløve Array* (KA).

The minimum-redundancy parameters of the CNA and IWA have closed-form expressions, whereas those of the KA can be found in linear time with respect to the number of sensors N. Publication IX, Proposition 1 establishes that the minimum-redundancy symmetric array with a Nested Array [200] generator is actually a CNA. The IWA and KA are symmetric arrays with Wichmann [294] and Kløve-Mossige basis [191] generators, respectively. Although neither the IWA nor KA is necessarily *the* minimum-redundancy symmetric array for the respective generator, they compare favorably with the CNA. In particular, the IWA achieves the same asymptotic redundancy as the CNA: $R_\infty = 2$, but has only approximately half the number of unit inter-sensor spacings: $S(1) \leq N/4 + 1$. The minimum-redundancy KA achieves the lowest asymptotic redundancy of any currently known scalable linear array with a contiguous sum co-array: $R_\infty = 23/12 < 1.92$ (see [130, Theorem, p. 177] or Publication IX, Proposition 2). The minimum-redundancy KA has approximately $S(1) \propto N/5.75$ unit spacings. Publication VII shows that the KA can also be constrained to achieve $S(1) = 8$ for any $N \geq 12$ at the cost of a slightly higher asymptotic redundancy $R_\infty = 2$. A low number of unit inter-sensor spacings can reduce the unwanted effects of mutual coupling, e.g., in direction finding, as demonstrated in Publication VII.

Comparison to asymmetric arrays with non-contiguous sum co-array

Fig. 4.11 shows the CNA, IWA and KA for $N = 14$ sensors, along with the respective sum and difference co-arrays. For reference, the generator arrays of these symmetric arrays (using the aperture maximizing parameters) are also

shown, i.e., the Nested Array (NA), Wichmann Array (WA), and Kløve-Mossige Array (KMA). Both the sum and difference co-arrays are contiguous for the CNA, IWA, and KA, whereas only the difference co-array is contiguous for the NA, WA and KMA. The WA achieves the largest difference co-array but has gaps in its sum co-array. The KMA and KA have the largest sum co-array.

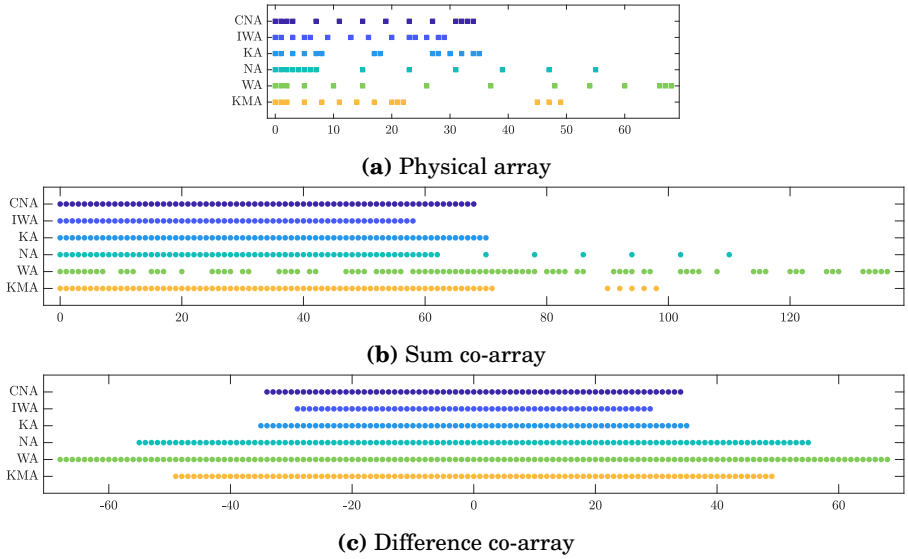

(a) Physical array

(b) Sum co-array

(c) Difference co-array

Figure 4.11. Sparse linear array configurations. The symmetric arrays have a contiguous sum and difference co-array, whereas the asymmetric arrays require a larger physical aperture to achieve a comparable sum co-array. The NA, WA, and KMA are the generators of the general symmetric arrays giving rise to the CNA, IWA, and KA.

The KMA actually has approximately 10% more sum co-array elements (both contiguous and in total) than the KA as the number of sensors approaches infinity (cf. Publication IX, Table V). For the same aperture (approaching infinity), the KA has 57% more sum co-array elements, but only 31% more physical sensors. Hence, the KA attains an increased number of DoFs for a given physical aperture, at the cost of a moderate increase in the number of physical sensors compared to the KMA. Compared to the MRA, the KA requires 0–27% more physical sensors to achieve the same physical aperture or number of DoFs. Unlike the MRA, the KA can be easily generated for any number of sensors.

4.4 Discussion

A key message of this chapter is that sparse array configurations with a contiguous sum co-array and minimal or low redundancy can be constructed for practically any number of sensors, aperture or aspect ratio. These arrays are suitable for active sensing applications where the physical dimensions of the array or the number of sensors and Tx/Rx front ends are tightly constrained.

The presented array configurations are nevertheless subject to further im-

provement. In fact, even the redundancy of the restricted MRA can be reduced by relaxing the requirement of a contiguous sum co-array and instead considering the general MRA problem. The reduction in redundancy comes at the price of a larger physical aperture for a given number of physical sensors or virtual DoFs. This may or may not be an issue, depending on the physical area available for placing the sensors. The general MRA is of significant theoretical interest, as it provides the least lower bound for the redundancy of any array. Appendix A.4 discusses the general MRA in further detail.

Novel array designs can likewise reduce the redundancy of the scalable sparse array configurations in Section 4.3. For example, extending the symmetric linear array framework in Section 4.3.3 to planar arrays may bridge the gap in the asymptotic redundancy between the presented strictly planar and linear arrays with $R_\infty = 2$ and $R_\infty \approx 1.92$, respectively. Lower redundancy linear arrays exist as well. In particular, Publication IX, Fig. 6 shows a noticeable gap in the (non-asymptotic) redundancy between the KA and MRA. The asymptotic redundancy of the KA may also be suboptimal, as indicated by the following argument: Recall from Section 2.4.1 that the observed ratio between the number of physical sensors of sum and difference MRAs with the same physical aperture closely matches $\sqrt{2} \approx 1.4$, which is in agreement with a simple counting argument based on the (non-)commutativity of the (difference) sum operator. Since the WA is a difference MRA for at least $14 \leq N \leq 26$ (cf. Section 2.2.2), and the ratio between the number of sensors in the KA and WA is $\sqrt{23}/3 \approx 1.6 > 1.4$, it is reasonable to expect that a scalable (contiguous sum co-array) configuration with $1 - 3\sqrt{2/23} \approx 12\%$ fewer sensors than the KA exists.

Finally, we remark that a principal advantage of the co-array perspective adopted in this work is that it is environment-independent. For example, two co-array equivalent arrays yield the same identifiability conditions in parameter estimation (provided the co-array is contiguous) [135], or achieve the same set of effective beampatterns [111]. Array design and signal processing can therefore be decoupled, which greatly simplifies both tasks. Naturally, this incurs a loss in optimality compared to the joint design. However, depending on the application, the cost may be acceptable when simplicity is prioritized, or online optimization and adaptation of the hardware cannot be afforded.

5. Active linear imaging using low-complexity architectures

Active sensing is concerned with detecting, classifying, and inferring properties about potential targets in the scattering scene based on observing the backscattering of the transmitted signals. Typical quantities of interest are the target locations (angle and range), powers, and velocities (Doppler shift). In case of the signal model in (3.5), we are mainly interested in the scatterer directions $\boldsymbol{v}_k$ and reflectivities γ_k. These parameters can be uniquely estimated, i.e., they are *identifiable*, when the number of independent measurements in (3.5) is larger than or equal to the number of unknowns. This is commonly the case in, for instance, radar, where the scattering scene only contains a few far field point targets [211, 306]. The co-array model establishes that the upper limit on the number of identifiable parameters is determined by the number of co-array elements [2, 135, 287, 165], rather than the number of physical sensors as is commonly assumed [256, 257]. However, the parameters are unidentifiable if the number scatterers is exceedingly large compared to the number of sensors, regardless of the number of co-array elements or temporal samples. Indeed, the number of point targets may even be uncountably infinite if the scatterers are continuous or distributed [277, 149, 221]. This is typically the case in medical ultrasound imaging, where internal organs and other scatterers of interest have complicated shapes. Useful information may nevertheless be extracted from this ill-posed problem in the form of an image, or a spatial spectrum estimate [255], of the scattering scene. Specifically, beamforming can reveal the spatial distribution and relative powers of the scatterers. In the identifiable case, i.e., when the number of point scatterers or parameters describing the extended scatterers is sufficiently small, methods such as MUSIC can provide improved resolution and statistical performance [143, 277]. This work focuses on linear imaging, where the parameters of the signal model may be unidentifiable. Our emphasis is on improving the resolution and decreasing the side lobe levels by utilizing the sum co-array in joint transmit-receive beamforming.

The chapter is organized as follows. Section 5.1 briefly reviews the basics of beamforming in active imaging, including relevant terminology and notation. Specifically, we consider image synthesis using *image addition* [111], i.e, multiple transmit and receive beamforming weight pairs corresponding to different

transmission-receptions or Tx waveforms. Section 5.2 analyzes the noise and interference suppression capability of image addition. Section 5.3 formulates an optimization problem for finding the beamforming weights that achieve a desired image fidelity using as component images as possible. We discuss approximate solutions to the posed optimization problems in the fully digital (Section 5.3.1), hybrid (Section 5.3.2), and fully analog beamforming (Section 5.3.3) cases.

5.1 Overview of active imaging using beamforming

Linear imaging refers to the formation of a spatial spectrum estimate, or image, by linear processing. In particular, we consider images consisting of a discrete grid of pixels, where each pixel corresponds beamformed output. Beamforming is widely employed in spatial spectrum estimation, since it requires minimal assumptions on the signal model. For example, scatterers do not need to be described by a finite number of parameters, nor does the array response need to be known exactly. Another advantage of beamforming is its low computational complexity, since it is a linear operation. The main disadvantages of beamforming are its diffraction limited resolution and poor statistical performance in parameter estimation due to bias [304, 275, 143]. Typical applications of linear imaging are diagnostic medical ultrasound, sonar, radar, and microwave imaging tasks, such as concealed weapon detection [13] and through-the-wall imaging [20, 107].

Next, we discuss beamforming and linear imaging in more detail. We describe the concept of the *point spread function* (PSF), which characterizes the key properties of a linear imaging system, such as the resolution and side lobe levels. We demonstrate the dependence of the PSF on the sum co-array, and review the image addition method for synthesizing arbitrary PSFs by multiple transmissions and receptions [111].

5.1.1 Joint transmit-receive beamforming

Beamforming refers to directional transmission or spatial filtering [279]. In transmit beamforming, the spatial self-interference of the radiated wavefield is controlled by appropriately scaling and phase shifting (or in general, delaying) the output of each Tx element so that they add constructively in desired directions. The resulting spatial distribution of radiated power is called a *beam* or a *beampattern*. In receive beamforming, the Rx sensor outputs are scaled and phase shifted prior to their addition. This beam can be flexibly shaped and steered post-acquisition, especially when the beamforming architecture of the receiver is fully digital. In contrast, the transmit beam is typically fixed for the duration of a pulse. In this work, we consider joint Tx-Rx beamforming, where the *effective* Tx-Rx beampattern is determined by the product of the Tx and Rx beampatters [252, 174], [261, Section 7.5.1]. The effective beampattern

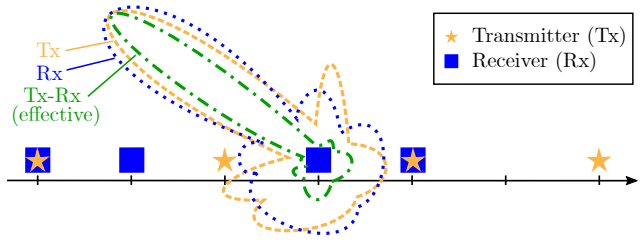

Figure 5.1. Beampatterns of an active array. The effective beampattern is the product of the Tx and Rx beampatterns. The Tx-Rx beampattern achieves a narrower main beam and lower side lobe levels than the Tx and Rx beampatterns. Adapted from Publication VIII, Fig. 2 © 2020 IEEE.

can therefore achieve a narrower main beam or lower side lobe levels than the individual Tx and Rx beampatterns, as illustrated in Fig. 5.1. Note that with planar arrays, beamforming is typically performed in two dimensions—azimuth and elevation. The beam may also be focused in range.

Following the general MIMO signal model in (3.4), the output of the beamformer can be expressed using the post matched filter received data matrix $\boldsymbol{X}$ as $y = \boldsymbol{c}_\mathrm{r}^\mathrm{T}\boldsymbol{X}\boldsymbol{w}_s = (\boldsymbol{w}_s \otimes \boldsymbol{c}_\mathrm{r})^\mathrm{T}\mathrm{vec}(\boldsymbol{X})$. Here $\boldsymbol{c}_\mathrm{r} \in \mathbb{C}^{M_\mathrm{r}}$ is a digital Rx beamforming vector, and $\boldsymbol{w}_s \in \mathbb{C}^{N_s}$ is a *waveform diversity weight vector* that linearly combines measurements corresponding to the different Tx waveforms post-acquisition. By (3.4), the beamformer output becomes

$$y = (\boldsymbol{w}_\mathrm{t} \otimes \boldsymbol{w}_\mathrm{r})^\mathrm{T}(\boldsymbol{A}_\mathrm{t} \odot \boldsymbol{A}_\mathrm{r})\boldsymbol{\gamma} + (\boldsymbol{S}^\mathrm{H}\boldsymbol{w}_s \otimes \boldsymbol{w}_\mathrm{r})^\mathrm{T}\boldsymbol{n}. \tag{5.1}$$

Recall that the Tx/Rx beamforming vectors $\boldsymbol{w}_\xi$ satisfy (3.6), where the digital Tx beamforming vector can be decomposed as

$$\boldsymbol{c}_\mathrm{t} = \boldsymbol{C}_s\boldsymbol{R}_s\boldsymbol{w}_s. \tag{5.2}$$

In (5.2), $\boldsymbol{C}_s \in \mathbb{C}^{M_\mathrm{t} \times N_s}$ is the digital waveform mixing matrix and $\boldsymbol{R}_s \in \mathbb{H}_{++}^{N_s}$ is the positive definite waveform cross-correlation matrix defined in (3.3). In (5.1), $\boldsymbol{S}$ is the $N_s \times T$ Tx waveform matrix and $\boldsymbol{n} \sim \mathcal{CN}(\boldsymbol{0}, \sigma^2\boldsymbol{I})$ a $N_\mathrm{r}T$-dimensional vector of i.i.d. spatio-temporally white circular complex Gaussian noise. Since a linear transformation of Gaussian random variables is Gaussian, the scalar noise component in (5.1) also follows a zero-mean complex-valued normal distribution, albeit with a different variance, i.e.,

$$(\boldsymbol{S}^\mathrm{H}\boldsymbol{w}_s \otimes \boldsymbol{w}_\mathrm{r})^\mathrm{T}\boldsymbol{n} \sim \mathcal{CN}(0, \sigma^2\|\boldsymbol{R}_s^{1/2}\boldsymbol{w}_s\|_2^2\|\boldsymbol{w}_\mathrm{r}\|_2^2). \tag{5.3}$$

Note that the effective $N_\mathrm{t}N_\mathrm{r}$-dimensional Tx-Rx beamforming vector $\boldsymbol{w}_\mathrm{t} \otimes \boldsymbol{w}_\mathrm{r}$ in (5.1) is the Kronecker product of the Tx and Rx beamforming vectors.

5.1.2 Linear imaging and image addition

The beamformer output is typically computed for a set of *pixels*—or *voxels* in three-dimensions—each corresponding to a distinct array steering direction and

Tx-Rx beamforming weight pair. An *image* is a collection of pixels, i.e., (5.1) evaluated for a finite set of Tx/Rx beamforming weight pairs. By the far field assumption (A2), the steering direction $\boldsymbol{u} \in \mathbb{R}^2$ of a given pixel can be written as[1]

$$\boldsymbol{u} = \begin{bmatrix} \sin\phi \sin\vartheta & \cos\vartheta \end{bmatrix}^{\mathrm{T}},$$

where $\phi \in [-\pi/2, \pi/2]$ and $\vartheta \in [0, \pi]$ denote the azimuth and elevation angles, respectively. If more than one of the pixels correspond to same transmission, then the noise is correlated between pixels. This may be the case in, e.g., medical ultrasound imaging, where the number of Tx beams (focal points) is often lower than the number of Rx beams [261, p. 194].

Image addition

Image addition is a method for synthesizing a high-quality composite image by adding together several *component images* of possibly lower quality [111]. This may come at the cost of an increased image acquisition time, depending on the degree of waveform diversity. As illustrated in Fig. 5.2, image addition suppresses side or grating lobes, which may arise due to the employed sparse array geometry or hybrid/analog beamforming architecture.

In particular, consider the effective Tx-Rx beamforming weight vector

$$\boldsymbol{w}_{\mathrm{t}} \otimes \boldsymbol{w}_{\mathrm{r}} = \mathrm{vec}\left(\boldsymbol{w}_{\mathrm{r}} \boldsymbol{w}_{\mathrm{t}}^{\mathrm{T}}\right).$$

Clearly, the range of this vector is limited by the rank-1 matrix $\boldsymbol{w}_{\mathrm{r}} \boldsymbol{w}_{\mathrm{t}}^{\mathrm{T}}$. To overcome this limitation, image addition instead considers the Q-fold sum

$$\sum_{q=1}^{Q} \boldsymbol{w}_{\mathrm{t},q} \otimes \boldsymbol{w}_{\mathrm{r},q} = \mathrm{vec}(\boldsymbol{W}), \quad \text{where} \quad \boldsymbol{W} \triangleq \sum_{q=1}^{Q} \boldsymbol{w}_{\mathrm{r},q} \boldsymbol{w}_{\mathrm{t},q}^{\mathrm{T}} \tag{5.4}$$

is the $N_{\mathrm{r}} \times N_{\mathrm{t}}$ *co-array weight matrix*, and $\boldsymbol{w}_{\xi,q} \mathbb{C}^{N_\xi}$ denotes the Tx/Rx beamforming weight vector of the qth component image. The output of the beamformer in (5.1) after image addition thus becomes

$$y = \sum_{q=1}^{Q} (\boldsymbol{w}_{\mathrm{t},q} \otimes \boldsymbol{w}_{\mathrm{r},q})^{\mathrm{T}} (\boldsymbol{A}_{\mathrm{t}} \odot \boldsymbol{A}_{\mathrm{r}}) \boldsymbol{\gamma} + \sum_{q=1}^{Q} (\boldsymbol{S}^{\mathrm{H}} \boldsymbol{w}_{s,q} \otimes \boldsymbol{w}_{\mathrm{r},q})^{\mathrm{T}} \boldsymbol{n}_q, \tag{5.5}$$

where $\boldsymbol{n}_q \in \mathbb{C}^{N_{\mathrm{r}} T}$ is the noise vector of the qth component image, and $\boldsymbol{w}_{s,q} \in \mathbb{C}^{N_s}$ is the corresponding waveform diversity combining vector.

Number of component images versus pulses

The number of component images Q generally depends on the performance requirements of the beamformer. Factors influencing the value of Q are, e.g., the array geometry, beamforming architecture, desired beampattern (affecting the reconstruction fidelity of the final image), and the tolerated image

[1] Vector $\boldsymbol{u}$ contains the x and y components of the three-dimensional unit vector pointing in the direction of the pixel. The xy-plane contains the Tx and Rx sensors (see Fig. 3.1b).

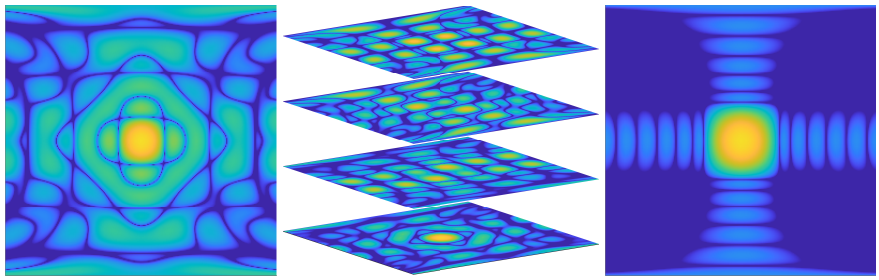

(a) Single image **(b)** Component images **(c)** Composite image

Figure 5.2. Image addition. The fidelity of a single component image ($Q = 1$) is improved by summing multiple component images into a composite image ($Q = 4$).

acquisition time. For example, if the beamforming weights are unconstrained, then any $N_\mathrm{t}N_\mathrm{r}$-dimensional effective beamforming vector can be achieved using $Q = \mathrm{rank}(\boldsymbol{W}) \leq \min(N_\mathrm{t}, N_\mathrm{r})$ component images by application of singular value decomposition (SVD), as we will show in Section 5.3.1.

In the general MIMO beamforming model (5.5), Q does not necessarily equal the number of transmissions and receptions, or pulses, P. Due to waveform diversity, a single pulse yields as many unique component images as the number of linearly independent transmit waveforms N_s. Generally, the number of component images can be up to $Q = PN_s$. As we consider Q to be the main free variable in this thesis, the number of pulses should satisfy

$$P = \lceil Q/N_s \rceil. \tag{5.6}$$

By (3.6) and (5.2), the qth transmit beamforming weight vector corresponding to the pth transmission can therefore be written as

$$\boldsymbol{w}_{\mathrm{t},q} = \boldsymbol{F}_{\mathrm{t},p}\boldsymbol{C}_{s,p}\boldsymbol{R}_s\boldsymbol{w}_{s,q},$$

where $\boldsymbol{F}_{\mathrm{t},p}$ is the $N_\mathrm{t} \times M_\mathrm{t}$ Tx phase shift matrix. The pulse and component image indices satisfy $p = 1, 2, \ldots, P$ and $q \in \mathscr{I}_p \subseteq \{1 : Q\}$, where set

$$\mathscr{I}_p \triangleq \big\{(p-1)N_s + 1 : \min(pN_s, Q)\big\} \tag{5.7}$$

contains the indices of the component images corresponding to the pth pulse. Equivalently, the qth waveform diversity vector of dimension N_s can be chosen as $\boldsymbol{w}_{s,q} = (\boldsymbol{F}_{\mathrm{t},p}\boldsymbol{C}_{s,p}\boldsymbol{R}_s)^\dagger \boldsymbol{w}_{\mathrm{t},q}$ to achieve a desired $\boldsymbol{w}_{\mathrm{t},q}$, since the transmission-specific beamforming matrix $\boldsymbol{F}_{\mathrm{t},p}\boldsymbol{C}_{s,p} \in \mathbb{C}^{N_\mathrm{t} \times N_s}$ has full column rank. Here $(\cdot)^\dagger$ denotes the Moore-Penrose pseudoinverse.

Finally, it is instructive to consider (5.6) in the case of the O-MIMO and PA architectures discussed in Section 3.3.2. In the (fully digital) O-MIMO case, a single pulse ($P = 1$) suffices to achieve any PSF supported on the sum co-array. This holds regardless of the value of Q, since $N_s = N_\mathrm{t}$ and $Q \leq \min(N_\mathrm{t}, N_\mathrm{r})$. Using more than $\min(N_\mathrm{t}, N_\mathrm{r})$ component images ($P \geq 2$ pulses) improves the SNR, although multiple pulses are not necessary from the point of view of image addition. In contrast, the PA architecture requires $P = Q$ pulses, since $N_s = 1$.

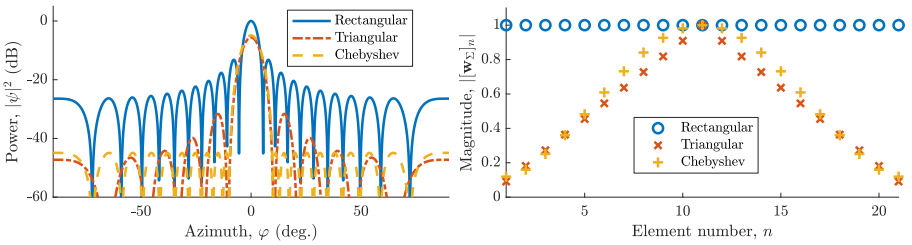

(a) Point spread function **(b)** Sum co-array weights

Figure 5.3. PSFs corresponding to typical beamforming weight choices. There is a general trade-off among the main lobe width, side lobe levels, and array gain.

5.1.3 Point spread function

The *point spread function* (PSF) is the spatial impulse response of a linear imaging system [91, p. 20]. The effective PSF of an active array, determined by the product of the Tx and Rx PSFs, fully characterizes the achievable resolution and interference suppression capability of the imaging system. In general, the PSF is a complex-valued function defined as

$$\psi(\boldsymbol{u},\boldsymbol{v}) \triangleq \mathrm{vec}^{\mathrm{T}}(\boldsymbol{W}(\boldsymbol{u}))(\boldsymbol{a}_{\mathrm{t}}(\boldsymbol{v}) \otimes \boldsymbol{a}_{\mathrm{r}}(\boldsymbol{v})), \tag{5.8}$$

where $\boldsymbol{u} \in \mathbb{R}^2$ is the focusing direction of the array (in the xy-plane), and $\boldsymbol{v} \in \mathbb{R}^2$ is the direction of a unit reflectivity point-scatterer. Fig. 5.3 shows examples of common one-dimensional PSFs. Image addition allows for any linear array with a contiguous sum co-array of appropriate size to achieve any of these PSFs.

Space invariance

The PSF is *space-invariant* or *isoplanatic* if $\psi(\boldsymbol{u},\boldsymbol{v}) = \psi(\boldsymbol{v}-\boldsymbol{u})$ holds [91, p. 21]. For example, consider the weighted *spatial matched filter* with

$$\boldsymbol{w}_\xi(\boldsymbol{u}) = \boldsymbol{w}_\xi \circ \boldsymbol{a}_\xi^*(\boldsymbol{u}). \tag{5.9}$$

Here $\boldsymbol{w}_\xi \in \mathbb{C}^{N_\xi}$ is a direction-independent apodization vector, and $\boldsymbol{a}_\xi^*(\boldsymbol{u})$ is the complex conjugate of the Tx/Rx array steering vector in direction $\boldsymbol{u}$. Consequently, the PSF becomes

$$\psi(\boldsymbol{v},\boldsymbol{u}) = \mathrm{vec}^{\mathrm{T}}(\boldsymbol{W})\big((\boldsymbol{a}_{\mathrm{t}}(\boldsymbol{v}) \circ \boldsymbol{a}_{\mathrm{t}}^*(\boldsymbol{u})) \otimes (\boldsymbol{a}_{\mathrm{r}}(\boldsymbol{v}) \circ \boldsymbol{a}_{\mathrm{r}}^*(\boldsymbol{u}))\big),$$

where the effective apodization vector $\mathrm{vec}(\boldsymbol{W})$ following (5.4) is independent of $\boldsymbol{u}$. By the omnidirectional sensor assumption in (A4), the PSF reduces to

$$\psi(\boldsymbol{v}-\boldsymbol{u}) = \mathrm{vec}^{\mathrm{T}}(\boldsymbol{W})(\boldsymbol{a}_{\mathrm{t}}(\boldsymbol{v}-\boldsymbol{u}) \otimes \boldsymbol{a}_{\mathrm{r}}(\boldsymbol{v}-\boldsymbol{u})), \tag{5.10}$$

which is space-invariant, as it only depends on the difference $\boldsymbol{v}-\boldsymbol{u}$. The fact that matrix $\boldsymbol{W}$ does not depend on $\boldsymbol{u}$ considerably simplifies the task of designing the beamforming weights.

Connection to sum co-array

The PSF can be interpreted as the spatial Fourier transform of the virtual beamforming weights of the sum co-array [111]. Indeed, this Fourier transform pair is analogous to that of the physical beamforming weights and beampattern of an ideal array [278, p. 95]. Hence, a desired PSF is achieved by appropriately designing the sum co-array weights. In particular, let $\boldsymbol{\psi} \triangleq [\psi(\boldsymbol{v}_1), \psi(\boldsymbol{v}_2), \ldots, \psi(\boldsymbol{v}_V)]^{\mathrm{T}} \in \mathbb{C}^V$ denote the PSF sampled in V distinct directions $\{\boldsymbol{v}_i\}_{i=1}^V$. By (5.10) and (3.16), this can be written as

$$\boldsymbol{\psi} = (\boldsymbol{A}_{\mathrm{t}} \odot \boldsymbol{A}_{\mathrm{r}})^{\mathrm{T}} \operatorname{vec}(\boldsymbol{W}) = \boldsymbol{A}_{\Sigma}^{\mathrm{T}} \boldsymbol{w}_{\Sigma}. \tag{5.11}$$

Here, $\boldsymbol{w}_{\Sigma} \in \mathbb{C}^{N_{\Sigma}}$ is the *sum co-array beamforming weight vector*, defined as

$$\boldsymbol{w}_{\Sigma} \triangleq \boldsymbol{\Upsilon} \operatorname{vec}(\boldsymbol{W}), \tag{5.12}$$

and $\boldsymbol{\Upsilon} \in \{0,1\}^{N_{\Sigma} \times N_{\mathrm{r}} N_{\mathrm{t}}}$ is the co-array selection matrix in (3.17). The effective and sum co-array steering matrices $\boldsymbol{A}_{\mathrm{t}} \odot \boldsymbol{A}_{\mathrm{r}} \in \mathbb{C}^{N_{\mathrm{r}} N_{\mathrm{t}} \times V}$ and $\boldsymbol{A}_{\Sigma} \in \mathbb{C}^{N_{\Sigma} \times V}$, respectively, are sampled in the same V directions as $\boldsymbol{\psi}$. If $\operatorname{rank}(\boldsymbol{A}_{\Sigma}) = N_{\Sigma}$, implying that $V \geq N_{\Sigma}$, then the mapping between $\boldsymbol{\psi}$ and $\boldsymbol{w}_{\Sigma}$ in (5.11) is one-to-one (invertible).

5.2 Noise and interference suppression capability

The noise and interference suppression capability of image addition is clarified by decomposing the beamformer output into three terms: a *signal of interest* (SoI) term, an interference term, and a noise term. Assuming w.l.o.g. that the array is steered in the direction of the SoI, i.e., $\boldsymbol{u} = \boldsymbol{v}_1$, and that the remaining $K-1$ scatterers act as interferers, (5.5) becomes

$$y(\boldsymbol{u}) = \gamma_1 \psi(\boldsymbol{0}) + \sum_{i=2}^{K} \gamma_i \psi(\boldsymbol{v}_i - \boldsymbol{u}) + n\alpha(\boldsymbol{u}).$$

Here ψ is the (space-invariant) PSF in (5.10), $n \sim \mathcal{CN}(0, \sigma^2)$ is measurement noise, and α is a normalization factor that—assuming the noise in (5.5) is uncorrelated between pulses—reduces to (see Appendix A.5)

$$\alpha(\boldsymbol{u}) = \sqrt{\sum_{p=1}^{\lceil Q/N_s \rceil} \left\| \sum_{q \in \mathscr{I}_p} \boldsymbol{R}_s^{1/2} \boldsymbol{w}_{s,q}(\boldsymbol{u}) \otimes \boldsymbol{w}_{\mathrm{r},q}(\boldsymbol{u}) \right\|_2^2}.$$

Recall that $\mathscr{I}_p$ is the set of component image indices corresponding to the pth pulse, as defined in (5.7).

By the coherent scatterer assumption (A2), the SINR becomes

$$\mathrm{SINR} \triangleq \frac{\mathbb{E}\left(|\gamma_1 \psi(\boldsymbol{0})|^2\right)}{\mathbb{E}\left(\left|\sum_{i=2}^{K} \gamma_i \psi(\boldsymbol{v}_i - \boldsymbol{u}) + n\alpha(\boldsymbol{u})\right|^2\right)} = \frac{|\gamma_1|^2 |\psi(\boldsymbol{0})|^2}{\left|\sum_{i=2}^{K} \gamma_i \psi(\boldsymbol{v}_i - \boldsymbol{u})\right|^2 + \sigma^2 |\alpha(\boldsymbol{u})|^2}.$$

The effect the PSF, and specifically, image addition, has on the SINR is of particular interest in the following two special cases:

- Interference-limited regime, $\left|\sum_{i=2}^{K}\gamma_i\psi(\boldsymbol{v}_i-\boldsymbol{u})\right|^2 \gg \sigma^2|\alpha(\boldsymbol{u})|^2$
- Noise-limited regime, $\left|\sum_{i=2}^{K}\gamma_i\psi(\boldsymbol{v}_i-\boldsymbol{u})\right|^2 \ll \sigma^2|\alpha(\boldsymbol{u})|^2$.

Next, we consider both of these cases separately, with an emphasis on the latter.

5.2.1 Interference-limited regime

In the interference-limited regime, the SINR is completely characterized by the PSF and the scattering coefficients. Image addition may therefore improve the SINR by suitably shaping the PSF. However, emitters that do not interact with active illumination, or only backscatter weakly, will be indifferent to the Tx beam. The imaging system is therefore susceptible to active interference in directions where the Rx beam has high side lobes, regardless of the effective Tx-Rx beampattern.

The SINR in the interference-limited regime largely depends on the scattering scene. A detailed, yet sufficiently general quantitive analysis lies beyond the scope of this work. Instead, we focus on the noise-limited regime in the following.

5.2.2 Noise-limited regime

In the noise limited regime, the SINR reduces to the SNR, which is defined as

$$\mathrm{SNR} \triangleq \frac{\mathbb{E}\left(|\gamma_1\psi(\mathbf{0})|^2\right)}{\mathbb{E}\left(|n\alpha(\boldsymbol{u})|^2\right)} = \frac{|\gamma_1|^2}{\sigma^2}\left|\frac{\psi(\mathbf{0})}{\alpha(\boldsymbol{u})}\right|^2.$$

The SNR crucially depends on the beamforming gain, which is quantified by the magnitude of $\psi/\alpha = \boldsymbol{w}_{\mathrm{tr}}^{\mathrm{T}}(\boldsymbol{a}_{\mathrm{t}}\otimes\boldsymbol{a}_{\mathrm{r}})$, where $\boldsymbol{w}_{\mathrm{tr}} \triangleq \mathrm{vec}(\boldsymbol{W})/\alpha$ is the normalized effective beamforming vector of the imaging system. Consequently, we have

$$\mathrm{SNR} = \frac{|\gamma_1|^2}{\sigma^2}|\boldsymbol{w}_{\mathrm{tr}}^{\mathrm{T}}(\boldsymbol{a}_{\mathrm{t}}\otimes\boldsymbol{a}_{\mathrm{r}})|^2 \leq \frac{|\gamma_1|^2}{\sigma^2}\|\boldsymbol{w}_{\mathrm{tr}}\|_2^2 N_{\mathrm{t}}N_{\mathrm{r}} \tag{5.13}$$

by the Cauchy-Schwartz inequality—assuming unit magnitude steering vector entries. The main quantity of interest $\|\boldsymbol{w}_{\mathrm{tr}}\|_2^2 = \|\boldsymbol{W}\|_{\mathrm{F}}^2/|\alpha|^2$ can be written as

$$\|\boldsymbol{w}_{\mathrm{tr}}\|_2^2 = \frac{\sum_{q=1}^{Q}\sum_{l=1}^{Q}\boldsymbol{w}_{\mathrm{t},q}^{\mathrm{H}}\boldsymbol{w}_{\mathrm{t},l}\boldsymbol{w}_{\mathrm{r},q}^{\mathrm{H}}\boldsymbol{w}_{\mathrm{r},l}}{\sum_{p=1}^{\lceil Q/N_s\rceil}\sum_{q,l\in\mathscr{I}_p}\boldsymbol{w}_{s,q}^{\mathrm{H}}\boldsymbol{R}_s\boldsymbol{w}_{s,l}\boldsymbol{w}_{\mathrm{r},q}^{\mathrm{H}}\boldsymbol{w}_{\mathrm{r},l}}. \tag{5.14}$$

The numerator of (5.14) contains the cross-correlations between the Tx/Rx beamforming weight vectors of all component image pairs. Similarly, the denominator contains the cross-correlations of the post-acquisition beamforming vectors (related to the Rx and waveform diversity weights). In contrast to the numerator, the inner products in the denominator are only between component image pairs corresponding to the same pulse. In case of the phased array (PA) and orthogonal

MIMO (O-MIMO) architectures (cf. Section 3.3.2), (5.14) simplifies to:

$$\|\boldsymbol{w}_{\mathrm{tr}}\|_2^2 = \begin{cases} \dfrac{\sum_{q=1}^{Q}\sum_{l=1}^{Q} \boldsymbol{w}_{\mathrm{t},q}^{\mathrm{H}}\boldsymbol{w}_{\mathrm{t},l}\boldsymbol{w}_{\mathrm{r},q}^{\mathrm{H}}\boldsymbol{w}_{\mathrm{r},l}}{\sum_{q=1}^{Q}\|\boldsymbol{w}_{\mathrm{r},q}\|_2^2}, & \text{if PA} \\ 1 + \dfrac{\sum_{p,r=1;r\neq p}^{\lceil Q/N_{\mathrm{t}}\rceil}\sum_{q\in\mathscr{I}_p}\sum_{l\in\mathscr{I}_r} \boldsymbol{w}_{s,q}^{\mathrm{H}}\boldsymbol{w}_{s,l}\boldsymbol{w}_{\mathrm{r},q}^{\mathrm{H}}\boldsymbol{w}_{\mathrm{r},l}}{\sum_{p=1}^{\lceil Q/N_{\mathrm{t}}\rceil}\sum_{q,l\in\mathscr{I}_p} \boldsymbol{w}_{s,q}^{\mathrm{H}}\boldsymbol{w}_{s,l}\boldsymbol{w}_{\mathrm{r},q}^{\mathrm{H}}\boldsymbol{w}_{\mathrm{r},l}}, & \text{if O-MIMO.} \end{cases}$$

The maximum SNR of the O-MIMO architecture is less affected than the PA by the number of component images Q due to the lack of Tx combining gain. In the O-MIMO case, $\|\boldsymbol{w}_{\mathrm{tr}}\|_2^2$ only depends ratio of the *inter-* and *intra-*pulse cross-correlations of the beamforming weights. Indeed, if $Q \leq N_{\mathrm{t}}$ then $\|\boldsymbol{w}_{\mathrm{tr}}\|_2^2 = 1$, since a single pulse is sufficient to obtain any sum co-array weighting.

For further insight into (5.14), we next examine the single component image case, $Q = 1$, and then extend our analysis to the general case, $Q \geq 1$. Note that Q and the number of linearly independent Tx waveforms N_s are considered free variables, whereas the number of pulses is determined as $P = \lceil Q/N_s \rceil$.

Single component image, $Q = 1$

When $Q = 1$, the expression in (5.14) simplifies by (3.6) and (5.2) to

$$\|\boldsymbol{w}_{\mathrm{tr}}\|_2^2 = \frac{\|\boldsymbol{w}_{\mathrm{t}}\|_2^2}{\|\boldsymbol{R}_s^{1/2}\boldsymbol{w}_s\|_2^2} = \frac{\|\boldsymbol{F}_{\mathrm{t}}\boldsymbol{C}_s\boldsymbol{R}_s\boldsymbol{w}_s\|_2^2}{\|\boldsymbol{R}_s^{1/2}\boldsymbol{w}_s\|_2^2} \leq \|\boldsymbol{F}_{\mathrm{t}}\boldsymbol{C}_s\boldsymbol{R}_s^{1/2}\|_2^2. \tag{5.15}$$

The final step in (5.15) follows from the Cauchy-Schwartz inequality, or by noting that (5.15) is a Rayleigh quotient, whose maximum is the largest singular value (squared) of matrix $\boldsymbol{F}_{\mathrm{t}}\boldsymbol{C}_s\boldsymbol{R}_s^{1/2}$. Consequently, (5.15) holds with equality when the waveform diversity weight vector $\boldsymbol{w}_s = \boldsymbol{R}_s^{-1/2}\boldsymbol{r}_1$, where $\boldsymbol{r}_1$ is the (arbitrarily scaled but nonzero) leading right singular vector of $\boldsymbol{F}_{\mathrm{t}}\boldsymbol{C}_s\boldsymbol{R}_s^{1/2}$.

Eq. (5.15) is independent of the Rx beamforming vector, which mainly affects the SINR by shaping the PSF. Hence, the SNR is primarily limited by the transmit combining gain, which is characterized by the largest singular value of the $N_{\mathrm{t}} \times N_s$ matrix $\boldsymbol{F}_{\mathrm{t}}\boldsymbol{C}_s\boldsymbol{R}_s^{1/2}$. This reduces to the squared norm of the Tx beamforming vector $\boldsymbol{w}_{\mathrm{t}}$ when $N_s = 1$. Typically, the power per Tx sensor or total Tx power is constrained, which means that $\|\boldsymbol{w}_{\mathrm{t}}\|_2^2$ is fixed. For example, consider the PA with spatially matched beamforming weights $\boldsymbol{w}_{\mathrm{t}} = \boldsymbol{a}_{\mathrm{t}}^*$ and $\boldsymbol{w}_{\mathrm{r}} = c\boldsymbol{a}_{\mathrm{r}}^*$, where $c \in \mathbb{C} \setminus \{0\}$ is an arbitrary nonzero constant. This beamformer maximizes the SNR assuming that each Tx sensor is operating at full power such that $\|\boldsymbol{w}_{\mathrm{t}}\|_2^2 = N_{\mathrm{t}}$. In this case, (5.13) yields the well-known result (cf. [124, Eq. (20)])

$$\mathrm{SNR} \propto N_{\mathrm{t}}^2 N_{\mathrm{r}},$$

that is, the SNR is proportional to the square of the number of Tx sensors and scales linearly with the number of Rx sensors. In the O-MIMO case we have $\mathrm{SNR} \propto N_{\mathrm{t}}N_{\mathrm{r}}$. The Tx combining gain of the PA thus yields an SNR gain of a factor N_{t} compared to the O-MIMO case. This holds regardless if the total Tx power scales with the number of Tx sensors (as is assumed here) or not.

Multiple component images, $Q \geq 1$

When $Q \geq 1$, two extreme cases emerge, where the beamforming weights are either mutually *orthogonal*, or *identical* between component images. Eq. (5.14) simplifies substantially in both cases, which helps clarify the influence of image addition on the SNR.

- **Orthogonal Tx/Rx weights**, i.e., $\boldsymbol{w}_{\mathrm{t},q}^{\mathrm{H}}\boldsymbol{w}_{\mathrm{t},l} = 0$ or $\boldsymbol{w}_{\mathrm{r},q}^{\mathrm{H}}\boldsymbol{w}_{\mathrm{r},l} = 0 \ \forall \ q \neq l$:

$$\|\boldsymbol{w}_{\mathrm{tr}}\|_2^2 = \frac{\sum_{q=1}^{Q} \|\boldsymbol{w}_{\mathrm{t},q}\|_2^2 \|\boldsymbol{w}_{\mathrm{r},q}\|_2^2}{\sum_{q=1}^{Q} \|\boldsymbol{R}_s^{1/2}\boldsymbol{w}_{s,q}\|_2^2 \|\boldsymbol{w}_{\mathrm{r},q}\|_2^2}.$$

  The Cauchy-Schwartz inequality and (5.2) then yield an upper bound on the normalized beamforming weight vector of the imaging system:

$$\|\boldsymbol{w}_{\mathrm{tr}}\|_2^2 \leq \max_{q\in\{1:Q\}} \|\boldsymbol{F}_{\mathrm{t},q}\boldsymbol{C}_{s,q}\boldsymbol{R}_s^{1/2}\|_2^2 = \begin{cases} \max\limits_{q\in\{1:Q\}} \|\boldsymbol{w}_{\mathrm{t},q}\|_2^2, & \text{if PA} \\ 1, & \text{if O-MIMO.} \end{cases} \tag{5.16}$$

  If the Tx beamforming weights are further normalized as $\|\boldsymbol{w}_{\mathrm{t},q}\|_2^2 = N_{\mathrm{t}}$, then by (5.13) the PA has $\mathrm{SNR} \propto N_{\mathrm{t}}^2 N_{\mathrm{r}}$ (O-MIMO has $\mathrm{SNR} \propto N_{\mathrm{t}} N_{\mathrm{r}}$).

- **Identical Tx/Rx weights**, i.e., $\boldsymbol{w}_{\mathrm{t},q} = \boldsymbol{w}_{\mathrm{t},l}$ and $\boldsymbol{w}_{\mathrm{r},q} = \boldsymbol{w}_{\mathrm{r},l} \ \forall \ q,l$:

$$\|\boldsymbol{w}_{\mathrm{tr}}\|_2^2 = \frac{Q^2 \|\boldsymbol{w}_{\mathrm{t}}\|_2^2}{\sum_{p=1}^{\lceil Q/N_s \rceil} \sum_{q,l\in\mathscr{I}_p} \boldsymbol{w}_{s,q}^{\mathrm{H}}\boldsymbol{R}_s\boldsymbol{w}_{s,l}}.$$

  Further assuming that $\boldsymbol{w}_{s,q} = \boldsymbol{w}_{s,l} \neq \boldsymbol{0} \ \forall \ q,l,p$ yields

$$\|\boldsymbol{w}_{\mathrm{tr}}\|_2^2 \leq \left\lceil \frac{Q}{N_s} \right\rceil \min_{q\in\{1:Q\}} \|\boldsymbol{F}_{\mathrm{t},q}\boldsymbol{C}_{s,q}\boldsymbol{R}_s^{1/2}\|_2^2 = \begin{cases} Q\|\boldsymbol{w}_{\mathrm{t}}\|_2^2, & \text{if PA} \\ \lceil Q/N_{\mathrm{t}} \rceil, & \text{if O-MIMO.} \end{cases} \tag{5.17}$$

  If $\|\boldsymbol{w}_{\mathrm{t}}\|_2^2 = N_{\mathrm{t}}$, then the PA has $\mathrm{SNR} \propto Q N_{\mathrm{t}}^2 N_{\mathrm{r}}$ (O-MIMO has $\mathrm{SNR} \propto \max(Q, N_{\mathrm{t}}) N_{\mathrm{r}}$).

Eq. (5.16) establishes that image addition using orthogonal beamforming weights cannot markedly increase the SNR compared to the single component image case. Multiple component images may nevertheless improve the SINR by facilitating a wider selection of PSFs. The orthogonal case is of particular interest in fully digital beamforming, where SVD can be used to find the beamforming weights.

Eq. (5.17) agrees with the intuition that the SNR increases linearly with the number of pulses $\lceil Q/N_s \rceil$ when employing identical beamforming weights. This corresponds to reducing noise by summing identical images with independent noise realizations obtained over multiple pulses. However, the interference suppression capability does not improve, since the set of achievable PSFs is limited to that of a single component image.

Often the beamforming weights of different component images are not completely identical nor orthogonal. For example, the hybrid or fully analog beamforming architectures discussed in Sections 5.3.2 and 5.3.3 impose constraints on the beamforming weights that may prevent orthogonality. The exact SNR can nonetheless be computed by evaluating (5.13) numerically.

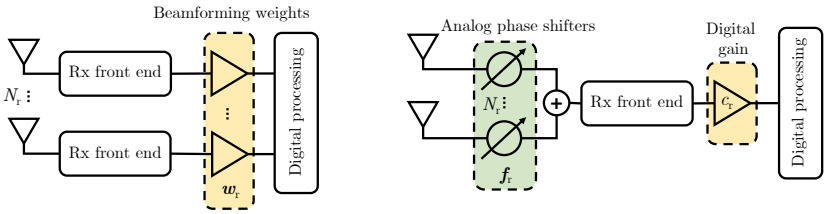

(a) Fully digital receiver **(b)** Fully analog receiver

Figure 5.4. Fully (a) digital and (b) analog beamforming architectures. The digital receiver has unconstrained beamforming weights, but requires an expensive Rx front end for each sensors. The analog receiver only has a single front end, but the beamforming weights are constrained to phase shifts with a common gain. See also Fig. 3.2 for the general hybrid case including the transmitter. Adapted in part from Publication VI, Fig. 1 © 2019 IEEE.

5.3 Low-complexity imaging using few component images

Fig. 5.4 illustrates the fully digital and analog beamforming architectures introduced in Section 3.3.1. Historically, beamforming architectures were analog in applications, such as, communications, radar, and sonar [109, 87, 131]. Over the past decades, digital architectures have become more commonplace, especially at microwave frequencies, thanks to the proliferation of and advances in digital hardware and computing [87]. There has recently been a revived interest in combining analog and digital processing in hybrid beamforming architectures (see Fig. 3.2 in Section 3.3.1). A key driving force behind this trend is mmWave and beyond communications and sensing. This paradigm envisions using arrays with a large number of antennas—up to hundreds or even thousands—packed in a small physical area. Prime examples include 5G communications and automotive radar [100, 204]. However, at frequencies approaching the THz regime, fully digital beamforming is still infeasible and hybrid or fully analog architectures are employed instead. The main drawbacks of high hardware costs and power consumption [226, p. 128] can be alleviated by reducing the number of Tx/Rx front ends and assigning part of the processing to the analog domain using inexpensive phase shifter networks.

Another means to reduce the number of front ends is to employ fewer physical sensors. Sparse arrays can be used in conjunction with non-digital beamforming architectures to achieve further savings. As an extreme example, consider the difference between a fully digital URA with N sensors and Tx/Rx front ends, and an co-array equivalent fully analog sparse array, such as the MRA, with $\mathcal{O}\left(\sqrt{N}\right)$ sensors and a single front end. Alternatively, for the same number of sensors, a sparse array with a hybrid beamforming architecture can outperform a fully digital uniform array in, e.g., DoA estimation tasks [114, 96, 137].

This section considers hybrid beamforming in the context of active sensing. In particular, we study linear imaging using fully digital (Section 5.3.1), hybrid (Section 5.3.2), and fully analog (Section 5.3.3) beamforming architectures at both the transmitter and receiver. We assume that both the Tx and Rx array

has the same beamforming architecture for simplicity. We focus on image addition and formulate novel optimization problems for finding the beamforming weights achieving a desired PSF using as few component images as possible. By virtue of the sum co-array model adopted in this work, our discussion naturally accommodates both uniform and sparse array configurations. Details of the results presented in the section may be found in Publication II, VI, and VIII.

5.3.1 Fully digital beamforming

A fully digital beamforming architecture has a dedicated Tx or Rx front end for each sensor, which means that $M_\xi = N_\xi$. This provides maximum flexibility in signal processing, but comes at the expense of high cost and power consumption. Since a fully digital architecture does not require phase shifters, the phase shift matrices $\boldsymbol{F}_\xi$ reduce to identity matrices ($\boldsymbol{F}_\xi = \boldsymbol{I}$). By (5.2), the Tx and Rx beamforming weight vectors are unconstrained, i.e., $\boldsymbol{w}_\xi \in \mathbb{C}^{N_\xi}$, which implies that they may be recovered from the SVD of co-array weight matrix $\boldsymbol{W}$ in (5.4). Specifically, let the SVD of $\boldsymbol{W}$ be $\boldsymbol{W} = \boldsymbol{U}\boldsymbol{\Sigma}\boldsymbol{V}^{\mathrm{H}}$ and denote

$$\boldsymbol{W} = \sum_{q=1}^{Q} \boldsymbol{w}_{\mathrm{r},q}\boldsymbol{w}_{\mathrm{t},q}^{\mathrm{T}} = \boldsymbol{W}_{\mathrm{r}}\boldsymbol{W}_{\mathrm{t}}^{\mathrm{T}},$$

where matrix $\boldsymbol{W}_\xi \in \mathbb{C}^{N_\xi \times Q}$ contains the respective Tx/Rx beamforming weights of all component images. A valid choice for the beamforming weight matrices is, for example, $\boldsymbol{W}_{\mathrm{r}} = \boldsymbol{U}\boldsymbol{\Sigma}$ and $\boldsymbol{W}_{\mathrm{t}} = \boldsymbol{V}^*$, where $\boldsymbol{U}$ and $\boldsymbol{V}$ are unitary matrices. To ensure that least one sensor is transmitting at full power, we may additionally multiply $\boldsymbol{W}_{\mathrm{t}}$ (and $\boldsymbol{W}_{\mathrm{r}}$) from the left (right) by an appropriate normalizing diagonal matrix (and its inverse).

Least squares beamforming weights

Matrix $\boldsymbol{W}$ may be found by minimizing the ℓ_2 approximation error between the desired and realized co-array weighting (or PSF), defined as

$$\varepsilon \triangleq \left\| \boldsymbol{w}_\Sigma - \boldsymbol{\Upsilon}\,\mathrm{vec}(\boldsymbol{W}) \right\|_2^2. \tag{5.18}$$

Infinitely many $\boldsymbol{W}$ minimizing $\varepsilon \geq 0$ may exist, since $\boldsymbol{\Upsilon}$ is an $N_\Sigma \times N_{\mathrm{r}}N_{\mathrm{t}}$ matrix with full row rank and $N_\Sigma \leq N_{\mathrm{r}}N_{\mathrm{t}}$. In other words, setting $\varepsilon = 0$ is equivalent to solving $\boldsymbol{w}_\Sigma = \boldsymbol{\Upsilon}\,\mathrm{vec}(\boldsymbol{W})$, which is an underdetermined system of equations when the sum co-array is redundant, i.e., $N_\Sigma < N_{\mathrm{r}}N_{\mathrm{t}}$. A typical choice for $\boldsymbol{W}$, which is always unique, is the *least squares* (LS) solution with minimum Frobenius norm $\|\boldsymbol{W}\|_{\mathrm{F}}$ (see, e.g., [184, p. 423])

$$\mathrm{vec}(\boldsymbol{W}) = \boldsymbol{\Upsilon}^\dagger \boldsymbol{w}_\Sigma. \tag{5.19}$$

By (3.19), the pseudoinverse of matrix $\boldsymbol{\Upsilon}$ is given by

$$\boldsymbol{\Upsilon}^\dagger = \boldsymbol{\Upsilon}^{\mathrm{T}}\left(\boldsymbol{\Upsilon}\boldsymbol{\Upsilon}^{\mathrm{T}}\right)^{-1} = \boldsymbol{\Upsilon}^{\mathrm{T}}\,\mathrm{diag}^{-1}(\boldsymbol{v}_\Sigma),$$

where $\boldsymbol{v}_\Sigma \in \mathbb{N}_+^{N_\Sigma}$ is the sum co-array multiplicity vector defined in (3.13). The LS solution distributes the desired co-array weights equally among the Tx-Rx sensor pairs contributing to the given co-array element. Eq. (5.19) is therefore equivalent to the *uniform weight assignment* scheme proposed by Kozick and Kassam [139, 141] and discussed in Publication II.

A drawback of the LS solution is that it does not generally yield a low rank $\boldsymbol{W}$. Consequently, unnecessarily many pulses or linearly independent Tx waveforms may be required for achieving the desired co-array weighting (or PSF)[2].

Optimization of beamforming weights

To address the shortcomings of the LS solution, Publication II proposes searching for the beamforming weights that minimize the number of component images Q, while ensuring that the realized co-array weighting is within a given tolerance of the desired weighting. Since $Q = \operatorname{rank}(\boldsymbol{W})$, this optimization problem can be written as

$$\underset{\boldsymbol{W} \in \mathbb{C}^{N_\mathrm{r} \times N_\mathrm{t}}}{\text{minimize}} \ \operatorname{rank}(\boldsymbol{W}) \quad \text{subject to} \quad \|\boldsymbol{w}_\Sigma - \boldsymbol{\Upsilon} \operatorname{vec}(\boldsymbol{W})\|_2^2 \leq \varepsilon_{\max}. \tag{P5.1}$$

Here $\boldsymbol{w}_\Sigma \in \mathbb{C}^V$ is a desired co-array weight vector, $\boldsymbol{\Upsilon} \in \{0,1\}^{N_\Sigma \times N_\mathrm{r} N_\mathrm{t}}$ the co-array selection matrix defined in (3.17), and $\varepsilon_{\max} \geq 0$ the maximum tolerated approximation error. Unfortunately, (P5.1) is a non-convex problem. However, the rank function may be replaced by the nuclear norm to yield a convex problem that typically yields a low-rank solution. The nuclear norm is the tightest convex relaxation to the rank function [70]. The resulting semidefinite program can be efficiently solved using standard numerical solvers [266].

Publication VIII presents another approach based on alternating minimization [118] and binary search (bisection). As summarized in Algorithm 1, this method fixes Q and iteratively attempts to solve

$$\underset{\boldsymbol{W}_\xi \in \mathbb{C}^{N_\xi \times Q}}{\text{minimize}} \ \left\| \boldsymbol{w}_\Sigma - \boldsymbol{\Upsilon} \operatorname{vec}\left(\boldsymbol{W}_\mathrm{r} \boldsymbol{W}_\mathrm{t}^\mathrm{T}\right) \right\|_2^2 \tag{P5.2}$$

by bisecting over Q to find the smallest value for which the objective function ε is smaller than or equal to the desired approximation error tolerance $\varepsilon_{\max}$. Although (P5.2) is a non-convex problem, it is biconvex in $\boldsymbol{W}_\mathrm{t}$ or $\boldsymbol{W}_\mathrm{r}$. This implies that a local minimum may be found efficiently using least squares, as summarized in Publication VIII, Algorithm 1.

If the PSF is not space-invariant, then $\boldsymbol{W}$ may need to be computed for multiple steering directions $\boldsymbol{u}$. This may be the case when sensors have directive gain patters or scatterers are located in the near field of the array. For details, see Section V-D of Publication VIII and [223].

Bounds on the number of component images

Publication VIII, Proposition 1 presents a lower bound on the number of component images Q required by the fully digital beamformer to achieve any co-array

[2] An exception is the case when the sum co-array is completely non-redundant, i.e. $N_\Sigma = N_\mathrm{t} N_\mathrm{r}$, which implies that (5.19) is the unique minimizer of (5.18).

Algorithm 1 Binary search (bisection) solving (P5.1)

procedure BINSEARCH($\boldsymbol{\Upsilon}, \boldsymbol{w}_\Sigma, \varepsilon_{\max}$)
  $\mathcal{Q} = \{1, 2, \ldots, \min(N_\mathrm{r}, N_\mathrm{t})\}$ ▷ set of feasible values of Q
  while $\mathcal{Q} \neq \emptyset$ **do** ▷ find smallest Q solving (P5.1)
    $Q \leftarrow \lfloor (\max \mathcal{Q} + \min \mathcal{Q})/2 \rfloor$ ▷ select midpoint of interval
    Solve (P5.2) to obtain $\boldsymbol{W}_\mathrm{t}$, $\boldsymbol{W}_\mathrm{r}$, and ε in (5.18)
    if $\varepsilon > \varepsilon_{\max}$ **then** ▷ infeasible solution
      $\mathcal{Q} \leftarrow \mathcal{Q} \setminus \{\min \mathcal{Q}, \ldots, Q\}$ ▷ discard smaller values
    else ▷ feasible solution
      $\mathcal{Q} \leftarrow \mathcal{Q} \setminus \{Q, \ldots, \max \mathcal{Q}\}$ ▷ discard larger values
      $\boldsymbol{W}_\mathrm{r}^\star \leftarrow \boldsymbol{W}_\mathrm{r}$ and $\boldsymbol{W}_\mathrm{t}^\star \leftarrow \boldsymbol{W}_\mathrm{t}$ ▷ update solution
  return $\boldsymbol{W}_\mathrm{r}^\star, \boldsymbol{W}_\mathrm{t}^\star$

weight vector in (5.12). The lower bound, which is based on a simple "equations versus unknowns" argument, is given by the inequality

$$Q \geq \frac{N_\mathrm{t} + N_\mathrm{r} - \sqrt{(N_\mathrm{t} + N_\mathrm{r})^2 - 4N_\Sigma}}{2}, \tag{5.20}$$

since $\boldsymbol{W}$ is a $N_\mathrm{r} \times N_\mathrm{t}$ matrix of rank Q, $\boldsymbol{\Upsilon}$ has full row rank, and $\boldsymbol{w}_\Sigma$ is a N_Σ-dimensional vector. Consequently, the following *necessary* condition holds: there *exists* a $\boldsymbol{W}$ that satisfies $\boldsymbol{w}_\Sigma = \boldsymbol{\Upsilon} \operatorname{vec}(\boldsymbol{W})$ for *any* $\boldsymbol{w}_\Sigma \in \mathbb{C}^{N_\Sigma}$ *only if*

- $Q \geq 1$, for the ULA with $N_\mathrm{t} = N_\mathrm{r} = N$ and $N_\Sigma = 2N - 1$
- $Q \geq 2$, for the URA (see Appendix A.6)
- $Q = \mathcal{O}(N)$, for any sparse array with $N_\mathrm{t} \propto N_\mathrm{r} \propto N$ and $N_\Sigma \propto N^2$
- $Q = \min(N_\mathrm{r}, N_\mathrm{t})$, for any nonredundant array with $N_\Sigma = N_\mathrm{t} N_\mathrm{r}$.

We conclude that the sparser the array, the larger the necessary number of component images. Specifically, order-wise optimal sparse arrays with N physical sensors have $\mathcal{O}(N^2)$ co-array elements and therefore require $\mathcal{O}(N)$ component images to achieve an arbitrary co-array weighting. We note that a similar relation also holds in DoA estimation. That is, N sensor sparse linear arrays, such as the Nested or Co-prime Array, require $\mathcal{O}(N)$ times more snapshots than the $\mathcal{O}(N^2)$ sensor ULA of equivalent aperture to achieve comparable MSE of the source direction estimates [289].

Eq. (5.20) also reveals that the URA may require a larger Q than the ULA. Note that (5.20) is only necessary for exactly achieving any co-array weight vector $\boldsymbol{w}_\Sigma$. Hence, some $\boldsymbol{w}_\Sigma$ may be achieved using a smaller Q. For example, if $\boldsymbol{w}_\Sigma$ is real-valued (but $\boldsymbol{W}$ is complex), then the lower bound of the URA reduces to $Q \geq 1$. Similarly, if a given $\boldsymbol{w}_\Sigma$ only needs to be attained approximately, then (5.20) does not necessarily hold.

The upper bound $Q \leq \min(N_\mathrm{r}, N_\mathrm{t})$ guaranteeing synthesis of any $\boldsymbol{w}_\Sigma$ may also be improved in some cases by considering array-specific synthetic aperture

schemes. These schemes allow adjusting the sum co-array weights independently by partitioning the Tx and Rx arrays into physical subarrays, such that the virtual subarrays (of the co-array) corresponding to different component images do not overlap. Tighter bounds may be achieved by allowing for overlap at the expense of a possibly more complicated weighting scheme. Fig. 5.5 illustrates weighting strategies for the ULA, URA, CNA and BA, whose simple structures make them amenable to this analysis. Hence, the following *sufficient* condition holds: there *exists* a $\boldsymbol{W}$ that satisfies $\boldsymbol{w}_\Sigma = \boldsymbol{\Upsilon}\,\mathrm{vec}(\boldsymbol{W})$ for *any* $\boldsymbol{w}_\Sigma \in \mathbb{C}^{N_\Sigma}$ *if*

$$Q \leq \begin{cases} 2, & \text{for the ULA} \\ 4, & \text{for the URA} \\ \frac{N+1}{2}, & \text{for the CNA} \\ \frac{(N+3)\rho+1}{\rho+1}, & \text{for the BA.} \end{cases} \tag{5.21}$$

Consequently, the ULA achieves any co-array weighting using $1 \leq Q \leq 2$ component images, whereas the URA needs $2 \leq Q \leq 4$. Sparse arrays, such as the CNA and BA, require $Q \propto N$, where N is the number of sensors. Eq. (5.21) follows directly from Fig. 5.5 using the fact that $\rho = (2L_y+1)/(2L_x+1)$ and $N = 2(L_x+L_y)$ in case of the BA, and $N_1 \leq (N+1)/4$ in case of the (minimum-redundancy) CNA by Publication IX, Eq. (16). Here $\rho \in (0,1]$ is the aspect ratio defined in (3.15).

Consider the number of component images Q relative to N as N approaches infinity. For the CNA, this asymptotic ratio is bounded as[3]

$$1 - \frac{\sqrt{3}}{2} \leq \lim_{N\to\infty} \frac{Q}{N} \leq \frac{1}{2}. \tag{5.22}$$

In practice, the CNA therefore achieves any co-array weighting when Q is between 13–50% of the value of N. Similarly, for the BA we have[4]

$$1 - \sqrt{1 - \left(\frac{\sqrt{\rho}}{\rho+1}\right)^2} \leq \lim_{N\to\infty} \frac{Q}{N} \leq \frac{\rho}{\rho+1}. \tag{5.23}$$

In the square array case, $\rho = 1$, (5.23) simplifies to the bound of the CNA in (5.22). In the non-square case, $\rho < 1$, the BA becomes increasingly redundant as $\rho \to 0$ (see Section 4.3.1), which implies that fewer component images are needed. For example, when $\rho = 1/2$, the BA achieves any co-array weighting when Q is between 12–33% of the value of N. The BA reduces to the ULA for $\rho = h_x^{-1}$, and Q becomes independent of N per (5.21).

5.3.2 Hybrid beamforming

Hybrid beamforming reduces the hardware costs and power consumption of the array by employing $1 < M_\xi < N_\xi$ Tx/Rx front ends along with an analog phase

[3]Specifically, the lower bound $Q \geq \left(1 - \frac{1}{2}\sqrt{3 - \frac{6N-7}{N^2}}\right)N$ follows by straightforward computation from (5.20) and Publication VIII, Theorem 3 and Corollary 4.

[4]The bound $Q \geq \left(1 - \sqrt{1 - \left(\frac{\sqrt{\rho}}{\rho+1}\frac{N+2}{N}\right)^2}\right)N$ follows from (5.20) and Section 4.3.1.

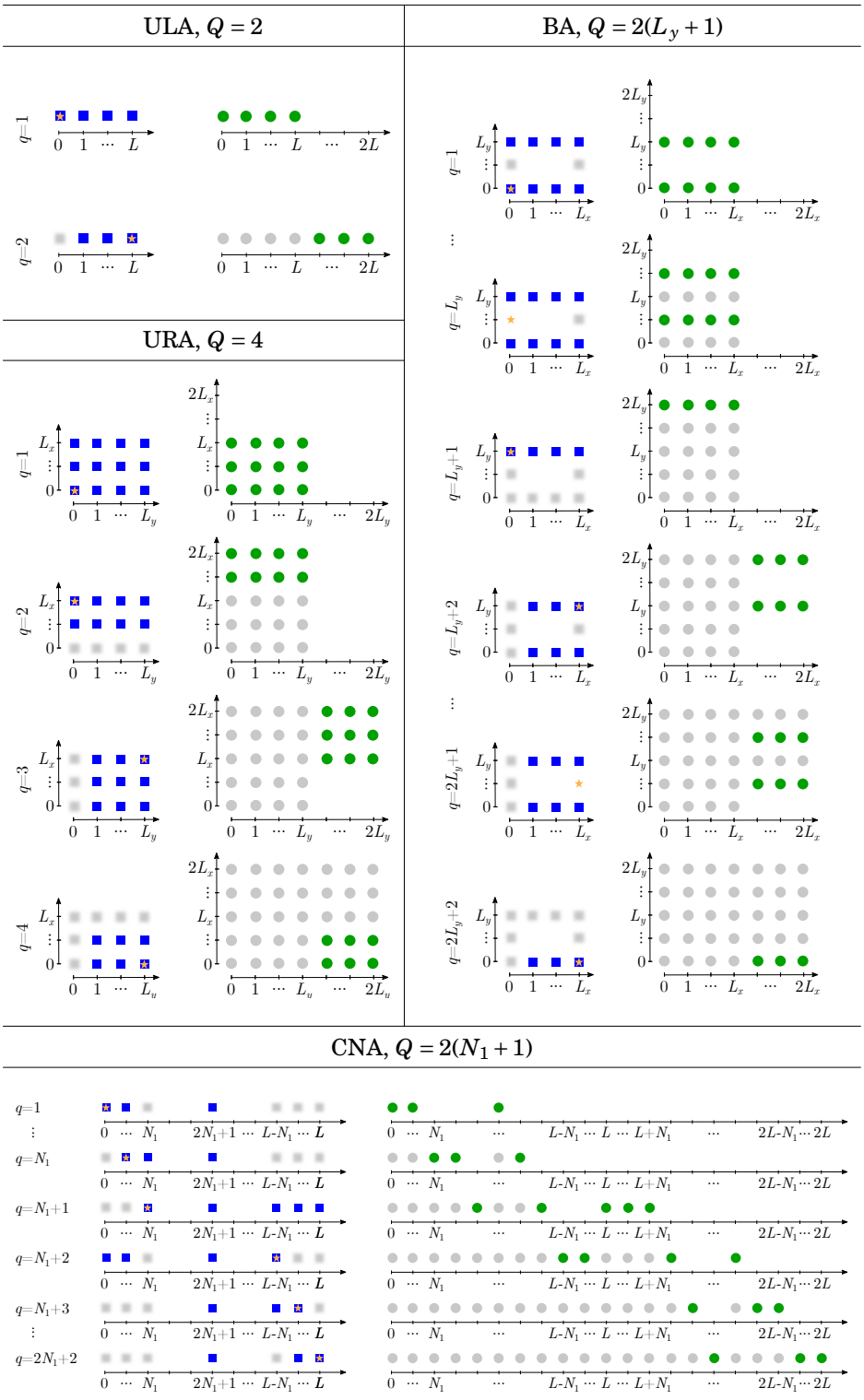

Figure 5.5. Synthetic aperture schemes for independently weighting the sum co-array elements. These schemes yield array-specific upper bounds on the number of component images required to achieve any co-array weighting exactly. The active physical and virtual sensors are marked by ★ (Tx), ■ (Rx), and ● (sum co-array). Inactive sensors are displayed in gray.

shifter network (see Fig. 3.2). These savings come at the expense of a loss in the flexibility provided by digital beamforming. In case of the hybrid beamformer, the co-array weight matrix in (5.4) becomes

$$\boldsymbol{W} = \sum_{q=1}^{Q} \boldsymbol{F}_{\mathrm{r},q} \boldsymbol{c}_{\mathrm{r},q} \boldsymbol{c}_{\mathrm{t},q}^{\mathrm{T}} \boldsymbol{F}_{\mathrm{t},q}^{\mathrm{T}} = \boldsymbol{F}_{\mathrm{r}} (\boldsymbol{I} \odot \boldsymbol{C}_{\mathrm{r}}) (\boldsymbol{I} \odot \boldsymbol{C}_{\mathrm{t}})^{\mathrm{T}} \boldsymbol{F}_{\mathrm{t}}^{\mathrm{T}}. \tag{5.24}$$

Here, the $N_\xi \times M_\xi Q$ matrix $\boldsymbol{F}_\xi \triangleq [\boldsymbol{F}_{\xi,1}, \boldsymbol{F}_{\xi,2}, \ldots, \boldsymbol{F}_{\xi,Q}]$ collects the $N_\xi \times M_\xi$ phase shift matrices $\boldsymbol{F}_{\xi,q} \in \mathscr{F}_\xi(B)$ of all component images, and $\mathscr{F}_\xi(B)$ denotes the set of phase shift matrices with B-bit phase quantization defined in (3.7). The $M_\xi \times Q$ matrix $\boldsymbol{C}_\xi \triangleq [\boldsymbol{c}_{\xi,1}, \boldsymbol{c}_{\xi,2}, \ldots, \boldsymbol{c}_{\xi,Q}]$ contains the respective digital beamforming vectors $\boldsymbol{c}_\xi \in \mathbb{C}^{M_\xi}$.

The optimal analog beamforming weights can be found similarly to the digital case by iteratively solving the following optimization problem with respect to the analog and digital Tx/Rx beamforming matrices $\boldsymbol{F}_\xi$ and $\boldsymbol{C}_\xi$:[5]

$$\begin{aligned} \underset{\boldsymbol{F}_\xi \in \mathbb{C}^{N_\xi \times M_\xi Q}; \boldsymbol{C}_\xi \in \mathbb{C}^{M_\xi \times Q}}{\text{minimize}} \quad & \left\| \boldsymbol{w}_\Sigma - \boldsymbol{\Upsilon} \left(\boldsymbol{F}_{\mathrm{t}} (\boldsymbol{I} \odot \boldsymbol{C}_{\mathrm{t}}) \odot \boldsymbol{F}_{\mathrm{r}} (\boldsymbol{I} \odot \boldsymbol{C}_{\mathrm{r}}) \right) \mathbf{1} \right\|_2^2 \\ \text{subject to} \quad & \boldsymbol{F}_\xi \in \mathscr{F}_\xi(B). \end{aligned} \tag{P5.3}$$

Publication VIII, Algorithm 3 proposes a greedy search method for finding an approximate solution to (P5.3) for any number of bits B used to quantize the phase shifters. The algorithm sequentially attempts to find the best single component hybrid beamforming weights whose Kronecker product is aligned with the residual between the desired and realized co-array weight vector. The optimal weights are found at each iteration by projecting the fully digital beamforming weights to the set of feasible hybrid beamforming weights (cf. Publication VIII, Algorithm 2). The fully digital weights can be computed using Algorithm 1 in Publication VIII.

Publication VIII, Theorem 1 shows that if $B \to \infty$, then the number of component images Q is upper bounded by $\min(N_{\mathrm{r}}, N_{\mathrm{t}})$, similarly to the fully digital case. Remarkably, the hybrid beamformer only requires two Tx and Rx front ends to synthesize any PSF achieved by the fully digital beamformer. Publication VIII, Theorem 2 further demonstrates that if $B \geq 1$ and $M_\xi \geq 2$, then $Q \leq N_{\mathrm{r}} N_{\mathrm{t}}$. This bound can actually be tightened to $Q \leq N_\Sigma \leq N_{\mathrm{r}} N_{\mathrm{t}}$, as proven in the following new result, included in this thesis only.

Proposition 5.1 (Hybrid beamformer)**.** *Let $M_\xi = 2$ and $B = 1$. Any $\boldsymbol{w}_\Sigma \in \mathbb{C}^{N_\Sigma}$ may be written as $\boldsymbol{w}_\Sigma = \boldsymbol{\Upsilon} \operatorname{vec}(\boldsymbol{W})$, where $\boldsymbol{\Upsilon}$ is defined in* (3.17)*, and $\boldsymbol{W} \in \mathbb{C}^{N_{\mathrm{r}} \times N_{\mathrm{t}}}$ factorizes as in* (5.24) *with $Q = N_\Sigma$. For example, $\boldsymbol{F}_{\xi,q} \in \mathscr{F}_\xi(1)$ following* (3.7) *and $\boldsymbol{c}_{\xi,q} \in \mathbb{C}^2$ may be selected as*

$$\boldsymbol{F}_{\xi,q} = \begin{bmatrix} \mathbf{1} & 2\boldsymbol{e}_{n_\xi} - \mathbf{1} \end{bmatrix} \quad \text{and} \quad \boldsymbol{c}_{\xi,q} = \frac{\sqrt{\left[\boldsymbol{w}_\Sigma\right]_q}}{2} \mathbf{1}, \tag{5.25}$$

where any choice of indices $n_\xi \in \{1 : N_\xi\}$ satisfying $\boldsymbol{d}_{\mathrm{t},n_{\mathrm{t}}} + \boldsymbol{d}_{\mathrm{r},n_{\mathrm{r}}} = \boldsymbol{d}_{\Sigma,q}$ is valid.

[5] Modifications to Algorithm 1: on line 2 set $\max \mathscr{Q} = N_\Sigma$ if $B < \infty$ (see PVIII, Theorem 1 and Proposition 5.1 of this thesis), and on line 5 solve (P5.3).

Proof. By (5.25), each component image contributes to exactly one entry in matrix $\boldsymbol{W}$. Furthermore, each non-zero entry of $\boldsymbol{W}$ affects only a single entry of $\boldsymbol{w}_\Sigma$, since the rows of $\boldsymbol{\Upsilon}$ are orthogonal. In particular, $\boldsymbol{F}_{\xi,q}\boldsymbol{c}_{\xi,q} = \sqrt{\left[\boldsymbol{w}_\Sigma\right]_q}\boldsymbol{e}_{n_\xi}$, where $\boldsymbol{e}_{n_\xi} \in \{0,1\}^{N_\xi}$ is the standard unit vector of dimension N_ξ with a unit entry at index $n_\xi \in \{1,2,\ldots,N_\xi\}$. Note that n_ξ is a function of q. Hence, we have

$$\operatorname{vec}(\boldsymbol{W}) = \sum_{q=1}^{N_\Sigma} \operatorname{vec}\left(\boldsymbol{F}_{\mathrm{r},q}\boldsymbol{c}_{\mathrm{r},q}\boldsymbol{c}_{\mathrm{t},q}^{\mathrm{T}}\boldsymbol{F}_{\mathrm{t},q}^{\mathrm{T}}\right) = \sum_{q=1}^{N_\Sigma} \left[\boldsymbol{w}_\Sigma\right]_q \left(\boldsymbol{e}_{n_\mathrm{t}(q)} \otimes \boldsymbol{e}_{n_\mathrm{r}(q)}\right).$$

If $\boldsymbol{d}_{\mathrm{t},n_\mathrm{t}(q)} + \boldsymbol{d}_{\mathrm{r},n_\mathrm{r}(q)} = \boldsymbol{d}_{\Sigma,q}$, then $\boldsymbol{\Upsilon}(\boldsymbol{e}_{n_\mathrm{t}} \otimes \boldsymbol{e}_{n_\mathrm{r}}) = \boldsymbol{e}_q$ holds by definition, where $\boldsymbol{e}_q$ is an N_Σ-dimensional standard unit vector. Hence, $\boldsymbol{w}_\Sigma = \boldsymbol{\Upsilon}\operatorname{vec}(\boldsymbol{W})$ follows. □

The bound $Q \leq N_\Sigma$ implied by Proposition 5.1 holds for any $B \geq 1$, since $\mathscr{F}_\xi(1) \subseteq \mathscr{F}_\xi(B)$ by (3.7). It is also valid for any $M_\xi \geq 2$, since zeros and arbitrary columns can be appended to $\boldsymbol{c}_{\xi,q}$ and $\boldsymbol{F}_{\xi,q}$, respectively. Note that Q satisfies the lower bound in (5.20) also in the hybrid case.

5.3.3 Fully analog beamforming

In a fully analog beamforming architecture, each sensor is connected to the same Tx or Rx front end through a phase shifter network. This actually corresponds to the phased array architecture in (3.9), since a single Tx front end implies a single transmit waveform appropriately delayed at each sensor, i.e., $M_\mathrm{t} = 1 \implies N_s = 1$. By (5.2), the Tx/Rx beamforming weight reduces to $\boldsymbol{w}_\xi = \boldsymbol{f}_\xi c_\xi$, where $\boldsymbol{f}_\xi \in \mathscr{F}_\xi(B)$ is the N_ξ-dimensional analog phase shift vector with B-bit phase quantization and $c_\xi \in \mathbb{C}$ is a digital gain. Hence, the co-array weight matrix can be written as

$$\boldsymbol{W} = \sum_{q=1}^{Q} c_{\mathrm{r},q}c_{\mathrm{t},q}\boldsymbol{f}_{\mathrm{r},q}\boldsymbol{f}_{\mathrm{t},q}^{\mathrm{T}} = \boldsymbol{F}_\mathrm{r}\operatorname{diag}(\boldsymbol{c})\boldsymbol{F}_\mathrm{t}^{\mathrm{T}},$$

where the analog and digital beamforming weights of all component images are contained in the $N_\xi \times Q$ phase shift matrix $\boldsymbol{F}_\xi$ and digital beamforming weight vector $\boldsymbol{c} \triangleq [c_{\mathrm{t},1}c_{\mathrm{r},1}, c_{\mathrm{t},2}c_{\mathrm{r},2}, \ldots, c_{\mathrm{t},Q}c_{\mathrm{r},Q}]^{\mathrm{T}}$, respectively. Assuming w.l.o.g. that $|c_{\mathrm{t},q}| \leq 1$, we set $c_{\mathrm{t},q} = 1\ \forall q$ to maximize the Tx combining gain.

The optimal Q-component image beamforming weights are then found by solving the following optimization problem[6]

$$\underset{\boldsymbol{F}_\xi \in \mathbb{C}^{N_\xi \times Q}; \boldsymbol{c} \in \mathbb{C}^Q}{\text{minimize}} \ \left\|\boldsymbol{w}_\Sigma - \boldsymbol{\Upsilon}(\boldsymbol{F}_\mathrm{t} \odot \boldsymbol{F}_\mathrm{r})\boldsymbol{c}\right\|_2^2 \quad \text{subject to} \quad \boldsymbol{F}_\xi \in \mathscr{F}_\xi(B). \tag{P5.4}$$

Publication VI, Algorithm 1 presents a gradient descent algorithm for finding an approximate solution to the non-convex optimization problem (P5.4) in the case of infinite precision phase shifters, i.e., $B \to \infty$. This approach leverages the fact that the objective function is a continuous and differentiable with respect to

[6]Modifications to Algorithm 1: on line 2 set $\max \mathscr{Q} = 4\max(N_\mathrm{r}, N_\mathrm{t})$ if $B \to \infty$, otherwise $\max \mathscr{Q} = 4N_\Sigma$ (see PVIII, Theorem 3 and Lemma 3). On line 5, solve (P5.4).

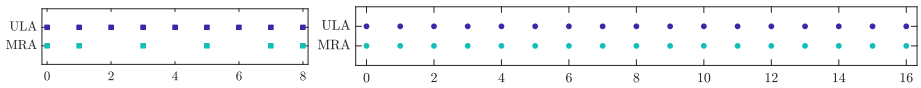

(a) Physical array **(b)** Sum co-array

Figure 5.6. Physical array and sum co-array of linear configurations with shared Tx and Rx sensors. The ULA has $N = 9$ physical sensors, whereas the MRA has $N = 6$. The sum co-arrays are contiguous with $N_\Sigma = 17$ virtual elements.

the Tx/Rx phase matrix $\boldsymbol{\Phi}_\xi \in \mathbb{R}^{N_\xi \times Q}$ by (3.7), and that the optimal digital gain vector is given by the least squares solution $\boldsymbol{c} = (\boldsymbol{\Upsilon}(\boldsymbol{F}_\mathrm{t} \odot \boldsymbol{F}_\mathrm{r}))^\dagger \boldsymbol{w}_\Sigma$. In the case of finite precision phase shifters, i.e., $B < \infty$, the greedy search of Publication VIII, Algorithm 4 can be applied similarly to the hybrid case discussed in Section 5.3.2.

Each component image of the fully analog beamformer corresponds to a separate transmission and reception due to the lack of waveform diversity. Publication VIII, Theorems 3 and 4 show that the number of component images Q is upper bounded by $4\min(N_\mathrm{r}, N_\mathrm{t})$ when $B \to \infty$, and $4N_\mathrm{r}N_\mathrm{t}$ when $B \geq 1$. The latter bound can be tightened to $Q \leq 4N_\Sigma$ by application of Proposition 5.1 and Publication VIII, Lemma 3.

5.3.4 Numerical examples

We illustrate the concepts presented in this section by a simple example using a uniform and sparse linear array. Further numerical results can be found in Publication II and VIII.

Array configuration and sum co-array

Consider the two linear arrays with fully overlapping Tx and Rx sensors depicted in Fig. 5.6. The ULA has $N = 9$ and the MRA $N = 6$ physical sensors. Both arrays have an aperture of $L = 8$ and a contiguous sum co-array with $H_\Sigma = 17$ virtual elements. Fig. 5.7 shows the beamforming weights and PSFs of both the physical array and sum co-array assuming unit Tx and Rx beamforming weights and a unit inter-sensor spacing of $\delta = \lambda/2$. The resulting sum co-array weight function indicates the multiplicity of each virtual element. The sum co-array weight function is the convolution of the Tx and Rx weight functions. Hence, by the Fourier transform relation, the effective PSF is the product of the Tx and Rx PSFs.

PSF synthesis using image addition

Finding the Tx and Rx beamforming weights achieving a desired co-array weighting requires solving the inverse problem (P5.1). In particular, the solution to (P5.1) yields the minimum number of physical Tx and Rx weighting pairs given a fully digital beamforming architecture.

For example, let the desired co-array beamforming weight function be a rectangular window, i.e., $\boldsymbol{w}_\Sigma = \mathbf{1}_{17}$. This yields an effective PSF with a narrow main lobe and a peak side lobe level of approximately -13 dB. Fig. 5.8 shows the

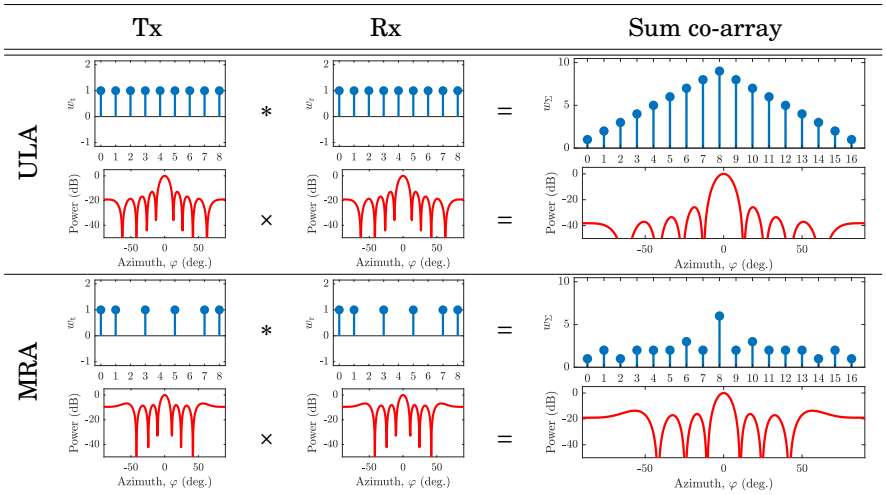

Figure 5.7. Beamforming weights (blue) and respective beampatterns (red), assuming unit Tx and Rx weights. The co-array weight function, corresponding to the multiplicities of the virtual elements per (3.13), is the convolution of the Tx and Rx weight functions. The effective beampattern is the Fourier transform pair, given by the product of the Tx and Rx beampatterns.

beamforming weights and PSFs of the ULA and MRA found using Algorithm 1 in Section 5.3.1 combined with Publication VIII, Algorithm 1. The ULA requires $Q = 1$ and the MRA $Q = 2$ component images when the approximation error tolerance is set to $\varepsilon_{\max} = 10^{-8}/\|\boldsymbol{w}_\Sigma\|_2^2$. If $\varepsilon_{\max} = 0$, then the MRA must satisfy $Q \geq 2$ by (5.20) and $Q \leq 4$ by (5.21), since the MRA actually coincides with the CNA for $N = 6$ sensors.

Effect of hybrid and fully analog architectures

In case of a non-digital beamforming architecture, more component images may be needed to achieve the desired PSF, even in the case of the ULA. Fig. 5.9 illustrates the fully digital, hybrid, and fully analog beamforming architectures assuming the number of Tx and Rx front ends equal M. Fig. 5.10 shows the PSFs achieved by Publication VIII, Algorithms 1 and 3 for different values of Q. The phase shifters of the hybrid and fully analog beamformers use $B = 3$ bit phase quantization. The coarse phase quantization and low number of front ends M can be offset by increasing the number of component images Q.

By Publication VIII, Theorem 1, the hybrid beamformer with $M \geq 2$ and no phase quantization ($B \to \infty$) achieves the PSF of the fully beamformer exactly using the same number of component images, i.e., $Q = 1$ in case of the ULA and $Q = 2$ in case of the MRA. If $B < \infty$, then Proposition 5.1 guarantees equivalence between the hybrid and fully digital beamformer provided $Q = N_\Sigma = 17$. In practice, Fig. 5.10 demonstrates that already $Q = 2$ or 4 yields the desired PSF with negligible approximation error in the hybrid case with $M \in \{2, 3\}$.

Similar conclusions hold for the fully analog case, albeit for a larger Q. By Publication VIII, Theorem 3, if $B \to \infty$, the PSF of the fully digital beamformer

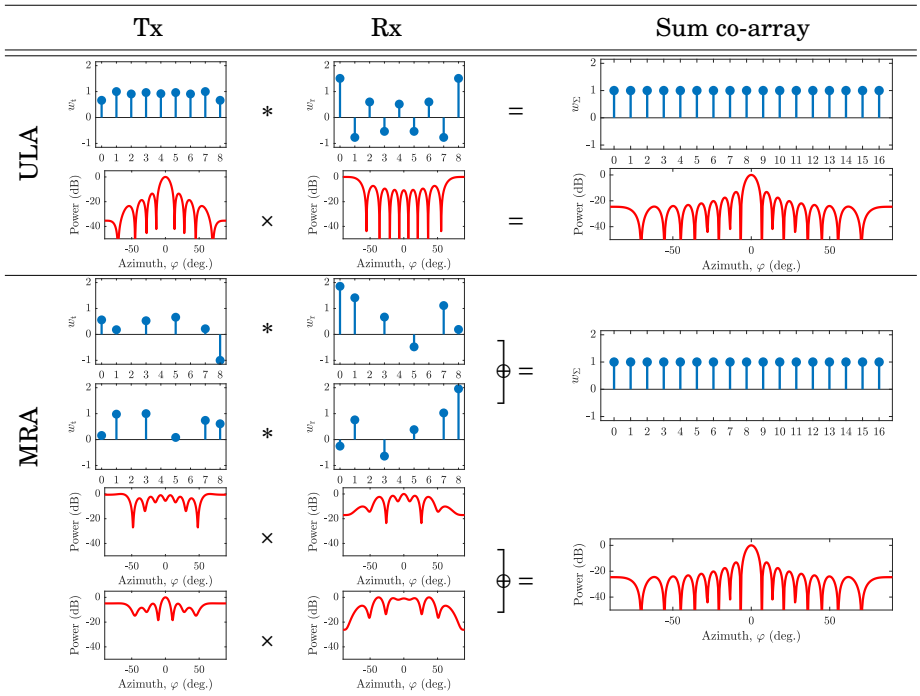

Figure 5.8. Beamforming weights (blue) and respective beampatterns (red), assuming a rectangular sum co-array weight function. The MRA requires two component images to achieve the desired co-array weighting, due to having fewer physical sensors than the ULA.

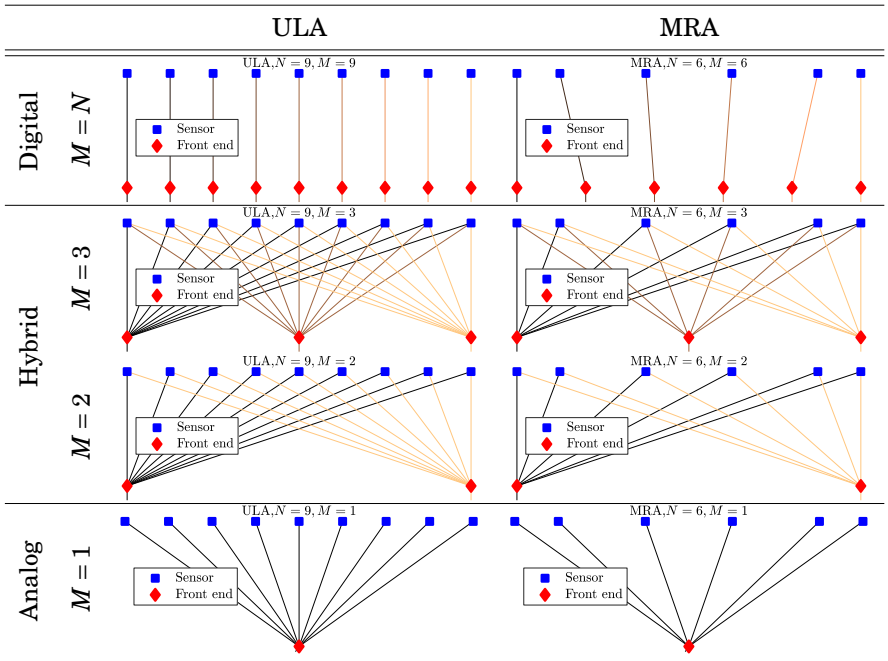

Figure 5.9. Fully digital, hybrid, and fully analog beamforming architectures. In the hybrid and analog cases, each front end and sensor is connected via a phase shifter with adjustable phase.

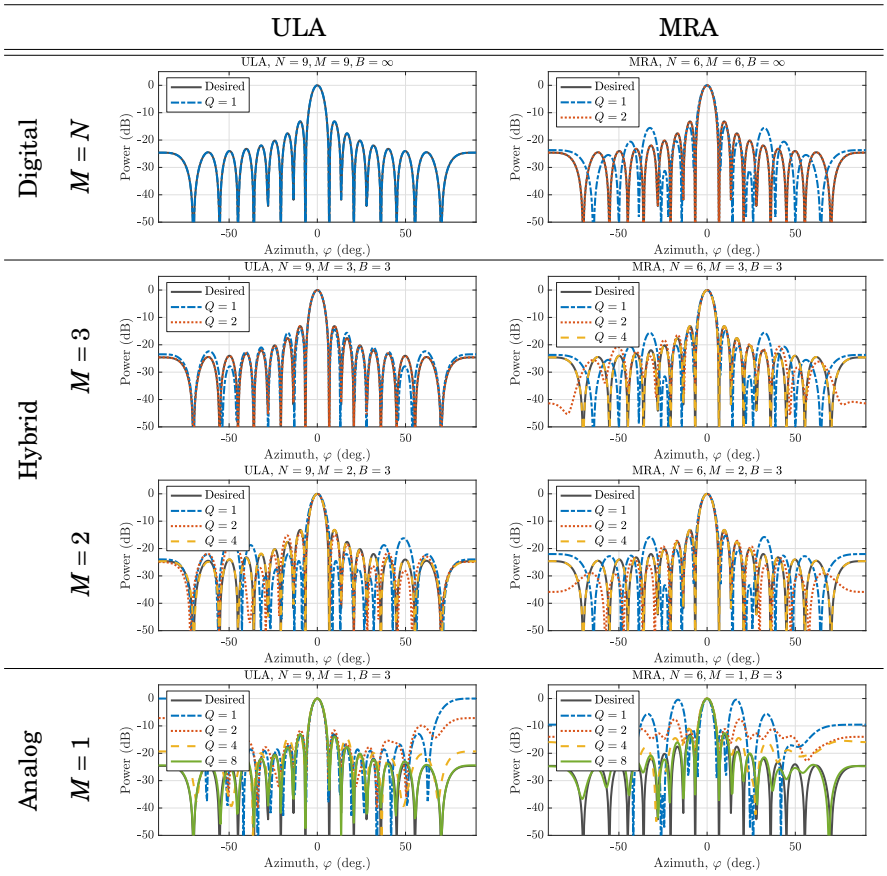

Figure 5.10. PSFs of fully digital, hybrid, and fully analog beamformers. A reduction in the number of Tx/Rx front ends M can be offset by increasing the number of component images Q. In this example, Q =–2 suffices in the fully digital case, whereas Q = 4–8 may be needed in the hybrid and fully analog cases, respectively. The ULA requires fewer component images than the MRA due to having has more physical sensors. The phase shifters of the hybrid and analog architectures use B = 3 bit phase quantization.

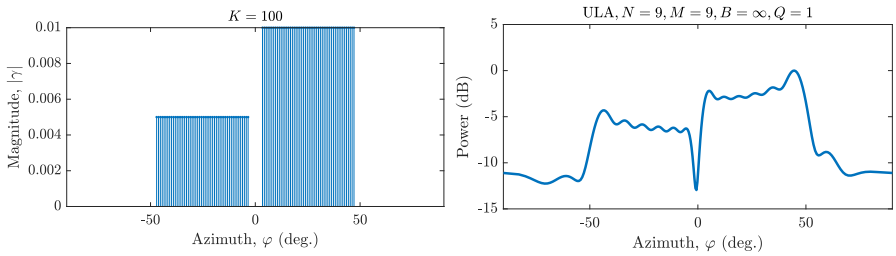

(a) Scatterer distribution

(b) Image

Figure 5.11. Scattering scene and image obtained by the fully digital architectures. The ULA requires $Q = 1$ component image and MRA $Q = 2$ components.

is achieved by quadrupling the number of component images, i.e., by setting $Q = 4$ in case of the ULA and $Q = 8$ in case of the MRA. For finite B, $Q = 4N_\Sigma = 68$ is theoretically sufficient by Proposition 5.1 and Publication VIII, Lemma 3. Fig. 5.10 illustrates that a much smaller value, e.g., $Q = 8$, is enough to approximate the desired PSF in practice.

Note that the PSF ceases to be space-invariant (cf. Section 5.1.3) when arbitrary phase shifts cannot be applied to steer the array. For example, when $B = 3$, only $2^3 = 8$ distinct phase shifts are achieved. The Tx and Rx beamforming weights therefore need to be recomputed for most steering directions, when employing coarse quantization. This requires solving (P5.3) in the hybrid case, or (P5.4) in the fully analog case.

Imaging example

For our final example we consider an imaging simulation. We approximate two continuous reflectors spaced apart by roughly one beamwidth[7] using $K = 100$ point scatterers with magnitudes depicted in Fig. 5.11a. The phases are set to zero for all scatterers, i.e., $\measuredangle \gamma_k = 0 \ \forall \ k$. For simplicity, we limit our discussion to the fully digital beamforming architecture and the hybrid beamformer with $M = 2$ Tx/Rx front ends and $B = 3$ phase shift bits.

Fig. 5.11b shows the image produced by either of the fully digital arrays, i.e., the ULA using $Q = 1$ or the MRA using $Q = 2$ component images. The general shape of the scatterers is resolved, along with the gap between them. Note that it is less obvious how to apply, e.g., MUSIC or compressed sensing in this scenario, since the number of point scatterers is much greater than the number of sum co-array elements, that is, $K = 100 \gg N_\Sigma = 17$.

Fig. 5.12 shows the image produced by the hybrid beamforming architectures for $Q = 1$ and $Q = 4$ component images. In the single image case, the low number of phase shifts bits results in poor image quality and a loss of resolution, especially in the case of the MRA. This is due to the fact that the PSF is not spatially invariant, i.e., the Tx/Rx beamforming weights have to be recomputed

[7] By [198, Eq. (20.10.7)], the full width half maximum at boresight is approximately $\frac{0.886\lambda}{N_\Sigma \delta}$, which for $N_\Sigma = 17$ and $\delta = \lambda/2$ evaluates to roughly 6°.

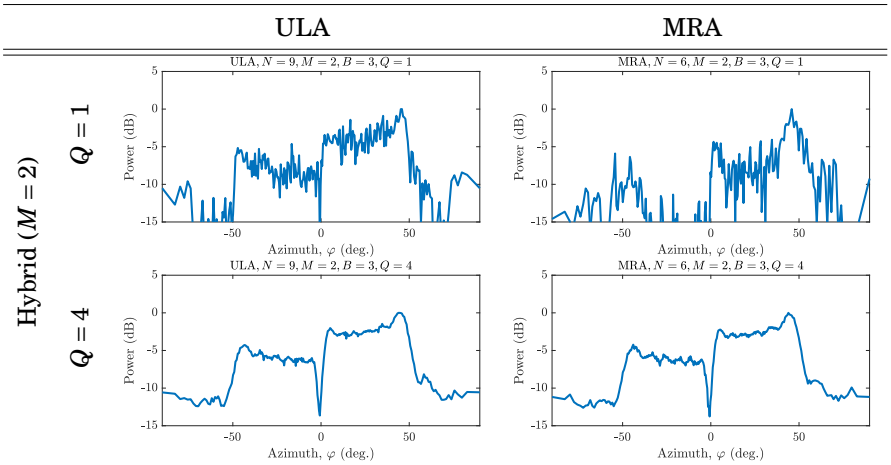

Figure 5.12. Images obtained by hybrid beamforming architectures. The steering quantization noise due to the low number of phase shift bits is suppressed by using several component images.

for each steering direction. Increasing the number of component images to $Q = 4$ suppresses these artifacts, and the resulting image closely resemble that in Fig. 5.11b obtained by the fully digital architecture.

Fig. 5.13 shows the images produced by the fully digital and hybrid (phased) arrays in the presence of receiver noise with variance $\sigma^2 = 10^{-3}$. The ULA achieves a higher SNR due to having 3/2 times the number of sensors of the MRA. In particular, by (5.13), the maximum SNR—assuming a single component image and no apodization—is $30\log\frac{3}{2} \approx 5.3$ dB higher for the ULA. The true SNR difference is $10\log\frac{39.70}{29.61} \approx 1.3$ dB, which is obtained by evaluating (5.13) for the realized component image beamforming weights of the fully digital ULA with $Q = 1$ and MRA with $Q = 2$ assuming a single boresight scatterer. In the case of the hybrid beamformers with $Q = 4$, the SNR difference is $10\log\frac{53.88}{36.71} \approx 1.7$ dB in favor of the ULA. We note that the beamforming weights are neither orthogonal nor fully correlated between component images. Specifically, the inter-image cross-correlation is $\frac{|\boldsymbol{w}_{\xi,1}^{\mathrm{H}}\boldsymbol{w}_{\xi,2}|}{\|\boldsymbol{w}_{\xi,1}\|_2\|\boldsymbol{w}_{\xi,2}\|_2} < 0.23$ for both the Tx and Rx beamforming weights of the fully digital MRA. In the hybrid case, the maximum inter-image cross-correlation is $\max_{q\neq l}\frac{|\boldsymbol{w}_{\xi,q}^{\mathrm{H}}\boldsymbol{w}_{\xi,l}|}{\|\boldsymbol{w}_{\xi,q}\|_2\|\boldsymbol{w}_{\xi,l}\|_2} < 0.71$ for both the Tx and Rx beamforming weights of the MRA, and < 0.31 for the ULA. Due to the larger number of component images, the hybrid beamformer improves the SNR compared to the fully digital beamformer by $10\log\frac{53.88}{39.70} \approx 1.3$ dB and $10\log\frac{36.71}{29.61} \approx 0.9$ dB in case of the ULA and MRA, respectively.

5.4 Discussion

A central goal of this chapter was to characterize the trade-off between the number of component images and image quality in sparse array imaging. The

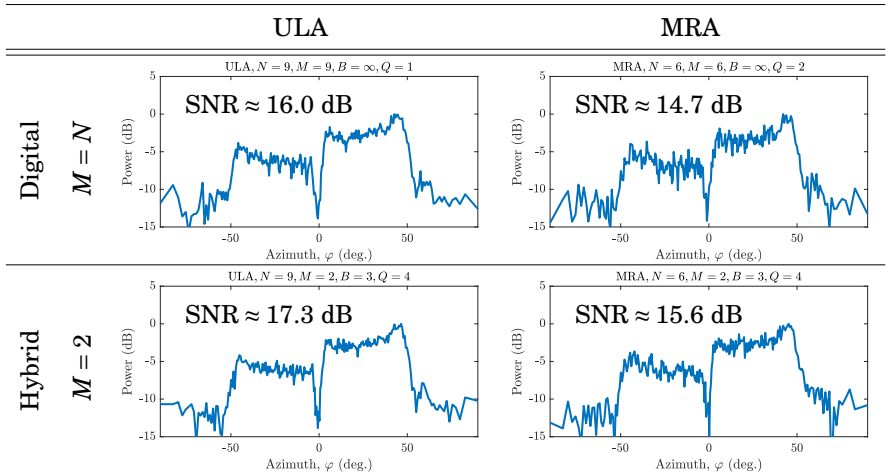

Figure 5.13. Images with receiver noise. The ULA achieves a higher SNR than the MRA due to having more sensors. Image addition only marginally improves the SNR since the beamforming weights are approximately orthogonal between component images.

presented results yield a quantitative description of the relation among the number of component images and the SNR, array sparsity, beamforming architecture, waveform diversity, or the number of pulses. Note that the considered beamformer designs essentially leverage redundancy to optimize the beamforming weights. Even the sum co-array of the MRA generally has redundant virtual elements, which implies the existence of multiple choices of beamforming weights yielding a desired effective Tx-Rx beampattern. Minimizing the number of component images is advantageous not only for reducing image acquisition time, but also for simplifying the array architecture and improving the Tx combining gain. Recall that a MIMO array obtains as many component images Q per pulse as the number of employed linearly independent Tx waveforms N_s. Consequently, if a desired point spread function can be achieved (approximately) using a smaller Q, then N_s can also be reduced. This implies both fewer necessary front ends at the transmitter and matched filters at the receiver. The Tx combining gain is also increased because some of the Tx sensor outputs are (fully) correlated.

We conclude the chapter by briefly considering image addition in the case of incoherent scatterers or emitters. Appendix A.7 extends the discussion on image addition by examining related concepts in imaging applications and beyond.

Incoherent image addition

A careful examination of the assumptions listed in Section 3.1 reveals that the coherent scatterer assumption (A2) is not invoked until this chapter. In particular, (A2) is not necessary for deriving the signal model in (3.5). Rather, it is needed for coherent ("complex") image addition to work properly when component images correspond to different transmissions. A loss of scatterer coherence between pulses can result in degraded image quality [112]. If the scattering coefficients fluctuate significantly between pulses, then incoherent ("intensity")

image addition [111] may have to be employed instead. This requires computing second-order statistics of the received data, i.e., the received signal covariance matrix. If the scatterers are mutually uncorrelated, then the difference-sum co-array is a more relevant virtual array model than the sum co-array, as pointed out in Appendix A.2.2.

Naturally, image addition can also be applied to passive sensing and the difference co-array [111, 9, 62]. Indeed, the nonlinear signal power-based beamformer discussed in Section 2.3.1 is a prime example of incoherent image addition. However, differently from the PA case in active sensing, and similarly to the O-MIMO case, the number of component images Q is less critical in passive sensing. Specifically, Q does not affect the acquisition time of the image. Imaging time is rather determined the number of snapshots needed to estimate the data covariance matrix. Recall from Section 2.3 that at least as many independent snapshots as physical sensors are required for the sample covariance matrix to have full rank. If the beamforming architecture is hybrid or fully analog, then the number of snapshots may need to be increased to compensate for the reduction in the number of Rx front ends.

6. Conclusions

A variety of multisensor system applications, such as volumetric imaging, multi-target tracking, as well as mmWave and beyond radar/communications, impose increasingly stricter demands on the performance of sensor arrays. In particular, achieving a high spatial resolution requires an array with a large electrical aperture. This entails a large number of physical sensors and expensive RF-IF front ends when conventional uniform array designs are employed. However, sparse arrays leveraging the virtual co-array model can drastically lower the number of sensors and front ends, while retaining many of the advantages of an equivalent aperture uniform array.

This thesis presented novel results in sparse array design and processing for active sensing. Specifically, Chapter 4 considered sum co-array-based array designs of the minimum-redundancy type. These array configurations achieve a contiguous sum co-array of desired size using as few physical sensors as possible. A contiguous sum co-array has several advantages. For a given physical array size, it provides a maximum number of degrees of freedom (DoFs) in imaging and direction finding applications. Many algorithms developed for uniform arrays can also be directly applied to a contiguous co-array.

Chapter 5 introduced a general framework for linear imaging using low-complexity beamforming architectures and few component images. Beamforming provides a simple and computationally inexpensive approach to active sensing. Hybrid and analog beamforming architectures—either together with, or as an alternative to sparse arrays—further reduce the number of expensive Tx/Rx front ends and DACs/ADCs. This may come at the cost of an increase in the number of component images required to achieve a desired image quality. Minimizing the number of component images is therefore necessary to reduce the image acquisition time or the number of linearly independent transmit waveforms and the related hardware requirements. Next, we summarize the main results of the thesis and outline directions for future work.

6.1 Sparse arrays with a contiguous sum co-array

Chapter 4 proposed a general definition of redundancy that takes into account different degrees of overlap between the transmitting and receiving arrays. Based on this definition, we formulated the Minimum-Redundancy Array (MRA) optimization problem in the case of non-overlapping, partially overlapping, and fully overlapping Tx and Rx arrays. We computed several novel solutions to this problem. In particular, we focused on planar MRAs where each sensor is a transceiver contained in an $L_x + 1$ by $L_y + 1$ rectangular grid. Here, L_x and L_y denote the normalized side lengths of the rectangle in units of the smallest inter-sensor spacing, which is typically half a wavelength. We found all MRAs for $1 \leq L_y \leq L_x \leq 13$, and established that the number of sensors N in square MRAs follows the simple relation $N = 4L$ for at least $L \leq 23$, where $L = L_x = L_y$ is the side length of the square.

We derived several scalable array configurations that are both easy to generate and achieve a low redundancy for any number of sensors, aperture, or aspect ratio. For instance, the novel Concentric Rectangular Array (CRA) has several desirable properties when its side lengths are equal ($L = L_x = L_y$). Specifically, the square CRA achieves the same number of sensors as the MRA for at least all even $6 \leq L \leq 22$, similarly to the well-known Boundary Array (BA), which has $N = 4L$ sensors for any $L \geq 1$. The square CRA is also the MRA with the fewest closely spaced sensors for at least $L \in \{6, 8, 10, 12\}$. In the strictly rectangular case ($L_y \neq L_x$), we showed that the Restricted Short Bars Array (R-SBA) achieves a low asymptotic redundancy for practically any aspect ratio. In the linear array case ($L_y = 0$), we presented a general framework for symmetric arrays, which allow constructing arrays with contiguous sum and difference co-arrays using any configuration with a contiguous difference co-array. The Concatenated Nested Array (CNA) and Kløve Array (KA) are examples of such symmetric arrays. The KA has the lowest asymptotic redundancy of any currently known scalable array with a contiguous sum co-array. It has 0–27% more sensors than the MRA of equivalent aperture, when the aperture approaches infinity.

New contributions included in this thesis only are the definition of redundancy for diverse Tx/Rx array overlap in (4.2), the non-overlapping MRA in Proposition 4.1, and the aspect ratio insensitive R-SBA in (4.8).

The presented novel sparse array configurations provide both theoretically important bounds on the achievable redundancy, as well as practical array designs relevant for active and passive sensing.

6.2 Image addition using few component images

Chapter 5 studied active coherent imaging using image addition. Image addition allows synthesizing arbitrary point spread functions (PSFs) supported on the sum co-array by linearly combining multiple component images corresponding

to different Tx and Rx beamforming weights. The number of component images Q depends mainly on the desired PSF and the sparsity of the array. Specifically, we showed that any N sensor sparse array with $\mathcal{O}(N^2)$ sum co-array elements requires $\mathcal{O}(N)$ component images to achieve an arbitrary feasible PSF. For example, the CNA and square BA satisfy $0.13N < Q \leq 0.5N$ for large N. In contrast, the Uniform Linear Array (ULA) satisfies $1 \leq Q \leq 2$ and the Uniform Rectangular Array (URA) $2 \leq Q \leq 4$, regardless of N.

We furthermore showed that the signal-to-noise ratio (SNR) of image addition primarily depends on the cross-correlation between the beamforming vectors corresponding to different component images. Image addition does not significantly affect the SNR compared to the single component image case, since the beamforming weights are typically approximately orthogonal between component images. However, using multiple component images facilitates a wider range of PSFs, which may suppress interference from unwanted scatterers. The number of component images can at most equal the product of the number of pulses and linearly independent transmit waveforms. Hence, waveform diversity can reduce image acquisition time in case multiple component images are used.

Finally, we showed that redundancy provides DoFs in selecting the physical beamforming weights producing a desired co-array weight function. We leveraged this fact by formulating an optimization problem for minimizing the number of component images, subject to the realized PSF being within a predetermined tolerance of the desired PSF. We proposed numerical methods for approximately solving this problem in the case of fully digital, hybrid, and fully analog beamforming architectures. We demonstrated that hybrid and fully analog beamformers reduce the number of expensive Tx/Rx front ends at the expense of a possible increase in the number of component images. For example, any hybrid beamformer with at least two Tx and Rx front ends can achieve any PSF of a fully digital beamformer using an equivalent number of component images Q, provided that the phase shifters have continuously adjustable phases. When the number of phase shift bits is finite, Q is at most proportional to the number of sum co-array elements. A smaller value of Q usually suffices in practice, as demonstrated numerically.

Novel contributions included in this thesis only are the characterization of the SNR of image addition in Section 5.2, the tighter upper bounds on Q in (5.21) and Proposition 5.1, as well as the inclusion of waveform diversity in the general analysis of image addition—see (5.6), for instance.

The presented results yield insight into the influence of various system parameters on the number of component images needed in sparse array imaging. Furthermore, they provide explicit methods for computing the physical beamforming weights yielding a desired effective beampattern. The contributions are of theoretical and practical relevance to imaging system designers, who have to weigh the costs and benefits of different array configurations, degrees of waveform diversity, and beamforming architectures.

6.3 Open problems and future work

Several research topics remain for future work. The following list highlights selected directions and open problems suggested by this dissertation:

- **Redundancy of MRA.** The MRA serves as a benchmark for sparse array configurations with a contiguous sum co-array. However, the exact redundancy of the MRA is unknown. Novel array configurations could offer tighter upper bounds on the asymptotic redundancy of the MRA, especially in the linear array case. In the rectangular case, lower bounds applicable to any fixed aspect ratio remain to be derived. In the square array case, a proof or counterexample of the minimum redundancy property of the BA (for any $L \geq 1$) and CRA (any even $L \geq 6$) is yet to be found.

- **General MRA.** Chapter 4 focused on the restricted MRA. However, the general MRA remains unexplored in the case of fully overlapping Tx and Rx arrays (cf. Appendix A.4). For example, it is not known if the general MRA achieves a lower asymptotic redundancy than extremal additive 2-bases, i.e., solutions to the canonical postage stamp problem. The general MRA is of interest because it is the least redundant array for a given number of physical sensors or contiguous DoFs (and aspect ratio).

- **Joint array and beamformer design.** Chapter 5 considered beamformer weight optimization assuming a fixed array configuration. Variable sensor positions could nevertheless be accommodated by imposing a joint sparsity constraint on the Tx and Rx weight vectors of different component images. This joint array and beamforming weight design problem is closely connected to blind deconvolution [254] and phase retrieval [72], where sparsity constraints are regularly employed to obtain unique solutions [286, 300, 197, 245, 117].

Other important subjects also merit closer attention. For example, the practical relevance of this work would benefit from an in-depth study of the discussed sparse array configurations and beamforming techniques in a specific application. For instance, ultrasound imaging often entails challenging near field operating conditions and stringent requirements on the frame rate, which the array and beamformer designs need to take into account. Likewise, future applications such as THz sensing [227] or joint sensing and communications [205] warrant dedicated studies. The considered hybrid beamforming architectures could also be extended to accommodate for low resolution ADCs, partially connected phase shifter networks, and mixed digital/hybrid/analog beamforming (e.g., a fully digital Rx but an analog Tx array). Furthermore, sum co-array-based adaptive beamforming and high-resolution imaging or direction finding are of great practical and theoretical interest. It would additionally be valuable to investigate the Cramér-Rao lower bound of the derived active sensing model and its extensions—especially from the perspective of the co-array.

A. Appendix

A.1 Derivation of received signal model

By (A1) and (A2), the received signal $\check{\boldsymbol{x}}(t) \in \mathbb{C}^{M_\mathrm{r}}$ at time t is the sum of phase shifted copies of the transmitted signals contained in vector $\boldsymbol{s}(t) \in \mathbb{C}^{N_s}$, scaled by the scattering coefficients $\{\gamma_k\}_{k=1}^K$:

$$\check{\boldsymbol{x}}(t) = \boldsymbol{F}_\mathrm{r}^\mathrm{T} \left(\sum_{k=1}^{K} \gamma_k \boldsymbol{a}_\mathrm{r}(\boldsymbol{v}_k) \boldsymbol{a}_\mathrm{t}^\mathrm{T}(\boldsymbol{v}_k) \boldsymbol{F}_\mathrm{t} \boldsymbol{C}_s \boldsymbol{s}(t) + \boldsymbol{n}(t) \right).$$

Here $\boldsymbol{n}(t) \in \mathbb{C}^{N_\mathrm{r}}$ is a receiver noise vector, which by (A5) follows a complex circularly symmetric normal distribution, i.e., $\boldsymbol{n}(t) \sim \mathscr{CN}(\boldsymbol{0}, \sigma^2 \boldsymbol{I})$. By collecting T snapshots at time instances $t = t_1, t_2, \ldots, t_T$ during one pulse, we obtain the $M_\mathrm{r} \times T$ received data matrix

$$\check{\boldsymbol{X}} = \boldsymbol{F}_\mathrm{r}^\mathrm{T} (\boldsymbol{A}_\mathrm{r} \boldsymbol{\Gamma} \boldsymbol{A}_\mathrm{t}^\mathrm{T} \boldsymbol{F}_\mathrm{t} \boldsymbol{C}_s \boldsymbol{S} + \boldsymbol{N}),$$

where $\boldsymbol{S} = [\boldsymbol{s}(t_1), \ldots, \boldsymbol{s}(t_T)]$ is the Tx waveform matrix, and $\boldsymbol{N} = [\boldsymbol{n}(t_1), \ldots, \boldsymbol{n}(t_T)]$ is a noise matrix with i.i.d. zero-mean complex Gaussian entries. By (A2), the scattering coefficients contained in the diagonal matrix $\boldsymbol{\Gamma}$ are fixed during the coherence time of the scene.

The received signal then undergoes matched filtering to deconvolve the transmitted signals from the received data and improve the SNR. The data matrix after this final linear pre-processing stage becomes $\boldsymbol{X} = \check{\boldsymbol{X}} \boldsymbol{S}^\mathrm{H} \in \mathbb{C}^{M_\mathrm{r} \times N_s}$, which yields the received signal model in (3.4).

A.2 Relaxations to signal model assumptions

In practice, assumptions (A1) to (A5) of Section 3.1 may not hold exactly. For example, deviations to the sum co-array model may be induced by wideband waveforms, near field or incoherent scatterers, sensor nonidealities, such as mutual coupling or cross-talk, as well as interference or clutter.

A.2.1 Wideband transmit waveforms

Wideband transmit pulses are regularly employed in, for example, radar, sonar and ultrasound applications to improve range resolution. The narrowband assumption (A1) may therefore not always be valid. Wideband processing can be implemented simply using a bank of narrowband processors, or tapped delay lines after each sensor [278, ch. 6.13]. True time delays should be used to allow for frequency dependent phase shifting [235]. Interaction between the transmitted waveforms and frequency-selective scatterers or the (dispersive) propagation medium may have to be modeled as convolutions in the time domain or multiplications in the frequency domain.

Fortunately, wideband effects are typically benign and mainly provide additional DoFs for array processing tasks, such as beamforming and parameter estimation (assuming frequency-independent reflectivity). Frequency content beyond the carrier frequency manifests as extra virtual elements in the co-array. Indeed, since the electrical and virtual array aperture vary with wavelength, the wideband co-array can be interpreted as the union of narrowband *dilated co-arrays*, each corresponding to a discrete frequency in the transmitted pulse (active sensing) or source signal spectrum (passive sensing) [9, 10]. Specifically, for transmit pulse with (baseband) frequency support $\mathscr{B}$, the wideband sum co-array is [10]

$$\bigcup_{f\in\mathscr{B}} \left(1+\frac{f}{f_\mathrm{c}}\right)\mathscr{D}_\Sigma = \left\{ \left(1+\frac{f}{f_\mathrm{c}}\right)(\boldsymbol{d}_\mathrm{t}+\boldsymbol{d}_\mathrm{r}) \;\middle|\; \boldsymbol{d}_\xi \in \mathscr{D}_\xi; f\in\mathscr{B} \right\},$$

where f is any frequency in the spectrum of the pulse and $\mathscr{D}_\Sigma$ is the sum co-array in (3.12) at the carrier frequency f_c. For a large number of discrete frequencies, or a continuous spectrum, the wideband co-array becomes a continuous virtual aperture. Bandwidth can thus be exploited to fill the co-array and reduce the number of physical sensors [192, 37, 220].

A.2.2 Incoherent scatterers

Scattering coefficients may vary between pulses or scans due to small changes in orientation with respect to the Tx or Rx array [260]. For instance, the radar cross-section of non-spherical objects can be sensitive to even minor angular perturbations [248, pp. 33–46]—a fact which is exploited by stealth aircraft. Scatterers are therefore commonly assumed to be incoherent between pulses [277, 102]. In this case, (A2) is replaced by the assumption of K *uncorrelated far field point scatterers with zero mean and covariance matrix* $\boldsymbol{R}_\gamma \triangleq \mathbb{E}\big(\boldsymbol{\gamma}\boldsymbol{\gamma}^\mathrm{H}\big) = \mathrm{diag}(\boldsymbol{p})$*, where* $\boldsymbol{p}\in\mathbb{R}^K_{++}$. For simplicity, consider the O-MIMO model in (3.10). The covariance matrix of the received signal, $\boldsymbol{R}_x \triangleq \mathbb{E}(\boldsymbol{x}\boldsymbol{x}^\mathrm{H})$, then becomes

$$\boldsymbol{R}_x = (\boldsymbol{A}_\mathrm{t}\odot\boldsymbol{A}_\mathrm{r})\boldsymbol{R}_\gamma(\boldsymbol{A}_\mathrm{t}\odot\boldsymbol{A}_\mathrm{r})^\mathrm{H}+\sigma^2\boldsymbol{I}.$$

Correspondingly, the vectorized covariance, $\boldsymbol{r}_x \triangleq \mathrm{vec}(\boldsymbol{R}_x)$, reduces to

$$\boldsymbol{r}_x = (\boldsymbol{A}_\mathrm{t}^* \odot \boldsymbol{A}_\mathrm{r}^* \odot \boldsymbol{A}_\mathrm{t} \odot \boldsymbol{A}_\mathrm{r})\boldsymbol{p} + \sigma^2 \mathrm{vec}(\boldsymbol{I}).$$

The major difference to the received signal model of the O-MIMO array in (3.10) is that the effective steering matrix is now $\boldsymbol{A}_\mathrm{t}^* \odot \boldsymbol{A}_\mathrm{r}^* \odot \boldsymbol{A}_\mathrm{t} \odot \boldsymbol{A}_\mathrm{r}$, which has at most $N_\mathrm{t}^2 N_\mathrm{r}^2$ unique rows. This is obviously much more than $N_\mathrm{t} N_\mathrm{r}$, which implies that, compared to (3.5), even more scatterers may be resolved using the same number of physical sensors [35, 213]. In fact, by (A4), the incoherent measurement model has support on the *difference-sum co-array*,

$$\mathscr{D}_\Sigma - \mathscr{D}_\Sigma = \left\{ \boldsymbol{d}_\mathrm{t} + \boldsymbol{d}_\mathrm{r} - \boldsymbol{d}'_\mathrm{t} - \boldsymbol{d}'_\mathrm{r} \;\middle|\; \boldsymbol{d}_\xi, \boldsymbol{d}'_\xi \in \mathscr{D}_\xi \right\}.$$

This reduces to the difference co-array of the Rx (Tx) array for a single Tx (Rx) sensor. Note that the coherent signal model in (3.5) can be thought of as a worst-case scenario, as more uncorrelated scatterers than the number of sum co-array elements can always be resolved.

In practice, the covariance matrix has to be estimated from a finite sample. This may limit the use of second or higher-order statistics in rapidly changing scattering environments, where the coherence time is short compared to the observation period. For example, a full rank estimate of the sample covariance matrix could require as many as $N_\mathrm{t} N_\mathrm{r}$ snapshots, each corresponding to a separate transmission and reception. In contrast, the coherent signal model in (3.5) requires only first-order statistics, and is therefore applicable even in the single snapshot case. Ultimately, the appropriate signal model depends on the time-dynamics of the sensing environment, as rapidly changing or moving scatterers will only stay coherent for short periods of time.

A.2.3 Near field scatterers

The far field assumption in (A2) becomes increasingly inaccurate when the distance between the array and the closest scatterer approaches the electrical aperture of the array. This may be the case in medical ultrasound applications, where the scanning probe is in direct contact with the patient.

In the presence of near field scatterers, the true spherical shape of the propagating wavefronts have to be taken into account. The co-array therefore ceases to have a clear definition and loses some of its utility. However, an approximate perturbation term to the far field co-array can be derived, yielding insight into near field effects [142]. This *spatially varying co-array* [106] depends not only non-linearly on the sensor positions, but also on the scatterer directions and ranges. In particular, for a linear array with normalized Tx/Rx sensor positions $\mathscr{D}_\xi \subset \mathbb{Z}$, inter-sensor spacing $\delta \in \mathbb{R}_+$, a scatterer in direction $v \in [-1, 1]$, the array focused in direction $u \in [-1, 1]$ and range $r \in \mathbb{R}_+$ (of the scatterer), the spatially varying co-array is [106]

$$\mathscr{D}_\Sigma^\mathrm{nf} \approx \left\{ d_\mathrm{r} + d_\mathrm{t} + \frac{u+v}{2r/\delta}\left(d_\mathrm{r}^2 + d_\mathrm{t}^2\right) \;\middle|\; d_\xi \in \mathscr{D}_\xi \right\}.$$

Consequently, the field of view of the array may have to be decreased with range for the far field co-array to remain an adequate model in the near field [142, 10]. The useful field of view may be extended by adjusting the beamforming weights to suppress elevated side/grating lobes caused by the mismatch between the far and near field co-array models [223]. The co-array has been successfully leveraged in near field imaging also in practice [8, 57].

A.2.4 Nonideal sensors

Assumption (A4) does not hold for arrays with directional element gain patterns or nonidealities, such as gain or phase errors [76], mutual coupling [18, 83], cross-talk [129, 302, 92], or perturbations in the sensor positions [136, 288]. These phenomena can affect the Tx/Rx steering vector $\boldsymbol{a}_\xi$ such that the effective steering matrix $\boldsymbol{A}_\mathrm{t} \odot \boldsymbol{A}_\mathrm{r}$ cannot be expressed as a function of the sum co-array as conveniently as in (3.11). Array calibration and wavefield modeling [67] may therefore be necessary to obtain satisfactory performance in various array processing tasks, such as DoA estimation [30, 61].

In the case of direction-dependent but linear nonidealities, the Tx/Rx steering vector in direction $\boldsymbol{v}$ assumes the form $\tilde{\boldsymbol{a}}(\boldsymbol{v}) = \boldsymbol{M}(\boldsymbol{v})\boldsymbol{a}_\xi(\boldsymbol{v})$, where $\boldsymbol{M}_\xi \in \mathbb{C}^{N_\xi \times N_\xi}$ is a perturbation matrix and $\boldsymbol{a}_\xi$ is the ideal Tx/Rx steering vector in (3.1). This results in the effective Tx-Rx steering vector

$$\tilde{\boldsymbol{a}}_\mathrm{t}(\boldsymbol{v}) \otimes \tilde{\boldsymbol{a}}_\mathrm{r}(\boldsymbol{v}) = \big(\boldsymbol{M}_\mathrm{t}(\boldsymbol{v}) \otimes \boldsymbol{M}_\mathrm{r}(\boldsymbol{v})\big)\big(\boldsymbol{a}_\mathrm{t}(\boldsymbol{v}) \otimes \boldsymbol{a}_\mathrm{r}(\boldsymbol{v})\big).$$

For example, the O-MIMO received signal model in (3.10) then becomes

$$\boldsymbol{x} = \sum_{k=1}^{K} \big(\boldsymbol{M}_\mathrm{t}(\boldsymbol{v}_k) \otimes \boldsymbol{M}_\mathrm{r}(\boldsymbol{v}_k)\big)\big(\boldsymbol{a}_\mathrm{t}(\boldsymbol{v}_k) \otimes \boldsymbol{a}_\mathrm{r}(\boldsymbol{v}_k)\big)\gamma_k + \boldsymbol{n},$$

which is similar to the direction-dependent range-Doppler model in (3.20).

If the nonidealities are direction-independent, then the additional DoFs provided by co-array are more immediately leveraged [224] (see also [137] for a similar model). In this case, the perturbed effective Tx-Rx steering matrix is

$$\tilde{\boldsymbol{A}}_\mathrm{t} \odot \tilde{\boldsymbol{A}}_\mathrm{r} = (\boldsymbol{M}_\mathrm{t} \otimes \boldsymbol{M}_\mathrm{r})(\boldsymbol{A}_\mathrm{t} \odot \boldsymbol{A}_\mathrm{r}),$$

where $\boldsymbol{A}_\xi$ is the ideal Tx/Rx steering matrix in (3.2). This can serve as a simple model for mutual coupling in a linear array of dipole antennas. Typically, the coupling magnitude and phase of any sensors pair $d_{\xi,n}, d_{\xi,m}$ are assumed inversely, respectively, linearly proportional to the inter-sensor distance $|d_{\xi,n} - d_{\xi,m}|$ [163]. The resulting mutual coupling model is usually of the form

$$\big[\boldsymbol{M}_\xi\big]_{m,n} = \alpha \frac{\exp(j\beta|d_{\xi,n} - d_{\xi,m}|)}{|d_{\xi,n} - d_{\xi,m}| + c\,\mathbb{1}(n=m)},$$

where $\alpha \in \mathbb{C}$ and $\beta \in [0, 2\pi)$ are parameters representing the coupling magnitude/phase offset and the phase increment, respectively. Although such simplified models are mathematically convenient, they often lack physical rigor.

Mutual coupling is fundamentally a direction and polarization-dependent phenomenon [81]. Accurately assessing its effects therefore requires measurements or physical modeling [36].

A.2.5 Non-Gaussian noise and interference

Sensor nonidealities, such as mutual coupling, may result in nonwhite or non-Gaussian noise, which violates assumption (A5). Noise that does not follow a circularly symmetric complex normal distribution can also be caused by modeling errors, man made or natural impulsive (heavy-tailed) disturbances, interference, and outliers in the data [309, p. 126]. The statistics of the noise do not directly affect the validity of the co-array model. However, robust signal processing may be required to reliably handle deviations from the ideal noise model [308].

Clutter is a prime example of a non-Gaussian source of interference. Clutter generally denotes the unwanted reflections caused by scatterers that are not of direct interest, such as the ground or rain in radar [248, p. 470]. Clutter can be suppressed by beamforming (cf. Section 5.2), or by Doppler processing when the clutter occupies the same resolution cell as a scatterer of interest.

Another non-Gaussian disturbance is *speckle*, which especially affects coherent imaging systems such as synthetic aperture radar [190]. Like clutter, speckle is actually signal-dependent interference, as it is a consequence of the surface roughness of the scattering objects. Speckle is caused by the superposition of reflections from small (compared to the carrier wavelength) coherent scatterers within a resolution cell, which may result in significant fluctuations between pixels in the image. The amplitude and phase of these fluctuations are often exponentially and uniformly distributed, respectively [190, Eq. (8)]. Speckle can be mitigated by incoherently averaging multiple images over different view directions or frequencies [248, p. 528].

A.3 Expression for redundancy of active array

The general expression for redundancy in (4.2) is obtained by decomposing the set of Tx and Rx sensors into the union of overlapping and non-overlapping sensors. Specifically, denote the set of overlapping Tx/Rx sensors as

$$\mathscr{C} \triangleq \mathscr{D}_{\mathrm{t}} \cap \mathscr{D}_{\mathrm{r}}.$$

Hence, $\mathscr{D}_{\xi} = \mathscr{C} \cup (\mathscr{D}_{\xi} \setminus \mathscr{C})$ holds. By basic properties of unions and sums of sets [241, Eq. (3.1)], the sum co-array can then be written as

$$\begin{aligned}\mathscr{D}_{\mathrm{t}} + \mathscr{D}_{\mathrm{r}} &= \mathscr{C} \cup (\mathscr{D}_{\mathrm{t}} \setminus \mathscr{C}) + \mathscr{C} \cup (\mathscr{D}_{\mathrm{r}} \setminus \mathscr{C}) \\ &= (\mathscr{C} + \mathscr{C}) \cup (\mathscr{C} + \mathscr{D}_{\mathrm{t}} \setminus \mathscr{C}) \cup (\mathscr{C} + \mathscr{D}_{\mathrm{r}} \setminus \mathscr{C}) \cup (\mathscr{D}_{\mathrm{t}} \setminus \mathscr{C} + \mathscr{D}_{\mathrm{r}} \setminus \mathscr{C}).\end{aligned}$$

Consequently, the number of sum co-array elements satisfies

$$|\mathscr{D}_{\mathrm{t}} + \mathscr{D}_{\mathrm{r}}| \leq |\mathscr{C} + \mathscr{C}| + |\mathscr{C} + \mathscr{D}_{\mathrm{t}} \setminus \mathscr{C}| + |\mathscr{C} + \mathscr{D}_{\mathrm{r}} \setminus \mathscr{C}| + |\mathscr{D}_{\mathrm{t}} \setminus \mathscr{C} + \mathscr{D}_{\mathrm{r}} \setminus \mathscr{C}|.$$

The maximum number of unique pairwise self sums of N elements is $N(N+1)/2$, whereas the maximum number of unique cross sums between two sets containing N and M elements is MN. Therefore, the number of sum co-array elements is upper bounded as follows:

$$|\mathscr{D}_\mathrm{t}+\mathscr{D}_\mathrm{r}| \leq \frac{1}{2}|\mathscr{C}|\big(|\mathscr{C}|+1\big)+|\mathscr{C}||\mathscr{D}_\mathrm{t}\setminus\mathscr{C}|+|\mathscr{C}||\mathscr{D}_\mathrm{r}\setminus\mathscr{C}|+|\mathscr{D}_\mathrm{t}\setminus\mathscr{C}||\mathscr{D}_\mathrm{r}\setminus\mathscr{C}|.$$

Substituting $|\mathscr{D}_\xi \setminus \mathscr{C}| = |\mathscr{D}_\xi| - |\mathscr{C}|$ into the previous expression then yields

$$|\mathscr{D}_\mathrm{t}+\mathscr{D}_\mathrm{r}| \leq |\mathscr{D}_\mathrm{t}||\mathscr{D}_\mathrm{r}| - \frac{1}{2}|\mathscr{C}|\big(|\mathscr{C}|-1\big),$$

where the right-hand side is the numerator of the redundancy R in (4.2).

Note that for any $|\mathscr{D}_\mathrm{t}|, |\mathscr{D}_\mathrm{r}|$ and $|\mathscr{C}|$, the sets $\mathscr{D}_\mathrm{t}$ and $\mathscr{D}_\mathrm{r}$ can be chosen such that equality holds in the above inequality (simply spacing the elements of $\mathscr{D}_\xi$ adequately nonuniformly and widely apart suffices). By definition, unit redundancy $R = 1$ is achieved if and only if the sum co-array is both nonredundant and contiguous, i.e., $|\mathscr{D}_\mathrm{t}+\mathscr{D}_\mathrm{r}| = |\mathscr{D}_\mathrm{t}||\mathscr{D}_\mathrm{r}| - |\mathscr{C}|(|\mathscr{C}|-1)/2$ and $H_\Sigma = |\mathscr{D}_\mathrm{t}+\mathscr{D}_\mathrm{r}|$.

A.4 General Minimum-Redundancy Array

Chapter 4 focused on the restricted MRA and other low-redundancy array configurations with a contiguous sum co-array. However, the general MRA may actually achieve a lower redundancy by allowing for holes in the co-array.

In the case of non-overlapping or partially overlapping Tx and Rx arrays, the nested construction in Proposition 4.1 is both a general and a restricted MRA. However, in the fully overlapping case, little is known about the general MRA. General linear MRAs correspond to solutions of a generalization of the postage stamp problem, where the postage stamp values are allowed to be negative. Compared to the case of strictly non-negative stamp values, the general postage stamp problem has barely received any attention [19], [95, pp. 246–247]. Two-dimensional solutions, corresponding to general planar MRAs, are completely unknown. We note that Publication V extended the canonical postage stamp problem from $\mathbb{N}$ to $\mathbb{N}^2$. Solutions to this problem correspond to an intermediate form between general and restricted MRAs.[1]

Table 1.1 illustrates the distinction between the restricted and general MRA using three linear arrays with $N = 11$ sensors, corresponding to

(i) an extremal restricted postage stamp set (a restricted MRA)

(ii) an extremal postage stamp set (*not* a restricted *nor* a general MRA)

(iii) a generalized postage stamp set (*possibly* a general MRA).

[1]This terminology is in slight contradiction to Publication IX, where the general MRA was (improperly) defined as a solution to the canonical postage stamp problem.

Table 1.1. Restricted MRA, (i), and two less redundant configurations, (ii) and (iii), for $N = 11$ sensors. The number of contiguous DoFs H_Σ in (3.14) can be increased by allowing for holes in the sum co-array. Little is known about the general MRA, which maximizes H_Σ without constraining the co-array to be contiguous.

	Physical array, $\mathscr{D}$	$\mathscr{D}+\mathscr{D}$	H_Σ	Reference
(i)	$\{0,1,2,5,8,11,14,17,20,21,22\}$	$\{0:44\}$	45	[132]
(ii)	$\{0,1,2,3,7,11,15,19,21,22,24\}$	$\{0:46,48\}$	47	[134]
(iii)	$\{0,2,3,5,9,13,17,21,23,24,26\}$	$\{0,2:50,52\}$	49	[19]

Configuration (i) is a solution to the restricted postage stamp problem, i.e., an extremal restricted additive 2-basis or restricted MRA, and thus achieves a contiguous sum co-array with $H_\Sigma = 45$ elements. Configuration (ii) is a solution to the canonical postage stamp problem, i.e., an extremal additive 2-basis, which achieves $H_\Sigma = 47$ contiguous DoFs at the expense of a non-contiguous co-array. This configuration maximizes H_Σ under the constraint that the contiguous subarray of the sum co-array contains the origin, $\{0\}$. By relaxing this requirement, the number of contiguous DoFs can be increased further to $H_\Sigma = 49$, as configuration (iii) demonstrates. Whether configuration (iii) is a general MRA is still unknown. Note that there is no obvious *a priori* reason for the contiguous subarray of the sum co-array to contain the origin. This is unlike the general difference MRA, which must contain the origin, as a less redundant configuration could otherwise be constructed.[2]

A.5 Variance of beamformer output after image addition

In the following we derive the variance of the beamformer output after image addition. First, note that (5.5) can be written as $y = \tilde{s} + \tilde{n}$, where $\tilde{s}$ is a deterministic signal component and $\tilde{n}$ is stochastic noise component. Assuming independent noise realizations between pulses, the noise term can be expressed as

$$\tilde{n} \triangleq \sum_{p=1}^{P} \tilde{\boldsymbol{w}}_p^{\mathrm{T}} \boldsymbol{n}_p,$$

where the beamforming weight vector of the pth pulse is

$$\tilde{\boldsymbol{w}}_p = \sum_{q \in \mathscr{I}_p} \boldsymbol{S}^{\mathrm{H}} \boldsymbol{w}_{s,q} \otimes \boldsymbol{w}_{\mathrm{r},q}.$$

Here, P is the number of pulses and $\mathscr{I}_p$ the set of component image indices associated with the pth pulse—see the definitions in (5.6) and (5.7).

By assumption (A5), the noise vector of each pulse follows a complex circularly symmetric distribution, $\boldsymbol{n}_p \sim \mathscr{CN}(\boldsymbol{0}, \sigma^2 \boldsymbol{I})$. Since $\tilde{n}$ is a sum of independent

[2] Proof by contradiction: Assume $\mathscr{D}$ is the MRA. If $\{\boldsymbol{0}\} \notin \mathscr{D} - \mathscr{D}$, then $|\mathscr{D} - \mathscr{D}| \leq N(N-1)/2$. However, the minimum-redundancy NA satisfies $|\mathscr{D}_{\mathrm{NA}} - \mathscr{D}_{\mathrm{NA}}| \geq N(N+2)/2 - 1$ [200], which is greater than $N(N-1)/2$ for $N \geq 1$. Hence, $\mathscr{D}$ cannot be the MRA.

zero-mean complex normal random variables, it also follows a complex normal distribution with zero mean. By the independence of the noise between pulses, the variance of $\tilde{n}$ reduces to

$$\mathbb{E}(|\tilde{n}|^2) = \sigma^2 \sum_{p=1}^{P} \|\tilde{\boldsymbol{w}}_p\|_2^2,$$

where by (3.3) and basic properties of the Kronecker product we have

$$\|\tilde{\boldsymbol{w}}_p\|_2^2 = \left\| \sum_{q \in \mathscr{I}_p} \boldsymbol{S}^{\mathrm{H}} \boldsymbol{w}_{s,q} \otimes \boldsymbol{w}_{\mathrm{r},q} \right\|_2^2 = \left\| \sum_{q \in \mathscr{I}_p} \boldsymbol{R}_s^{1/2} \boldsymbol{w}_{s,q} \otimes \boldsymbol{w}_{\mathrm{r},q} \right\|_2^2.$$

Hence, the variance of the noise or the beamformed signal y is

$$\mathbb{E}\big(|y - \mathbb{E}(y)|^2\big) = \mathbb{E}(|\tilde{n}|^2) = \sigma^2 \sum_{p=1}^{P} \left\| \sum_{q \in \mathscr{I}_p} \boldsymbol{R}_s^{1/2} \boldsymbol{w}_{s,q} \otimes \boldsymbol{w}_{\mathrm{r},q} \right\|_2^2.$$

In the single component image case $Q = 1$, which implies $P = 1$ since $P = \lceil Q/N_s \rceil$, we recover the variance of the beamformed output without image addition, i.e., $\sigma^2 \|\boldsymbol{R}_s^{1/2} \boldsymbol{w}_s\|_2^2 \|\boldsymbol{w}_{\mathrm{r}}\|_2^2$, as asserted in (5.3).

A.6 Lower bound on number of component images of URA

Consider a URA with $N = N_x N_y$ transceivers, where N_x and N_y denote the number of physical sensors in the x and z dimensions. The number of sum co-array elements is $N_\Sigma = h_x h_y = (2N_x - 1)(2N_y - 1)$. The lower bound on the number of component images can thus be written as $Q \geq g$, where by (5.20)

$$g = N - \sqrt{N^2 - 4N + 2(N_x + N_y) - 1}.$$

We now show that if the array is strictly planar, i.e., $N_x, N_y \geq 2$, then (5.20) implies that $Q \geq 2$. First note that

$$1 = N - \sqrt{(N-1)^2} = N - \sqrt{N^2 - 2N + 1}.$$

Consequently, $g > 1$ if and only if

$$-2N + 2(N_x + N_y) - 2 < 0 \iff 0 < (N_x - 1)(N_y - 1).$$

If $N_x, N_y \geq 2$, then $(N_x - 1)(N_y - 1) > 0$, which implies that $g > 1$, i.e., $Q \geq 2$. It is easy to verify that actually $g \leq 2$. Again, note that

$$2 = N - \sqrt{(N-2)^2} = N - \sqrt{N^2 - 4N + 4}.$$

This implies that $g \leq 2$ if and only if

$$2(N_x + N_y) - 5 \geq 0 \iff N_x + N_y - 1 \geq \frac{5}{2}.$$

If $N_x, N_y \geq 2$, then $N_x + N_y - 1 \geq 3 > 5/2$, which implies that $g \leq 2$. Consequently, $Q \geq 2$ is the greatest lower bound that follows from (5.20) in case of the strictly planar URA.

A.7 Image addition: a general framework for linear imaging

In this appendix, we shortly consider previous works related to image addition and examine connections to applications beyond active imaging. In particular, we offer a broad interpretation of image addition as a general framework for linear imaging techniques.

A.7.1 Origins and related concepts in imaging

The origins of image addition can be traced back to the mid 1960s. Early works by Gabor et al. considered the phase-coherent summation of component images in optical holography [88]. Around the same time, Wild applied similar ideas to incoherent imaging in radio astronomy using annular apertures [295]. Hoctor and Kassam later generalized Wild's image synthesis method to both coherent and incoherent imaging using the co-array formalism [111]. In particular, Kassam et al. used image addition to match the image quality of elliptical, rectangular, and arbitrary convex polygonal continuous apertures with a filled interior using only (subapertures on) the boundary of the array [178, 121, 122, 139, 141]. Kozick and Kassam also considered approximating the image quality achieved by continuous apertures using SVD and a finite number of sensors and component images [139, 140].

Curiously, image addition is rarely explicitly mentioned in the contemporary array processing literature. Active sensing and imaging nevertheless routinely employ multiple transmission-receptions, or transmission schemes based on synthetic aperture techniques, waveform diversity, or multiple frequencies, as pointed out in Section 2.4 and Appendix A.2.1. All of these approaches fit within the image addition framework. Indeed, the co-array can be synthesized and weighted in various ways using multiplexing in time, space, or frequency. For example, synthetic aperture radar (SAR) is a form of temporal multiplexing. SAR, which is routinely employed by remote sensing satellites [190], uses the motion of the transmitter or receiver to create a large virtual array (co-array) that improves resolution compared to the stationary array. SAR techniques are also employed in passive sensing in conjunction with sparse arrays [219, 218].

In ultrasound imaging, so-called plane wave compounding [189] is a popular method with parallels to image addition and synthetic aperture techniques. In plane wave compounding, several defocused transmissions are used to reduce the scan time by avoiding transmit focusing. The component images are linearly combined post-acquisition to form a composite image by synthetic focusing. This may be interpreted as a form of image addition, where the transmit weights of the component images are chosen to produce plane waves at diverse angles. Defocused transmissions are a practical alternative to range focusing on transmit when a high frame rate is required. Plane wave compounding, together with compressive sensing techniques [284, 44], Fourier-domain processing [55, 54], or sparse arrays [60] enable real-time three-dimensional imaging, which is of par-

ticular importance in medical imaging applications, such as echocardiography.

A.7.2 Connections beyond imaging

The key ideas of image addition have also independently emerged in non-imaging applications. In the design of multistage separable two-dimensional filters, the response of any filter can be decomposed into a sum of (separable) filters expressible as the product of a pair of one-dimensional filters [269]. The filter coefficients of the one-dimensional filters are analogous to the physical beamforming weights of the Tx and Rx arrays. The analogy is particularly appropriate in case of the fully digital beamformer. For example, [247] considered reducing the computational complexity of separable filter learning by solving a real-valued unconstrained optimization problem similar to the nuclear norm relaxation of (P5.1) discussed in Section 5.3.1 and Publication II.

Problems with Kronecker structure akin to that encountered in image addition have even appeared in communications. For instance, a low-dimensional Kronecker factorization of the Rx beamforming vector can yield a computational advantage in massive MIMO systems employing planar arrays and beamforming in both azimuth and elevation [229]. Multiple transmissions (corresponding to $Q > 1$) are generally avoided in communications when spectral efficiency is of principal concern.

Moreover, image addition is fundamentally connected to so-called *blind* problems [11, 161, 300], such as blind deconvolution in image processing [254, 144, 153], blind channel identification or equalization in communications [171, 268, 195], and self-calibration in array processing [75, 82]. Indeed, the task of recovering the unknown Tx and Rx beamforming weights from their convolution—the sum co-array beamforming weight function—is a (noiseless) blind deconvolution problem. Note that image addition modifies the standard blind deconvolution problem by allowing for the desired result to be comprised of the sum of several convolutions (for example, see [181]).

References

[1] Y. I. Abramovich and G. J. Frazer. Bounds on the volume and height distributions for the MIMO radar ambiguity function. *IEEE Signal Processing Letters*, 15:505–508, 2008.

[2] Y. I. Abramovich, D. A. Gray, A. Y. Gorokhov, and N. K. Spencer. Positive-definite Toeplitz completion in DOA estimation for nonuniform linear antenna arrays. I. fully augmentable arrays. *IEEE Transactions on Signal Processing*, 46(9):2458–2471, Sep 1998.

[3] Y. I. Abramovich, O. A. Gray, A. Y. Gorokhov, and N. K. Spencer. Comparison of DOA estimation performance for various types of sparse antenna array geometries. In *8th European Signal Processing Conference, EUSIPCO 1996*, pages 1–4, Sept 1996.

[4] Y. I. Abramovich, N. K. Spencer, and A. Y. Gorokhov. Positive-definite Toeplitz completion in DOA estimation for nonuniform linear antenna arrays. II. partially augmentable arrays. *IEEE Transactions on Signal Processing*, 47(6):1502–1521, Jun 1999.

[5] K. Adhikari, J. R. Buck, and K. E. Wage. Extending coprime sensor arrays to achieve the peak side lobe height of a full uniform linear array. *EURASIP Journal on Advances in Signal Processing*, 2014(1):1–17, 2014.

[6] K. Adhikari and B. Drozdenko. Design and statistical analysis of tapered coprime and nested arrays for the min processor. *IEEE Access*, 7:139601–139615, 2019.

[7] V. D. Agrawal and Y. T. Lo. Distribution of sidelobe level in random arrays. *Proceedings of the IEEE*, 57(10):1764–1765, Oct 1969.

[8] F. Ahmad, G. J. Frazer, S. A. Kassam, and M. G. Amin. Design and implementation of near-field, wideband synthetic aperture beamformers. *IEEE Transactions on Aerospace and Electronic Systems*, 40(1):206–220, Jan 2004.

[9] F. Ahmad and S. A. Kassam. Performance analysis and array design for wide-band beamformers. *Journal of Electronic Imaging*, 7(4):825–838, 1998.

[10] F. Ahmad and S. A. Kassam. Coarray analysis of the wide-band point spread function for active array imaging. *Signal Processing*, 81(1):99–115, 2001.

[11] A. Ahmed, B. Recht, and J. Romberg. Blind deconvolution using convex programming. *IEEE Transactions on Information Theory*, 60(3):1711–1732, 2014.

[12] I. Ahmed, H. Khammari, A. Shahid, A. Musa, K. S. Kim, E. De Poorter, and I. Moerman. A survey on hybrid beamforming techniques in 5G: Architecture and system model perspectives. *IEEE Communications Surveys Tutorials*, 20(4):3060–3097, 2018.

[13] S. S. Ahmed, A. Schiessl, F. Gumbmann, M. Tiebout, S. Methfessel, and L. P. Schmidt. Advanced microwave imaging. *IEEE Microwave Magazine*, 13(6):26–43, Sept 2012.

[14] T. Aittomäki and V. Koivunen. Mismatched filter design and interference mitigation for MIMO radars. *IEEE Transactions on Signal Processing*, 65(2):454–466, 2017.

[15] K. Akiyama et al. First M87 event horizon telescope results. II. array and instrumentation. *The Astrophysical Journal Letters*, 875(1):L2, 2019.

[16] K. Akiyama et al. First M87 event horizon telescope results. IV. imaging the central supermassive black hole. *The Astrophysical Journal Letters*, 875(1):L4, 2019.

[17] A. Alkhateeb, J. Mo, N. González-Prelcic, and R. W. Heath. MIMO precoding and combining solutions for millimeter-wave systems. *IEEE Communications Magazine*, 52(12):122–131, December 2014.

[18] J. L. Allen and B. L. Diamond. Mutual coupling in array antennas. Technical Report 424, Massachusetts Institute Of Technology Lexington Lincoln Lab, 1966.

[19] R. Alter and J. A. Barnett. A postage stamp problem. *The American Mathematical Monthly*, 87(3):206–210, 1980.

[20] M. G Amin. *Through-the-wall radar imaging*. CRC press, Boca Raton, 1st edition, 2013.

[21] M. G. Amin, X. Wang, Y. D. Zhang, F. Ahmad, and E. Aboutanios. Sparse arrays and sampling for interference mitigation and DOA estimation in GNSS. *Proceedings of the IEEE*, 104(6):1302–1317, 2016.

[22] J Arsac. Application of mathematical theories of approximation to aerial smoothing in radio astronomy. *Australian Journal of Physics*, 10(1):16–28, 1957.

[23] L. Atzori, A. Iera, and G. Morabito. The Internet of Things: A survey. *Computer Networks*, 54(15):2787–2805, 2010.

[24] A. Austeng and S. Holm. Sparse 2-D arrays for 3-D phased array imaging - design methods. *IEEE Transactions on Ultrasonics, Ferroelectrics, and Frequency Control*, 49(8):1073–1086, 2002.

[25] A. Austeng and S. Holm. Sparse 2-D arrays for 3-D phased array imaging - experimental validation. *IEEE Transactions on Ultrasonics, Ferroelectrics, and Frequency Control*, 49(8):1087–1093, 2002.

[26] O. E. Ayach, S. Rajagopal, S. Abu-Surra, Z. Pi, and R. W. Heath. Spatially sparse precoding in millimeter wave MIMO systems. *IEEE Transactions on Wireless Communications*, 13(3):1499–1513, March 2014.

[27] C. A. Balanis. *Antenna theory: analysis and design*. John Wiley & sons, 4th edition, 2016.

[28] A. Barabell. Improving the resolution performance of eigenstructure-based direction-finding algorithms. In *IEEE International Conference on Acoustics, Speech, and Signal Processing, ICASSP 1983*, volume 8, pages 336–339, 1983.

[29] D. Barton and S. Sherman. *Monopulse Principles and Techniques*. Artech House radar series. Artech House, Norwood, Mass, 2nd edition, 2011.

[30] F. Belloni, A. Richter, and V. Koivunen. DOA estimation via manifold separation for arbitrary array structures. *IEEE Transactions on Signal Processing*, 55(10):4800–4810, 2007.

[31] K. A. Blanton and J. H. McClellan. New search algorithm for minimum redundancy linear arrays. In *International Conference on Acoustics, Speech, and Signal Processing, ICASSP 1991*, pages 1361–1364 vol.2, Apr 1991.

[32] D. W. Bliss and K. W. Forsythe. Multiple-input multiple-output (MIMO) radar and imaging: degrees of freedom and resolution. In *37th Asilomar Conference on Signals, Systems and Computers*, volume 1, pages 54–59 Vol.1, 2003.

[33] G. S. Bloom and S. W. Golomb. Applications of numbered undirected graphs. *Proceedings of the IEEE*, 65(4):562–570, April 1977.

[34] S. D. Blunt and E. L. Mokole. Overview of radar waveform diversity. *IEEE Aerospace and Electronic Systems Magazine*, 31(11):2–42, 2016.

[35] E. BouDaher, F. Ahmad, and M. G. Amin. Sparsity-based direction finding of coherent and uncorrelated targets using active nonuniform arrays. *IEEE Signal Processing Letters*, 22(10):1628–1632, Oct 2015.

[36] E. BouDaher, F. Ahmad, M. G. Amin, and A. Hoorfar. Mutual coupling effect and compensation in non-uniform arrays for direction-of-arrival estimation. *Digital Signal Processing*, 61:3–14, 2017.

[37] E. BouDaher, Y. Jia, F. Ahmad, and M. G. Amin. Multi-frequency co-prime arrays for high-resolution direction-of-arrival estimation. *IEEE Transactions on Signal Processing*, 63(14):3797–3808, July 2015.

[38] R. N. Bracewell, R. S. Colvin, L. R. D'Addario, C. J. Grebenkemper, K. M. Price, and A. R. Thompson. The Stanford five-element radio telescope. *Proceedings of the IEEE*, 61(9):1249–1257, Sept 1973.

[39] R. N. Bracewell and J. A. Roberts. Aerial smoothing in radio astronomy. *Australian Journal of Physics*, 7(4):615–640, 1954.

[40] A. Brauer. A problem of additive number theory and its application in electrical engineering. *J. Elisha Mitchell Sci. Soc*, 61:55–66, 1945.

[41] Y. Bresler and A. Macovski. Exact maximum likelihood parameter estimation of superimposed exponential signals in noise. *IEEE Transactions on Acoustics, Speech, and Signal Processing*, 34(5):1081–1089, 1986.

[42] O. M. Bucci, M. D'Urso, T. Isernia, P. Angeletti, and G. Toso. Deterministic synthesis of uniform amplitude sparse arrays via new density taper techniques. *IEEE Transactions on Antennas and Propagation*, 58(6):1949–1958, 2010.

[43] H. P. Bucker. High resolution cross-sensor beamforming for a billboard array. *The Journal of the Acoustical Society of America*, 65(1):145–147, 1979.

[44] A. Burshtein, M. Birk, T. Chernyakova, A. Eilam, A. Kempinski, and Y. C. Eldar. Sub-Nyquist sampling and Fourier domain beamforming in volumetric ultrasound imaging. *IEEE Transactions on Ultrasonics, Ferroelectrics, and Frequency Control*, 63(5):703–716, 2016.

[45] E. J. Candès and C. Fernandez-Granda. Super-resolution from noisy data. *Journal of Fourier Analysis and Applications*, 19(6):1229–1254, 2013.

[46] E. J. Candès and C. Fernandez-Granda. Towards a mathematical theory of super-resolution. *Communications on Pure and Applied Mathematics*, 67(6):906–956, 2014.

[47] J. Capon, R. J. Greenfield, and R. J. Kolker. Multidimensional maximum-likelihood processing of a large aperture seismic array. *Proceedings of the IEEE*, 55(2):192–211, Feb 1967.

[48] D. G. Chachlakis, T. Zhou, F. Ahmad, and P. P. Markopoulos. Minimum mean-squared-error autocorrelation processing in coprime arrays, 2020.

[49] M. F. Challis. Two new techniques for computing extremal h-bases A_k. *The Computer Journal*, 36(2):117–126, 1993.

[50] C. Chambers, T. C. Tozer, K. C. Sharman, and T. S. Durrani. Temporal and spatial sampling influence on the estimates of superimposed narrowband signals: when less can mean more. *IEEE Transactions on Signal Processing*, 44(12):3085–3098, 1996.

[51] C.-Y. Chen and P. P. Vaidyanathan. Minimum redundancy MIMO radars. In *IEEE International Symposium on Circuits and Systems (ISCAS)*, pages 45–48, May 2008.

[52] S. P. Chepuri and G. Leus. Sensor selection for estimation, filtering, and detection. In *2014 International Conference on Signal Processing and Communications (SPCOM)*, pages 1–5, Bangalore, India, Dec 2014.

[53] S. P. Chepuri and G. Leus. Continuous sensor placement. *IEEE Signal Processing Letters*, 22(5):544–548, 2015.

[54] T. Chernyakova, R. Cohen, R. Mulayoff, Y. Sde-Chen, C. Fraschini, J. Bercoff, and Y. C. Eldar. Fourier-domain beamforming and structure-based reconstruction for plane-wave imaging. *IEEE Transactions on Ultrasonics, Ferroelectrics, and Frequency Control*, 65(10):1810–1821, 2018.

[55] T. Chernyakova and Y. C. Eldar. Fourier-domain beamforming: the path to compressed ultrasound imaging. *IEEE Transactions on Ultrasonics, Ferroelectrics, and Frequency Control*, 61(8):1252–1267, 2014.

[56] R. Cohen and Y. C. Eldar. Optimized sparse array design based on the sum coarray. In *IEEE International Conference on Acoustics, Speech and Signal Processing (ICASSP)*, pages 3340–3343, 2018.

[57] R. Cohen and Y. C. Eldar. Sparse convolutional beamforming for ultrasound imaging. *IEEE Transactions on Ultrasonics, Ferroelectrics, and Frequency Control*, 65(12):2390–2406, Dec 2018.

[58] R. Cohen and Y. C. Eldar. Sparse Doppler sensing based on nested arrays. *IEEE Transactions on Ultrasonics, Ferroelectrics, and Frequency Control*, 65(12):2349–2364, 2018.

[59] R. Cohen and Y. C. Eldar. Sparse array design via fractal geometries. *IEEE Transactions on Signal Processing*, 68:4797–4812, 2020.

[60] R. Cohen, N. Fingerhut, F. Varray, H. Liebgott, and Y. C. Eldar. Sparse convolutional beamforming for 3D ultrafast ultrasound imaging. *arXiv preprint arXiv:2004.11297*, 2020.

[61] M. Costa, A. Richter, and V. Koivunen. DOA and polarization estimation for arbitrary array configurations. *IEEE Transactions on Signal Processing*, 60(5):2330–2343, 2012.

[62] C. M. Coviello, R. J. Kozick, A. Hurrell, P. P. Smith, and C. C. Coussios. Thin-film sparse boundary array design for passive acoustic mapping during ultrasound therapy. *IEEE Transactions on Ultrasonics, Ferroelectrics, and Frequency Control*, 59(10), October 2012.

[63] F. Daum and J. Huang. MIMO radar: Snake oil or good idea? *IEEE Aerospace and Electronic Systems Magazine*, 24(5):8–12, 2009.

[64] J. F. DeFord and O. P. Gandhi. Phase-only synthesis of minimum peak sidelobe patterns for linear and planar arrays. *IEEE Transactions on Antennas and Propagation*, 36(2):191–201, Feb 1988.

[65] P. E. Dewdney, P. J. Hall, R. T. Schilizzi, and T. J. L. W. Lazio. The Square Kilometre Array. *Proceedings of the IEEE*, 97(8):1482–1496, 2009.

[66] R. Dooley. The optimum design of small nonuniformly spaced arrays. *IEEE Transactions on Antennas and Propagation*, 20(5):636–637, Sep 1972.

[67] M. A. Doron and E. Doron. Wavefield modeling and array processing, part I—spatial sampling. *IEEE Transactions on Signal Processing*, 42(10):2549–2559, 1994.

[68] P. Erdös and I. S. Gál. On the representation of $1,2,...,N$ by differences. *Indagationes Math*, 10:379–382, 1948.

[69] J. E. Evans, D. F. Sun, and J. R. Johnson. Application of advanced signal processing techniques to angle of arrival estimation in ATC navigation and surveillance systems. Technical report, Massachusetts Inst of Tech Lexington Lincoln Lab, 1982.

[70] M. Fazel. *Matrix rank minimization with applications*. PhD thesis, Stanford University, 2002.

[71] A. Fenster, D. B. Downey, and H. N. Cardinal. Three-dimensional ultrasound imaging. *Physics in Medicine and Biology*, 46(5):R67–R99, apr 2001.

[72] J. R. Fienup. Phase retrieval algorithms: a comparison. *Appl. Opt.*, 21(15):2758–2769, Aug 1982.

[73] E. Fishler, A. Haimovich, R. S. Blum, L. J. Cimini, D. Chizhik, and R. A. Valenzuela. Spatial diversity in radars—models and detection performance. *IEEE Transactions on Signal Processing*, 54(3):823–838, 2006.

[74] S. Foucart and H. Rauhut. *A Mathematical Introduction to Compressive Sensing*. Birkhäuser, 2013.

[75] B. Friedlander. Self Calibration Techniques For High-Resolution Array Processing. In F. T. Luk, editor, *Advanced Algorithms and Architectures for Signal Processing III*, volume 0975, pages 377 – 384. International Society for Optics and Photonics, SPIE, 1988.

[76] B. Friedlander. A sensitivity analysis of the MUSIC algorithm. *IEEE Transactions on Acoustics, Speech, and Signal Processing*, 38(10):1740–1751, 1990.

[77] B. Friedlander. On the relationship between MIMO and SIMO radars. *IEEE Transactions on Signal Processing*, 57(1):394–398, 2009.

[78] B. Friedlander. Wireless direction-finding fundamentals. In T. E. Tuncer and B. Friedlander, editors, *Classical and Modern Direction-of-Arrival Estimation*, chapter 1, pages 1–51. Academic Press, Boston, 2009.

[79] B. Friedlander. On signal models for MIMO radar. *IEEE Transactions on Aerospace and Electronic Systems*, 48(4):3655–3660, 2012.

[80] B. Friedlander. On the role of waveform diversity in MIMO radar. *Digital Signal Processing*, 23(3):712–721, 2013.

[81] B. Friedlander. Antenna array manifolds for high-resolution direction finding. *IEEE Transactions on Signal Processing*, 66(4):923–932, 2018.

[82] B. Friedlander and T. Strohmer. Bilinear compressed sensing for array self-calibration. In *48th Asilomar Conference on Signals, Systems and Computers*, pages 363–367, 2014.

[83] B. Friedlander and A. J. Weiss. Direction finding in the presence of mutual coupling. *IEEE Transactions on Antennas and Propagation*, 39(3):273–284, Mar 1991.

[84] H. T. Friis and C. B. Feldman. A multiple unit steerable antenna for short-wave reception. *Proceedings of the Institute of Radio Engineers*, 25(7):841–917, 1937.

[85] B. Fuchs and S. Rondineau. Array pattern synthesis with excitation control via norm minimization. *IEEE Transactions on Antennas and Propagation*, PP(99):1–1, Jul 2016.

[86] D. R. Fuhrmann and G. San Antonio. Transmit beamforming for MIMO radar systems using signal cross-correlation. *IEEE Transactions on Aerospace and Electronic Systems*, 44(1):171–186, 2008.

[87] C. Fulton, M. Yeary, D. Thompson, J. Lake, and A. Mitchell. Digital phased arrays: Challenges and opportunities. *Proceedings of the IEEE*, 104(3):487–503, 2016.

[88] D. Gabor, G. W. Stroke, R. C. Restrick, A. T. Funkhouser, and D. Brumm. Optical image synthesis (complex amplitude addition and subtraction) by hollographic Fourier transformation. 1965.

[89] G. Gelli and L. Izzo. Minimum-redundancy linear arrays for cyclostationarity-based source location. *IEEE Transactions on Signal Processing*, 45(10):2605–2608, 1997.

[90] A. B. Gershman and J. F. Bohme. A note on most favorable array geometries for DOA estimation and array interpolation. *IEEE Signal Processing Letters*, 4(8):232–235, 1997.

[91] J. W. Goodman. *Introduction to Fourier optics*. McGraw Hill, 2nd edition, 1996.

[92] P. Gori, A. Iula, M. Pappalardo, N. Lamberti, and F. Montero De Espinosa. Influence of the inter-element coupling on ultrasound array radiation patterns. *Journal of Computational Acoustics*, 09(03):773–788, 2001.

[93] N. Goto and Y. Tsunoda. Sidelobe reduction of circular arrays with a constant excitation amplitude. *IEEE Transactions on Antennas and Propagation*, 25(6):896–898, Nov 1977.

[94] C. R. Greene and R. C. Wood. Sparse array performance. *The Journal of the Acoustical Society of America*, 61(S1):S74–S74, 1977.

[95] C. S. Güntürk and M. B. Nathanson. A new upper bound for finite additive bases. *Acta Arithmetica*, 124.3:235–255, 2006.

[96] M. Guo, Y. D. Zhang, and T. Chen. DOA estimation using compressed sparse array. *IEEE Transactions on Signal Processing*, 66(15):4133–4146, 2018.

[97] A. M. Haimovich, R. S. Blum, and L. J. Cimini. MIMO radar with widely separated antennas. *IEEE Signal Processing Magazine*, 25(1):116–129, 2008.

[98] S. A. Hamza. *Sparse Array Beamformer Design for Active and Passive Sensing*. PhD thesis, Villanova University, 2021.

[99] S. A. Hamza and M. G. Amin. Hybrid sparse array beamforming design for general rank signal models. *IEEE Transactions on Signal Processing*, 67(24):6215–6226, 2019.

[100] S. Han, C. I, Z. Xu, and C. Rowell. Large-scale antenna systems with hybrid analog and digital beamforming for millimeter wave 5G. *IEEE Communications Magazine*, 53(1):186–194, 2015.

[101] R. Harrington. Sidelobe reduction by nonuniform element spacing. *IRE Transactions on Antennas and Propagation*, 9(2):187–192, March 1961.

[102] A. Hassanien and S. A. Vorobyov. Phased-MIMO radar: A tradeoff between phased-array and MIMO radars. *IEEE Transactions on Signal Processing*, 58(6):3137–3151, 2010.

[103] R. A. Haubrich. Array design. *Bulletin of the Seismological Society of America*, 58(3):977–991, 1968.

[104] R. L. Haupt. Thinned arrays using genetic algorithms. *IEEE Transactions on Antennas and Propagation*, 42(7):993–999, 1994.

[105] R. L. Haupt. Adaptively thinned arrays. *IEEE Transactions on Antennas and Propagation*, 63(4):1626–1632, 2015.

[106] L. He and S. A. Kassam. Near-range point spread function coarray analysis for array imaging. *IEEE Transactions on Aerospace and Electronic Systems*, 51(1):397–404, January 2015.

[107] L. He, S. A. Kassam, F. Ahmad, and M. G. Amin. Sparse stepped-frequency waveform design for through-the-wall radar imaging, 2011.

[108] S. W. Hell. Far-field optical nanoscopy. *Science*, 316(5828):1153–1158, 2007.

[109] J. S. Herd and M. D. Conway. The evolution to modern phased array architectures. *Proceedings of the IEEE*, 104(3):519–529, 2016.

[110] R. Hoctor. *The Coarray Approach to Aperture Synthesis for Active and Passive Imaging*. PhD thesis, University of Pennsylvania, 1990.

[111] R. T. Hoctor and S. A. Kassam. The unifying role of the coarray in aperture synthesis for coherent and incoherent imaging. *Proceedings of the IEEE*, 78(4):735–752, Apr 1990.

[112] R. T. Hoctor and S. A. Kassam. High resolution coherent source location using transmit/receive arrays. *IEEE Transactions on Image Processing*, 1(1):88–100, Jan 1992.

[113] R. T. Hoctor and S. A. Kassam. Array redundancy for active line arrays. *IEEE Transactions on Image Processing*, 5(7):1179–1183, Jul 1996.

[114] M. Ibrahim, V. Ramireddy, A. Lavrenko, J. König, F. Römer, M. Landmann, M. Grossmann, G. Del Galdo, and R. S. Thomä. Design and analysis of compressive antenna arrays for direction of arrival estimation. *Signal Processing*, 138:35 – 47, 2017.

[115] M. Ishiguro. Minimum redundancy linear arrays for a large number of antennas. *Radio Science*, 15(6):1163–1170, 1980.

[116] A. Ishimaru. Theory of unequally-spaced arrays. *IRE Transactions on Antennas and Propagation*, 10(6):691–702, November 1962.

[117] K. Jaganathan, S. Oymak, and B. Hassibi. Sparse phase retrieval: Uniqueness guarantees and recovery algorithms. *IEEE Transactions on Signal Processing*, 65(9):2402–2410, 2017.

[118] P. Jain, P. Netrapalli, and S. Sanghavi. Low-rank matrix completion using alternating minimization. In *Proceedings of the forty-fifth annual ACM symposium on Theory of computing*, pages 665–674. ACM, 2013.

[119] K. G. Jansky. Electrical disturbances apparently of extraterrestrial origin. *Proceedings of the Institute of Radio Engineers*, 21(10):1387–1398, 1933.

[120] P. Jarske, T. Saramäki, S. K. Mitra, and Y. Neuvo. On properties and design of nonuniformly spaced linear arrays. *IEEE Transactions on Acoustics, Speech, and Signal Processing*, 36(3):372–380, 1988.

[121] C. Ji, R. T. Hoctor, and S. A. Kassam. Elliptical boundary arrays for coherent and incoherent imaging. In *IEE Proceedings F (Radar and Signal Processing)*, volume 136, pages 210–220. IET, 1989.

[122] C. Ji, S. A. Kassam, and R. T. Hoctor. Aperture synthesis for imaging systems using rectangular boundary arrays. *The Journal of the Acoustical Society of America*, 89(2):799–810, 1991.

[123] D. H. Johnson and D. E. Dudgeon. *Array Signal Processing: Concepts and Techniques*. PTR Prentice Hall, 1993.

[124] J. A. Johnson, M. Karaman, and B. T. Khuri-Yakub. Coherent-array imaging using phased subarrays. part I: basic principles. *IEEE Transactions on Ultrasonics, Ferroelectrics, and Frequency Control*, 52(1):37–50, Jan 2005.

[125] S. Joshi and S. Boyd. Sensor selection via convex optimization. *IEEE Transactions on Signal Processing*, 57(2):451–462, 2009.

[126] M. Karaman, I. O. Wygant, Ö. Oralkan, and B. T. Khuri-Yakub. Minimally redundant 2-D array designs for 3-D medical ultrasound imaging. *IEEE Transactions on Medical Imaging*, 28(7):1051–1061, July 2009.

[127] S. M. Kay. *Fundamentals of statistical signal processing: Estimation theory*. Prentice Hall PTR, 1993.

[128] D. King, R. Packard, and R. Thomas. Unequally-spaced, broad-band antenna arrays. *IRE Transactions on Antennas and Propagation*, 8(4):380–384, July 1960.

[129] G. S. Kino and R. Baer. Theory for cross-coupling. In *IEEE Ultrasonics Symposium*, pages 1013–1019, 1983.

[130] T. Kløve. A class of symmetric 2-bases. *Mathematica Scandinavica*, 47(2):177–180, 1981.

[131] W. C. Knight, R. G. Pridham, and S. M. Kay. Digital signal processing for sonar. *Proceedings of the IEEE*, 69(11):1451–1506, 1981.

[132] J. Kohonen. A meet-in-the-middle algorithm for finding extremal restricted additive 2-bases. *Journal of Integer Sequences*, 17(6), 2014.

[133] J. Kohonen. Early pruning in the restricted postage stamp problem. *arXiv preprint arXiv:1503.03416*, 2015.

[134] J. Kohonen and J. Corander. Addition chains meet postage stamps: reducing the number of multiplications. *Journal of Integer Sequences*, 17(3):14–3, 2014.

[135] A. Koochakzadeh and P. Pal. Cramér-Rao bounds for underdetermined source localization. *IEEE Signal Processing Letters*, 23(7):919–923, July 2016.

[136] A. Koochakzadeh and P. Pal. Performance of uniform and sparse non-uniform samplers in presence of modeling errors: A Cramér-Rao bound based study. *IEEE Transactions on Signal Processing*, 65(6):1607–1621, 2017.

[137] A. Koochakzadeh and P. Pal. Compressed arrays and hybrid channel sensing: A Cramér-Rao bound based analysis. *IEEE Signal Processing Letters*, 27:1395–1399, 2020.

[138] A. Koochakzadeh, H. Qiao, and P. Pal. On fundamental limits of joint sparse support recovery using certain correlation priors. *IEEE Transactions on Signal Processing*, 66(17):4612–4625, Sep. 2018.

[139] R. J. Kozick and S. A. Kassam. Linear imaging with sensor arrays on convex polygonal boundaries. *IEEE Transactions on Systems, Man, and Cybernetics*, 21(5):1155–1166, Sep 1991.

[140] R. J. Kozick and S. A. Kassam. The singular value decomposition applied to linear imaging with rectangular arrays. In *Communications, Computers and Signal Processing, 1991., IEEE Pacific Rim Conference on*, pages 231–234 vol.1, May 1991.

[141] R. J. Kozick and S. A. Kassam. Coarray synthesis with circular and elliptical boundary arrays. *IEEE Transactions on Image Processing*, 1(3):391–405, Jul 1992.

[142] R. J. Kozick and S. A. Kassam. Synthetic aperture pulse-echo imaging with rectangular boundary arrays. *IEEE Transactions on Image Processing*, 2(1):68–79, Jan 1993.

[143] H. Krim and M. Viberg. Two decades of array signal processing research: the parametric approach. *IEEE Signal Processing Magazine*, 13(4):67–94, Jul 1996.

[144] D. Kundur and D. Hatzinakos. Blind image deconvolution. *IEEE Signal Processing Magazine*, 13(3):43–64, 1996.

[145] H. Kuschel, D. Cristallini, and K. E. Olsen. Tutorial: Passive radar tutorial. *IEEE Aerospace and Electronic Systems Magazine*, 34(2):2–19, 2019.

[146] M. Laakso, R. Rajamäki, R. Wichman, and V. Koivunen. Phase-coherent multichannel SDR - sparse array beamforming. In *28th European Signal Processing Conference (EUSIPCO)*, pages 1856–1860, 2021.

[147] E. L. Lawler and D. E. Wood. Branch-and-bound methods: A survey. *Operations Research*, 14(4):699–719, 1966.

[148] R. M. Leahy and B. D. Jeffs. On the design of maximally sparse beamforming arrays. *IEEE Transactions on Antennas and Propagation*, 39(8):1178–1187, 1991.

[149] Y. U. Lee, J. Choi, I. Song, and S. R. Lee. Distributed source modeling and direction-of-arrival estimation techniques. *IEEE Transactions on Signal Processing*, 45(4):960–969, 1997.

[150] J. Leech. On the representation of $1,2,\ldots,n$ by differences. *Journal of the London Mathematical Society*, s1-31(2):160–169, 1956.

[151] D. G. Leeper. Isophoric arrays-massively thinned phased arrays with well-controlled sidelobes. *IEEE Transactions on Antennas and Propagation*, 47(12):1825–1835, 1999.

[152] N. H. Lehmann, A. M. Haimovich, R. S. Blum, and L. Cimini. High resolution capabilities of MIMO radar. In *40th Asilomar Conference on Signals, Systems and Computers*, pages 25–30, 2006.

[153] A. Levin, Y. Weiss, F. Durand, and W. T. Freeman. Understanding blind deconvolution algorithms. *IEEE Transactions on Pattern Analysis and Machine Intelligence*, 33(12):2354–2367, 2011.

[154] H. Li and B. Himed. Transmit subaperturing for MIMO radars with co-located antennas. *IEEE Journal of Selected Topics in Signal Processing*, 4(1):55–65, 2010.

[155] J. Li and P. Stoica. MIMO radar with colocated antennas. *IEEE Signal Processing Magazine*, 24(5):106–114, Sep. 2007.

[156] J. Li and P. Stoica. *MIMO radar signal processing*. John Wiley & Sons, 2009.

[157] J. Li and P. Stoica. The phased array is the maximum SNR active array [lecture notes]. *IEEE Signal Processing Magazine*, 27(2):143–144, 2010.

[158] J. Li, P. Stoica, L. Xu, and W. Roberts. On parameter identifiability of MIMO radar. *IEEE Signal Processing Letters*, 14(12):968–971, 2007.

[159] J. Lien, M. E. Gillian, N.and Karagozler, P. Amihood, C. Schwesig, E. Olson, H. Raja, and I. Poupyrev. Soli: Ubiquitous gesture sensing with millimeter wave radar. *ACM Transactions on Graphics (TOG)*, 35(4):1–19, 2016.

[160] D. A. Linebarger, I. H. Sudborough, and I. G. Tollis. Difference bases and sparse sensor arrays. *IEEE Transactions on Information Theory*, 39(2):716–721, Mar 1993.

[161] S. Ling and T. Strohmer. Self-calibration and bilinear inverse problems via linear least squares. *SIAM Journal on Imaging Sciences*, 11(1):252–292, 2018.

[162] C.-L. Liu and P. P. Vaidyanathan. Remarks on the spatial smoothing step in coarray MUSIC. *IEEE Signal Processing Letters*, 22(9):1438–1442, Sep. 2015.

[163] C.-L. Liu and P. P. Vaidyanathan. Super nested arrays: Linear sparse arrays with reduced mutual coupling – Part I: Fundamentals. *IEEE Transactions on Signal Processing*, 64(15):3997–4012, Aug 2016.

[164] C.-L. Liu and P. P. Vaidyanathan. Super nested arrays: Linear sparse arrays with reduced mutual coupling – Part II: High-order extensions. *IEEE Transactions on Signal Processing*, 64(16):4203–4217, 2016.

[165] C.-L. Liu and P .P. Vaidyanathan. Cramér-Rao bounds for coprime and other sparse arrays, which find more sources than sensors. *Digital Signal Processing*, 61:43 – 61, Feb 2017.

[166] C.-L. Liu and P. P. Vaidyanathan. Hourglass arrays and other novel 2-D sparse arrays with reduced mutual coupling. *IEEE Transactions on Signal Processing*, 65(13):3369–3383, July 2017.

[167] C.-L. Liu and P. P. Vaidyanathan. Optimizing minimum redundancy arrays for robustness. In *52nd Asilomar Conference on Signals, Systems, and Computers*, pages 79–83, 2018.

[168] C.-L. Liu and P. P. Vaidyanathan. Robustness of difference coarrays of sparse arrays to sensor failures—Part I: A theory motivated by coarray MUSIC. *IEEE Transactions on Signal Processing*, 67(12):3213–3226, 2019.

[169] C.-L. Liu and P. P. Vaidyanathan. Robustness of difference coarrays of sparse arrays to sensor failures—Part II: Array geometries. *IEEE Transactions on Signal Processing*, 67(12):3227–3242, 2019.

[170] C.-L. Liu, P. P. Vaidyanathan, and P. Pal. Coprime coarray interpolation for DOA estimation via nuclear norm minimization. In *2016 IEEE International Symposium on Circuits and Systems (ISCAS)*, pages 2639–2642, May 2016.

[171] H. Liu, G. Xu, L. Tong, and T. Kailath. Recent developments in blind channel equalization: From cyclostationarity to subspaces. *Signal Processing*, 50(1):83–99, 1996. Special Issue on Subspace Methods, Part I: Array Signal Processing and Subspace Computations.

[172] Y. Lo. A mathematical theory of antenna arrays with randomly spaced elements. *IEEE Transactions on Antennas and Propagation*, 12(3):257–268, May 1964.

[173] Y. Lo and S. Lee. A study of space-tapered arrays. *IEEE Transactions on Antennas and Propagation*, 14(1):22–30, Jan 1966.

[174] G. R. Lockwood, Pai-Chi Li, M. O'Donnell, and F. S. Foster. Optimizing the radiation pattern of sparse periodic linear arrays. *IEEE Transactions on Ultrasonics, Ferroelectrics, and Frequency Control*, 43(1):7–14, Jan 1996.

[175] G. R. Lockwood, J. R. Talman, and S. S. Brunke. Real-time 3-D ultrasound imaging using sparse synthetic aperture beamforming. *IEEE Transactions on Ultrasonics, Ferroelectrics, and Frequency Control*, 45(4):980–988, July 1998.

[176] G. R. Lookwood and F. S. Foster. Optimizing the radiation pattern of sparse periodic two-dimensional arrays. *IEEE Transactions on Ultrasonics, Ferroelectrics, and Frequency Control*, 43(1):15–19, Jan 1996.

[177] W. F. Lunnon. A postage stamp problem. *The Computer Journal*, 12(4):377–380, 1969.

[178] A. K. Luthra and S. A. Kassam. Side-lobe reduction in the ring array pattern for synthetic aperture imaging of coherent sources. *The Journal of the Acoustical Society of America*, 74(3):840–846, 1983.

[179] A. Macovski. Ultrasonic imaging using arrays. *Proceedings of the IEEE*, 67(4):484–495, 1979.

[180] A. Mamistvalov and Y. C. Eldar. Sparse convolutional beamforming for wireless ultrasound. In *IEEE International Conference on Acoustics, Speech and Signal Processing (ICASSP)*, pages 9254–9258, 2020.

[181] C. J. Martin, O. Martinez-Graullera, G. Godoy, and L. G. Ullate. Coarray synthesis based on polynomial decomposition. *IEEE Transactions on Image Processing*, 19(4):1102–1107, 2010.

[182] F. Marvasti. *Nonuniform sampling: theory and practice*. New York: Kluwer Academic, 2001.

[183] Y. Meurisse and J. P. Delmas. Bounds for sparse planar and volume arrays. *IEEE Transactions on Information Theory*, 47(1):464–468, Jan 2001.

[184] C. D. Meyer. *Matrix analysis and applied linear algebra*. Siam, 2000.

[185] B. Y. Mills and A. G. Little. A high-resolution aerial system of a new type. *Australian Journal of Physics*, 6(3):272–278, 1953.

[186] S. K. Mitra, K. Mondal, M. K. Tchobanou, and G. J. Dolecek. General polynomial factorization-based design of sparse periodic linear arrays. *IEEE Transactions on Ultrasonics, Ferroelectrics, and Frequency Control*, 57(9):1952–1966, 2010.

[187] A. Moffet. Minimum-redundancy linear arrays. *IEEE Transactions on Antennas and Propagation*, 16(2):172–175, Mar 1968.

[188] A. F. Molisch, V. V. Ratnam, S. Han, Z. Li, S. L. H. Nguyen, L. Li, and K. Haneda. Hybrid beamforming for massive MIMO: A survey. *IEEE Communications Magazine*, 55(9):134–141, September 2017.

[189] G. Montaldo, M. Tanter, J. Bercoff, N. Benech, and M. Fink. Coherent plane-wave compounding for very high frame rate ultrasonography and transient elastography. *IEEE Transactions on Ultrasonics, Ferroelectrics, and Frequency Control*, 56(3):489–506, 2009.

[190] A. Moreira, P. Prats-Iraola, M. Younis, G. Krieger, I. Hajnsek, and K. P. Papathanassiou. A tutorial on synthetic aperture radar. *IEEE Geoscience and Remote Sensing Magazine*, 1(1):6–43, 2013.

[191] S. Mossige. Algorithms for computing the h-range of the postage stamp problem. *Mathematics of Computation*, 36(154):575–582, 1981.

[192] J. Moulton. *Enhanced High-Resolution Imaging through Multiple-Frequency Coarray Augmentation*. PhD thesis, University of Pennsylvania, 2010.

[193] J. L. Moulton and S. A. Kassam. High-resolution coherent reflector location with multi-frequency active virtual arrays. In *44th Annual Conference on Information Sciences and Systems (CISS)*, pages 1–5, 2010.

[194] A. Mrose. Untere Schranken für die Reichweiten von Extremalbasen fester Ordnung. *Abh. Math. Semin. Univ. Hambg.*, 48:118–124, 1979.

[195] S. Mulleti, K. Lee, and Y. C. Eldar. Identifiability conditions for compressive multichannel blind deconvolution. *IEEE Transactions on Signal Processing*, 68:4627–4642, 2020.

[196] S. Nannuru, A. Koochakzadeh, K. L. Gemba, P. Pal, and P. Gerstoft. Sparse Bayesian learning for beamforming using sparse linear arrays. *The Journal of the Acoustical Society of America*, 144(5):2719–2729, 2018.

[197] H. Ohlsson and Y. C. Eldar. On conditions for uniqueness in sparse phase retrieval. In *IEEE International Conference on Acoustics, Speech and Signal Processing (ICASSP 2014)*, pages 1841–1845. IEEE, 2014.

[198] S. J. Orfanidis. *Electromagnetic waves and antennas*. Rutgers University New Brunswick, NJ, 2014.

[199] B. Ottersten, R. Roy, and T. Kailath. Signal waveform estimation in sensor array processing. In *23rd Asilomar Conference on Signals, Systems and Computers*, volume 2, pages 787–791, 1989.

[200] P. Pal and P. P. Vaidyanathan. Nested arrays: A novel approach to array processing with enhanced degrees of freedom. *IEEE Transactions on Signal Processing*, 58(8):4167–4181, Aug 2010.

[201] P. Pal and P. P. Vaidyanathan. Nested arrays in two dimensions, part I: Geometrical considerations. *IEEE Transactions on Signal Processing*, 60(9):4694–4705, Sept 2012.

[202] P. Pal and P. P. Vaidyanathan. Nested arrays in two dimensions, part II: Application in two dimensional array processing. *IEEE Transactions on Signal Processing*, 60(9):4706–4718, Sept 2012.

[203] P. Pal and P. P. Vaidyanathan. Pushing the limits of sparse support recovery using correlation information. *IEEE Transactions on Signal Processing*, 63(3):711–726, Feb 2015.

[204] S. M. Patole, M. Torlak, D. Wang, and M. Ali. Automotive radars: A review of signal processing techniques. *IEEE Signal Processing Magazine*, 34(2):22–35, 2017.

[205] B. Paul, A. R. Chiriyath, and D. W. Bliss. Survey of RF communications and sensing convergence research. *IEEE Access*, 5:252–270, 2017.

[206] D. Pearson, S. U. Pillai, and Y. Lee. An algorithm for near-optimal placement of sensor elements. *IEEE Transactions on Information Theory*, 36(6):1280–1284, Nov 1990.

[207] S. U. Pillai. *Array signal processing*. Springer-Verlag, New York, 1989.

[208] S. U. Pillai, Y. Bar-Ness, and F. Haber. A new approach to array geometry for improved spatial spectrum estimation. *Proceedings of the IEEE*, 73(10):1522–1524, Oct 1985.

[209] S. U. Pillai and F. Haber. Statistical analysis of a high resolution spatial spectrum estimator utilizing an augmented covariance matrix. *IEEE Transactions on Acoustics, Speech, and Signal Processing*, 35(11):1517–1523, November 1987.

[210] S. U. Pillai and B. H. Kwon. Forward/backward spatial smoothing techniques for coherent signal identification. *IEEE Transactions on Acoustics, Speech, and Signal Processing*, 37(1):8–15, Jan 1989.

[211] L. C. Potter, E. Ertin, J. T. Parker, and M. Cetin. Sparsity and compressed sensing in radar imaging. *Proceedings of the IEEE*, 98(6):1006–1020, 2010.

[212] H. C. Pumphrey. Design of sparse arrays in one, two, and three dimensions. *The Journal of the Acoustical Society of America*, 93(3):1620–1628, 1993.

[213] H. Qiao, A. Koochakzadeh, and P. Pal. Correlation-aware sensing in active and passive modes for source localization. In *50th Asilomar Conference on Signals, Systems and Computers*, pages 1692–1696, 2016.

[214] H. Qiao and P. Pal. Gridless line spectrum estimation and low-rank Toeplitz matrix compression using structured samplers: A regularization-free approach. *IEEE Transactions on Signal Processing*, 65(9):2221–2236, 2017.

[215] H. Qiao and P. Pal. On maximum-likelihood methods for localizing more sources than sensors. *IEEE Signal Processing Letters*, 24(5):703–706, 2017.

[216] H. Qiao and P. Pal. Unified analysis of co-array interpolation for direction-of-arrival estimation. In *IEEE International Conference on Acoustics, Speech and Signal Processing, ICASSP 2017*, pages 3056–3060, March 2017.

[217] H. Qiao and P. Pal. Guaranteed localization of more sources than sensors with finite snapshots in multiple measurement vector models using difference co-arrays. *IEEE Transactions on Signal Processing*, 67(22):5715–5729, 2019.

[218] H. Qiao, P. Sarangi, Y. Alnumay, and P. Pal. Sample complexity trade-offs for synthetic aperture based high-resolution estimation and detection. In *2020 IEEE 11th Sensor Array and Multichannel Signal Processing Workshop (SAM)*, pages 1–5, 2020.

[219] G. Qin, M. G. Amin, and Y. D. Zhang. DOA estimation exploiting sparse array motions. *IEEE Transactions on Signal Processing*, 67(11):3013–3027, 2019.

[220] S. Qin, Y. D. Zhang, M. G. Amin, and F. Gini. Frequency diverse coprime arrays with coprime frequency offsets for multitarget localization. *IEEE Journal of Selected Topics in Signal Processing*, 11(2):321–335, 2017.

[221] R. Raich, J. Goldberg, and H. Messer. Bearing estimation for a distributed source: modeling, inherent accuracy limitations and algorithms. *IEEE Transactions on Signal Processing*, 48(2):429–441, 2000.

[222] R. Rajamäki and V. Koivunen. Comparison of sparse sensor array configurations with constrained aperture for passive sensing. In *IEEE Radar Conference (RadarConf 2017)*, pages 0797–0802, May 2017.

[223] R. Rajamäki and V. Koivunen. Near field active imaging using sparse arrays. In *52nd Asilomar Conference on Signals, Systems and Computers*, Asilomar, Pacific Grove, CA, November 2018.

[224] R. Rajamäki and V. Koivunen. Co-array MUSIC under angle-independent nonidealities. In *54th Asilomar Conference on Signals, Systems and Computers*, pages 230–235, Asilomar, Pacific Grove, CA, November 2020.

[225] J. Ramirez, N. Bottenus, G. Trahey, and J. L. Krolik. Synthetic aperture imaging with thinned linear sensor arrays for medical ultrasound. In *IEEE Sensor Array and Multichannel Signal Processing Workshop (SAM)*, pages 1–5, 2016.

[226] T. S. Rappaport, R. W. Heath Jr, R. C. Daniels, and J. N. Murdock. Millimeter wave wireless communications. 2015.

[227] T. S. Rappaport, Y. Xing, O. Kanhere, S. Ju, A. Madanayake, S. Mandal, A. Alkhateeb, and G. C. Trichopoulos. Wireless communications and applications above 100 GHz: Opportunities and challenges for 6G and beyond. *IEEE Access*, 7:78729–78757, 2019.

[228] L. Rédei and A. Rényi. On the representation of $1,2,\ldots,N$ by differences. *Mat. Sb. (N.S)*, T. 24 (66)(3):385–389, 1949.

[229] L. N. Ribeiro, A. L. F. de Almeida, J. A. Nossek, and J. C. M. Mota. Low-complexity separable beamformers for massive antenna array systems. *IET Signal Processing*, 13(4):434–442, 2019.

[230] J. P. Robinson. Some postage stamp 2-bases. *Journal of Integer Sequences*, 12(2):3, 2009.

[231] P. Rocca, G. Oliveri, R. J. Mailloux, and A. Massa. Unconventional phased array architectures and design methodologies—a review. *Proceedings of the IEEE*, 104(3):544–560, 2016.

[232] H. Rohrbach. Ein Beitrag zur additiven Zahlentheorie. *Mathematische Zeitschrift*, 42(1):1–30, 1937.

[233] D. Romero, D. D. Ariananda, Z. Tian, and G. Leus. Compressive covariance sensing: Structure-based compressive sensing beyond sparsity. *IEEE Signal Processing Magazine*, 33(1):78–93, 2016.

[234] S. Rost and C. Thomas. Array seismology: Methods and applications. *Reviews of Geophysics*, 40(3):2–1–2–27, 2002.

[235] R. Rotman, M. Tur, and L. Yaron. True time delay in phased arrays. *Proceedings of the IEEE*, 104(3):504–518, 2016.

[236] R. Roy and T. Kailath. ESPRIT — Estimation of signal parameters via rotational invariance techniques. *IEEE Transactions on Acoustics, Speech, and Signal Processing*, 37(7):984–995, Jul 1989.

[237] S. Sandler. Some equivalences between equally and unequally spaced arrays. *IRE Transactions on Antennas and Propagation*, 8(5):496–500, September 1960.

[238] L. L. Scharf. *Statistical signal processing: Detection, Estimation, and Time Series Analysis*. Addison Wesley, 1991.

[239] S. A. Schelkunoff. A mathematical theory of linear arrays. *The Bell System Technical Journal*, 22(1):80–107, 1943.

[240] R. Schmidt. Multiple emitter location and signal parameter estimation. *IEEE Transactions on Antennas and Propagation*, 34(3):276–280, Mar 1986.

[241] R. Schneider. *Convex bodies: the Brunn–Minkowski theory*, volume 151. Cambridge university press, 2nd expanded edition, 2013.

[242] F. Schwartau, Y. Schröder, L. Wolf, and J. Schoebel. Large minimum redundancy linear arrays: Systematic search of perfect and optimal rulers exploiting parallel processing. *IEEE Open Journal of Antennas and Propagation*, 2:79–85, 2021.

[243] S. Sedighi, B. S. M. R. Rao, and B. Ottersten. An asymptotically efficient weighted least squares estimator for co-array-based DoA estimation. *IEEE Transactions on Signal Processing*, 68:589–604, 2020.

[244] S. Shakeri, D. D. Arianandа, and G. Leus. Direction of arrival estimation using sparse ruler array design. In *IEEE 13th International Workshop on Signal Processing Advances in Wireless Communications, SPAWC 2012*, pages 525–529, June 2012.

[245] Y. Shechtman, A. Beck, and Y. C. Eldar. Gespar: Efficient phase retrieval of sparse signals. *IEEE Transactions on Signal Processing*, 62(4):928–938, Feb 2014.

[246] Q. Shen, W. Liu, W. Cui, and S. Wu. Underdetermined DOA estimation under the compressive sensing framework: A review. *IEEE Access*, 4:8865–8878, 2016.

[247] A. Sironi, B. Tekin, R. Rigamonti, V. Lepetit, and P. Fua. Learning separable filters. *IEEE Transactions on Pattern Analysis and Machine Intelligence*, 37(1):94–106, 2015.

[248] M. Skolnik. *Introduction to radar systems*. McGraw-Hill Book Company, 2nd edition, 1981.

[249] M. Skolnik, G. Nemhauser, and J. Sherman. Dynamic programming applied to unequally spaced arrays. *IEEE Transactions on Antennas and Propagation*, 12(1):35–43, 1964.

[250] S. W. Smith, H. G. Pavy, and O. T. von Ramm. High-speed ultrasound volumetric imaging system. I. transducer design and beam steering. *IEEE Transactions on Ultrasonics, Ferroelectrics, and Frequency Control*, 38(2):100–108, 1991.

[251] B. D. Steinberg. *Principles of aperture and array system design: Including random and adaptive arrays*. New York, Wiley-Interscience, 1976.

[252] B. D. Steinberg. Microwave imaging of aircraft. *Proceedings of the IEEE*, 76(12):1578–1592, 1988.

[253] J. Steinwandt, F. Roemer, and M. Haardt. Performance analysis of ESPRIT-type algorithms for co-array structures. In *Seventh IEEE International Workshop on Computational Advances in Multi-Sensor Adaptive Processing, CAMSAP*, pages 1–5, 2017.

[254] T. G. Stockham, T. M. Cannon, and R. B. Ingebretsen. Blind deconvolution through digital signal processing. 63(4):678–692, 1975.

[255] P. Stoica and R. L. Moses. *Spectral analysis of signals*. Pearson Prentice Hall Upper Saddle River, NJ, 2005.

[256] P. Stoica and A. Nehorai. MUSIC, maximum likelihood, and Cramer-Rao bound. *IEEE Transactions on Acoustics, Speech, and Signal Processing*, 37(5):720–741, May 1989.

[257] P. Stoica and A. Nehorai. Performance study of conditional and unconditional direction-of-arrival estimation. *IEEE Transactions on Acoustics, Speech, and Signal Processing*, 38(10):1783–1795, 1990.

[258] P. Stoica and Y. Selen. Model-order selection: a review of information criterion rules. *IEEE Signal Processing Magazine*, 21(4):36–47, July 2004.

[259] P. Stoica and K. C. Sharman. Maximum likelihood methods for direction-of-arrival estimation. *IEEE Transactions on Acoustics, Speech, and Signal Processing*, 38(7):1132–1143, 1990.

[260] P. Swerling. Probability of detection for fluctuating targets. *IRE Transactions on Information Theory*, 6(2):269–308, 1960.

[261] T. L. Szabo. *Diagnostic Ultrasound Imaging: Inside Out*. Elsevier Academic Press, 2nd edition, 2004.

[262] T.-J. Shan, M. Wax, and T. Kailath. On spatial smoothing for direction-of-arrival estimation of coherent signals. *IEEE Transactions on Acoustics, Speech, and Signal Processing*, 33(4):806–811, 1985.

[263] Z. Tan, Y. C. Eldar, and A. Nehorai. Direction of arrival estimation using co-prime arrays: A super resolution viewpoint. *IEEE Transactions on Signal Processing*, 62(21):5565–5576, Nov 2014.

[264] Z. Tan and A. Nehorai. Sparse direction of arrival estimation using co-prime arrays with off-grid targets. *IEEE Signal Processing Letters*, 21(1):26–29, Jan 2014.

[265] C. Tang. An approximate method of designing nonuniformly spaced arrays. *IEEE Transactions on Antennas and Propagation*, 13(1):177–179, Jan 1965.

[266] K. C. Toh, M. J. Todd, and R. H. Tütüncü. SDPT3 — a Matlab software package for semidefinite programming. *Optimization Methods and Software*, 11(1-4):545–581, 1999.

[267] E. Tohidi, M. Coutino, S. P. Chepuri, H. Behroozi, M. M. Nayebi, and G. Leus. Sparse antenna and pulse placement for colocated MIMO radar. *IEEE Transactions on Signal Processing*, 67(3):579–593, 2019.

[268] L. Tong and S. Perreau. Multichannel blind identification: from subspace to maximum likelihood methods. *Proceedings of the IEEE*, 86(10):1951–1968, 1998.

[269] S. Treitel and J. L. Shanks. The design of multistage separable planar filters. *IEEE Transactions on Geoscience Electronics*, 9(1):10–27, 1971.

[270] J. A. Tropp. Greed is good: algorithmic results for sparse approximation. *IEEE Transactions on Information Theory*, 50(10):2231–2242, 2004.

[271] A. Trucco and V. Murino. Stochastic optimization of linear sparse arrays. *IEEE Journal of Oceanic Engineering*, 24(3):291–299, 1999.

[272] T. E. Tuncer, T. K. Yasar, and B. Friedlander. Direction of arrival estimation for nonuniform linear arrays by using array interpolation. *Radio Science*, 42(04):1–11, 2007.

[273] H. Unz. Linear arrays with arbitrarily distributed elements. *IRE Transactions on Antennas and Propagation*, 8(2):222–223, March 1960.

[274] H. Unz. Nonuniform arrays with spacings larger than one wavelength. *IRE Transactions on Antennas and Propagation*, 10(5):647–648, September 1962.

[275] C. Vaidyanathan and K. M. Buckley. Performance analysis of the MVDR spatial spectrum estimator. *IEEE Transactions on Signal Processing*, 43(6):1427–1437, June 1995.

[276] P. P. Vaidyanathan and P. Pal. Sparse sensing with co-prime samplers and arrays. *IEEE Transactions on Signal Processing*, 59(2):573–586, Feb 2011.

[277] S. Valaee, B. Champagne, and P. Kabal. Parametric localization of distributed sources. *IEEE Transactions on Signal Processing*, 43(9):2144–2153, 1995.

[278] H. L. Van Trees. *Optimum Array Processing, Part IV of Detection, Estimation, and Modulation Theory*. Wiley-Interscience, 2002.

[279] B. D. Van Veen and K. M. Buckley. Beamforming: a versatile approach to spatial filtering. *IEEE ASSP Magazine*, 5(2):4–24, 1988.

[280] E. Vertatschitsch and S. Haykin. Nonredundant arrays. *Proceedings of the IEEE*, 74(1):217–217, 1986.

[281] M. Vigano, G. Toso, G. Caille, C. Mangenot, and I. Lager. Sunflower array antenna with adjustable density taper. *International Journal of Antennas and Propagation, Hindawi Publishing Corporation*, 2009, Article ID 876989:222–223, 2009.

[282] S. A. Vorobyov. Principles of minimum variance robust adaptive beamforming design. *Signal Processing - Special Issue on Advances in Sensor Array Processing in Memory of Alex B. Gershman*, 93(12):3264–3277, 2013.

[283] S. A. Vorobyov, A. B. Gershman, and Z.-Q. Luo. Robust adaptive beamforming using worst-case performance optimization: a solution to the signal mismatch problem. *IEEE Transactions on Signal Processing*, 51(2):313–324, 2003.

[284] N. Wagner, Y. C. Eldar, and Z. Friedman. Compressed beamforming in ultrasound imaging. *IEEE Transactions on Signal Processing*, 60(9):4643–4657, 2012.

[285] J. Wang, H. Xu, G. J. T. Leus, and G. A. E. Vandenbosch. Experimental assessment of the coarray concept for DOA estimation in wireless communications. *IEEE Transactions on Antennas and Propagation*, 66(6):3064–3075, June 2018.

[286] L. Wang and Y. Chi. Blind deconvolution from multiple sparse inputs. *IEEE Signal Processing Letters*, 23(10):1384–1388, 2016.

[287] M. Wang and A. Nehorai. Coarrays, MUSIC, and the Cramér-Rao bound. *IEEE Transactions on Signal Processing*, 65(4):933–946, Feb 2017.

[288] M. Wang, Z. Zhang, and A. Nehorai. Performance analysis of coarray-based MUSIC in the presence of sensor location errors. *IEEE Transactions on Signal Processing*, 66(12):3074–3085, June 2018.

[289] M. Wang, Z. Zhang, and A. Nehorai. Further results on the Cramér–Rao bound for sparse linear arrays. *IEEE Transactions on Signal Processing*, 67(6):1493–1507, 2019.

[290] X. Wang, E. Aboutanios, M. Trinkle, and M. G. Amin. Reconfigurable adaptive array beamforming by antenna selection. *IEEE Transactions on Signal Processing*, 62(9):2385–2396, 2014.

[291] X. Wang, M. Amin, and X. Cao. Analysis and design of optimum sparse array configurations for adaptive beamforming. *IEEE Transactions on Signal Processing*, 66(2):340–351, 2018.

[292] Y. Wang, G. Leus, and A. Pandharipande. Direction estimation using compressive sampling array processing. In *IEEE/SP 15th Workshop on Statistical Signal Processing*, pages 626–629, 2009.

[293] C. C. Weng and P. P. Vaidyanathan. Nonuniform sparse array design for active sensing. In *45th Asilomar Conference on Signals, Systems and Computers*, pages 1062–1066, Nov 2011.

[294] B. Wichmann. A note on restricted difference bases. *Journal of the London Mathematical Society*, s1-38(1):465–466, 1963.

[295] J. P. Wild and M. L. E. Oliphant. A new method of image formation with annular apertures and an application in radio astronomy. *Proceedings of the Royal Society of London. Series A. Mathematical and Physical Sciences*, 286(1407):499–509, 1965.

[296] T. Wild, V. Braun, and H. Viswanathan. Joint design of communication and sensing for beyond 5G and 6G systems. *IEEE Access*, 9:30845–30857, 2021.

[297] R. Willey. Space tapering of linear and planar arrays. *IRE Transactions on Antennas and Propagation*, 10(4):369–377, July 1962.

[298] A. A. Winder. II. Sonar system technology. *IEEE Transactions on Sonics and Ultrasonics*, 22(5):291–332, 1975.

[299] D. P. Wipf and B. D. Rao. Sparse Bayesian learning for basis selection. *IEEE Transactions on Signal Processing*, 52(8):2153–2164, 2004.

[300] Y. Xie, M. B. Wakin, and G. Tang. Simultaneous sparse recovery and blind demodulation. *IEEE Transactions on Signal Processing*, 67(19):5184–5199, 2019.

[301] Z. Yang, L. Xie, and C. Zhang. A discretization-free sparse and parametric approach for linear array signal processing. *IEEE Transactions on Signal Processing*, 62(19):4959–4973, 2014.

[302] T. Yokoyama, M. Henmi, A. Hasegawa, and T. Kikuchi. Effects of mutual interactions on a phased transducer array. *Japanese Journal of Applied Physics*, 37(Part 1, No. 5B):3166–3171, May 1998.

[303] M. Zatman. How narrow is narrowband? *IEE Proceedings-Radar, Sonar and Navigation*, 145(2):85–91, April 1998.

[304] M. A. Zatman, M. D. Macleod, D. McLernon, and H. J. Strangeways. Estimation bias variation on beamformed signals. *IEEE Transactions on Antennas and Propagation*, 43(12):1496–1499, Dec 1995.

[305] Y. D. Zhang, M. G. Amin, and B. Himed. Sparsity-based DOA estimation using co-prime arrays. In *IEEE International Conference on Acoustics, Speech and Signal Processing (ICASSP 2013)*, pages 3967–3971, May 2013.

[306] L. Zhao, L. Wang, L. Yang, A. M. Zoubir, and G. Bi. The race to improve radar imagery: An overview of recent progress in statistical sparsity-based techniques. *IEEE Signal Processing Magazine*, 33(6):85–102, 2016.

[307] Z. Zheng, W. Wang, Y. Kong, and Y. D. Zhang. MISC array: A new sparse array design achieving increased degrees of freedom and reduced mutual coupling effect. *IEEE Transactions on Signal Processing*, 67(7):1728–1741, April 2019.

[308] A. M. Zoubir, V. Koivunen, Y. Chakhchoukh, and M. Muma. Robust estimation in signal processing: A tutorial-style treatment of fundamental concepts. *IEEE Signal Processing Magazine*, 29(4):61–80, 2012.

[309] A. M. Zoubir, V. Koivunen, E. Ollila, and M. Muma. *Robust statistics for signal processing*. Cambridge University Press, 1st edition, 2018.

Errata

Publication I

In Section II-D1 and Table I, the aperture and number of elements of the PA should be $L = N(N+1)/4 - 1/2$ and $N = (\sqrt{16L+9} - 1)/2$. In (5) and Table I, the upper bound on R_∞ in case of the MRA should be 1.92. Correspondingly, the last column of Table I should read (from top to bottom): 0.72–0.79; 1; 1.02–1.12.

Publication III

The third row of the second column on the first page should read: "... [7] is one solution that *extends symmetrical* MRAs into a ...".

Publication IV

The last sentence of Section II-B1 should read: "For example, any *linear* array...". Corrections to Table I: in case of the MRA $S(2) \geq 0$ and $R_\infty \leq 2$; in case of the URA $S(2) = 2(L_x L_y - 1)$. It should be noted that the results in Table I hold for $L_x, L_y \geq 2$ in case of the MRA and BA, and $L_x, L_y \geq 4$ and even in case of the CRA.

Publication VII

In Definitions 1 and 4, $S(d)$ and $\mathscr{D}_2$ should be $S(d) = \sum_{d_n, d_m \in \mathscr{D}} \mathbb{1}(d_n - d_m = d)$ and $\mathscr{D}_2 = \{0 : N_1 + 1 : (N_2 - 1)(N_1 + 1)\}$, respectively.

Publication VIII

In Section VII-E, the dimensions of the one-dimensional Dolph-Chebyshev window should be $2 \cdot 17 - 1 = 33$, that is, $\mathbf{w}_{\mathrm{DC}} \in \mathbb{R}^{33}$.

Multisensor systems are a key enabling technology in, e.g., radar, sonar, medical ultrasound, and wireless communications. Advantages of using multiple sensors include spatial selectivity, improved signal-to-noise ratio, and the capability to reject unwanted interference.

Conventional multisensor systems employ a simple array of uniformly spaced sensors. However, a uniform array spanning a large electrical aperture may become prohibitively expensive, as many sensors and costly electronics are needed. In contrast, sparse sensor arrays require drastically fewer resources to achieve comparable performance.

This dissertation proposes novel sparse array designs and signal processing methods for active sensing and imaging. These cost-effective arrays resolve vastly more scatterers than sensors, and synthesize transmit-receive beampatterns that are conventionally achieved by uniform arrays only. The dissertation also develops methods for coherent linear imaging, where image quality is improved by summing multiple component images. The component images may correspond to separate transmissions and receptions depending on the employed beamforming architecture and waveform diversity. The contributions of the thesis are of practical value in the design of sensor arrays for active sensing.

Aalto-DD 108/2021

ISBN 978-952-64-0473-8 (printed)
ISBN 978-952-64-0474-5 (pdf)
ISSN 1799-4934 (printed)
ISSN 1799-4942 (pdf)

Aalto University
School of Electrical Engineering
Department of Signal Processing and Acoustics
www.aalto.fi

BUSINESS + ECONOMY

ART + DESIGN + ARCHITECTURE

SCIENCE + TECHNOLOGY

CROSSOVER

DOCTORAL DISSERTATIONS